



**CERAMIC MATRIX COMPOSITE CHARACTERIZATION UNDER A GAS  
TURBINE COMBUSTION AND LOADING ENVIRONMENT**

THESIS

Dustin J. Bertrand, Captain, USAF

AFIT-ENY-14-M-08

**DEPARTMENT OF THE AIR FORCE  
AIR UNIVERSITY**

**AIR FORCE INSTITUTE OF TECHNOLOGY**

---

---

**Wright-Patterson Air Force Base, Ohio**

**DISTRIBUTION STATEMENT A.**  
APPROVED FOR PUBLIC RELEASE; DISTRIBUTION UNLIMITED.

The views expressed in this thesis are those of the author and do not reflect the official policy or position of the United States Air Force, Department of Defense, or the United States Government. This material is declared a work of the U.S. Government and is not subject to copyright protection in the United States.

AFIT-ENY-14-M-08

**CERAMIC MATRIX COMPOSITE CHARACTERIZATION UNDER A GAS  
TURBINE COMBUSTION AND LOADING ENVIRONMENT**

**THESIS**

Presented to the Faculty

Department of Aeronautics and Astronautics

Graduate School of Engineering and Management

Air Force Institute of Technology

Air University

Air Education and Training Command

In Partial Fulfillment of the Requirements for the

Degree of Master of Science in Materials Science

Dustin J. Bertrand, BS

Captain, USAF

17-03-2014

**DISTRIBUTION STATEMENT A.**  
APPROVED FOR PUBLIC RELEASE; DISTRIBUTION UNLIMITED.

**CERAMIC MATRIX COMPOSITE CHARACTERIZATION UNDER A GAS  
TURBINE COMBUSTION AND LOADING ENVIRONMENT**

Dustin J. Bertrand, BS

Captain, USAF

Approved:

\_\_\_\_\_  
//SIGNED//  
Shankar Mall, Civ, USAF, PhD (Chairman)

\_\_\_\_\_  
3/13/14  
Date

\_\_\_\_\_  
//SIGNED//  
Vinod Jain, Civ, University of Dayton, PhD (Member)

\_\_\_\_\_  
3/13/14  
Date

\_\_\_\_\_  
//SIGNED//  
Timothy Radsick, Lt Col, USAF, PhD (Member)

\_\_\_\_\_  
3/13/14  
Date



## **Abstract**

Ceramic matrix composites (CMC) show promise in gas turbine aircraft applications in increasing performance and efficiency. Manufacturing turbine blades and other turbine section parts out of these materials can potentially increase turbine inlet temperatures or reduce or eliminate the need for bleed air cooling, thereby increasing performance and efficiency of gas turbine engines.

The fatigue behavior of Hyper-Therm High Temperature Composites (HTC) Sylramic-iBN/BN/CVI SiC material was investigated while being subjected to a unique high temperature environment. The material under investigation is made up of woven Sylramic SiC (silicon carbide) fibers situated in an SiC matrix using chemical vapor infiltration (CVI). The specimens used in this research were subjected to a high temperature combustion environment intended to simulate the conditions this material would see in turbine engine applications.

The combustion environment was created using a High-Velocity Oxygen Fuel (HVOF) Gun. The flame directly impinged the CMC specimen on one side, as it was subjected to cyclic fatigue loading, heating up the surface of the specimen to temperatures of approximately 1250°C, 1350°C, and 1480°C. Results show that the effects of the combustion environment on the materials fatigue behavior are significant with increasing temperature.

## **Acknowledgments**

I would like to express my sincere appreciation to my faculty advisor, Dr. Shankar Mall, for his guidance and support throughout the course of this thesis effort. The insight and experience was certainly appreciated. I would, also, like to thank my sponsor, Mr. Larry Zawada, from the Air Force Research Lab for both the support and latitude provided to me in this endeavor. I would also like to thank the composites team at the AFRL Materials Directorate for their suggestions and input into this research. My appreciation also goes to Dr. Volodymyr Sabelkin for his guidance and experience during the course of this research.

Dustin J. Bertrand

## Table of Contents

	Page
Abstract .....	iv
Table of Contents .....	vi
List of Figures .....	viii
List of Tables .....	xiv
I. Introduction .....	1
1.1. Evolution of Aircraft Propulsion .....	1
1.2. CMCs .....	4
1.2.1. Oxidation .....	5
1.2.2. Hyper-Therm HTC Sylramic <sup>tm</sup> -iBN/BN/CVI SiC .....	7
1.3. Fatigue Loading .....	7
1.4. Combustion Environment .....	7
1.5. Objectives .....	8
II. Literature Review .....	10
Chapter Overview .....	10
2.1. Similar Research on Similar Material .....	10
2.2. SiC Recession .....	12
2.3. Rolls Royce Tensile Tests .....	12
III. Test Equipment and Experimental Procedure .....	14
Chapter Overview .....	14
3.1. Material Description and Specimen Geometry .....	14
3.2. Equipment .....	15
3.2.1. Material Test Stand .....	15
3.2.2. High-Velocity Oxygen-Fuel Flame System .....	19

3.2.3. Safety Shutdown System .....	22
3.2.4. Forward-Looking Infrared System .....	23
3.2.5. Specimen Imaging Equipment .....	27
3.3. Test Procedure .....	30
3.3.1. Specimen Inspection and Processing.....	30
3.3.2. Equipment Start-up and Specimen Loading.....	31
3.3.3 HVOF and Temperature Measurement Start-up .....	33
3.3.4. Fatigue Tests.....	36
3.3.5. Residual Strength Tests .....	38
3.4 Test Matrix .....	39
IV. Analysis and Results.....	40
Chapter Overview.....	40
4.1. Specimen Temperatures in Testing .....	40
4.2. Thermal Strain During Testing.....	57
4.3. Fatigue Tests.....	58
4.4. Residual Strength Tests .....	70
4.5. Material Loss - Oxidation and Erosion .....	73
4.6. Microstructural Analysis .....	85
4.7. Results Summary.....	100
V. Conclusions and Recommendations .....	101
Appendix.....	103
Bibliography .....	118

## List of Figures

	Page
Figure 1 - Evolution of Turbine Inlet Temperature [8].....	2
Figure 2 - Temperature Limits of Select Materials [3] .....	3
Figure 3 - CMC Toughening Mechanisms [4].....	5
Figure 4 - Fracture Surfaces of Burner Rig Fatigue Tests Performed By Kim [13] .....	11
Figure 5 - Room Temperature Stress-Strain Curve Produced By Rolls Royce [2] .....	13
Figure 6 - Stress-Strain Curve at 1480°C Produced by Rolls Royce [2] .....	13
Figure 7 - Specimen Geometry .....	14
Figure 8 - Material Test Stand .....	16
Figure 9 - NESLAB RTE 7 Chiller.....	17
Figure 10 - Grip Cooling/Insulation Scheme.....	18
Figure 11 - HVOF Nozzle [9] .....	19
Figure 12 - HVOF Spray Gun Mount .....	20
Figure 13 - DJF Flowmeter Unit Used To Control Spray Gun.....	20
Figure 14 - Whisper Room Containing Burner Rig Test Setup.....	22
Figure 15 - Pressure-Operated Valves for Oxygen and Propane .....	23
Figure 16 - FLIR Camera In Mount.....	24
Figure 17 - FLIR Camera Output During Testing .....	26
Figure 18 - Optical Microscope Used to Image Specimens .....	27
Figure 19 - SEM Used to Image Specimens .....	28
Figure 20 - Cut-out of Specimen N811 for SEM Imaging .....	29
Figure 21 - Specimen Mounted and Polished for SEM .....	29

Figure 22 - Specimen Prepared for Testing .....	31
Figure 23 - LabVIEW Software Display Before Start of Test.....	34
Figure 24 - Flame Gun In Operation.....	36
Figure 25 - Cyclic Fatigue Loading With PVC .....	37
Figure 26 - MPT Procedure for Fatigue Tests .....	38
Figure 27 - Specimen N88 IR Image With Measurements .....	42
Figure 28 - Temperature Profile Specimen N82 .....	43
Figure 29 - Temperature Profile Specimen N83 .....	44
Figure 30 - Temperature Profile Specimen N84 .....	45
Figure 31 - Temperature Profile Specimen N85 .....	46
Figure 32 - Temperature Profile Specimen N86 .....	47
Figure 33 - Temperature Profile Specimen N87 .....	48
Figure 34 - Temperature Profile Specimen N88 .....	49
Figure 35 - Temperature Profile Specimen N810 .....	50
Figure 36 - Temperature Profile Specimen N811 .....	51
Figure 37 - Temperature Profile Specimen N812 .....	52
Figure 38 - Temperature Profile Specimen N813 .....	53
Figure 39 - Hot Spot on Specimen N83 at 1529°C.....	55
Figure 40 - Thermal Image of Specimen N811 Backside.....	56
Figure 41 - IR Image of Backside N811 and Front and Back Temperature Profiles.....	57
Figure 42 - All Specimens After Tests .....	60
Figure 43 - S-N Curve Developed From Experimental Data .....	61

Figure 44 - S-N Curve Normalized to The Room Temperature UTS Provided by Rolls Royce.....	62
Figure 45 - Temperature vs. Number of Cycles for All Specimens .....	63
Figure 46 - 210 MPa 1480°C (#N82) Specimen Extension vs Number of Cycles.....	64
Figure 47 - 175 MPa 1480°C (#N87) Specimen Extension vs. Number of Cycles.....	64
Figure 48 - 125 MPa 1480°C (#N88) Specimen Extension vs. Number of Cycles.....	65
Figure 49 - 80 MPa 1480°C (#N810) Specimen Extension vs. Number of Cycles.....	65
Figure 50 - Grip Temperature vs. Number of Cycles for Specimen N810.....	66
Figure 51 - 210 MPa 1350°C (#N83) Specimen Extension vs. Number of Cycles.....	67
Figure 52 - 125 MPa 1350°C (#N812) Specimen Extension vs. Number of Cycles.....	67
Figure 53 - 90 MPa 1350°C (#N813) Specimen Extension vs. Number of Cycles.....	68
Figure 54 - 210 MPa 1250°C (#N84) Specimen Extension vs. Number of Cycles.....	68
Figure 55 - 175 MPa 1250°C (#N85) Specimen Extension vs. Number of Cycles.....	69
Figure 56 - 125 MPa 1250°C (#N86) Specimen Extension vs. Number of Cycles.....	69
Figure 57 - Specimen N86 Residual Strength Test Stress vs. Strain .....	70
Figure 58 - Fracture Surface of Specimen N86 After Residual Strength Test .....	71
Figure 59 - Specimen N813 Residual Strength Test Stress vs. Strain .....	72
Figure 60 - Fracture Surface of Specimen N813 After Residual Strength Test .....	73
Figure 61 - Weight Loss vs. Time for All Specimens .....	74
Figure 62 - Weight Loss Data Normalized to Original Weights .....	74
Figure 63 - Volume Loss vs. Time for All Specimens .....	75
Figure 64 - Flame Side of Specimen N82 After Fatigue Test With no Material Loss .....	76
Figure 65 - Specimen N87 Signs of Erosion After 2 hrs .....	77

Figure 66 - Specimen N88 With Obvious Material Loss After 3.5 hrs .....	78
Figure 67 - Specimen N810 With Obvious Material Loss After 4.3 Hrs .....	79
Figure 68 - Pits Starting to Form on Specimen N813.....	80
Figure 69 - Specimen N811 Material Loss Over Time.....	82
Figure 70 - Thermal Images of Specimen N811 Hot Spot Development and Erosion.....	82
Figure 71 - N811 Loss of Material After 16.7 Hrs at a Temperature of 1480°C.....	83
Figure 72 - Right, Center, and Left Edge Thickness Measurements of Specimen N811 vs. Time .....	85
Figure 73 - SEM Image of Un-tested Specimen.....	86
Figure 74 - SEM Image of Un-tested Specimen Zoomed In to See Fibers .....	86
Figure 75 - Specimen N83 SEM Image of Overall Fracture Surface .....	87
Figure 76 - Specimen N85 SEM Image of Overall Fracture Surface .....	87
Figure 77 - Specimen N810 SEM Image of Overall Fracture Surface .....	88
Figure 78 - Specimen N811 SEM Image of Overall Fracture Surface .....	88
Figure 79 - Specimen N83 Showing Signs of Fiber Pull-out .....	89
Figure 80 - Oxidation on Specimen N83 .....	90
Figure 81 - Specimen N83 With Some Fiber Pull-out.....	91
Figure 82 - Center of Specimen N85 No Signs of Oxidation .....	92
Figure 83 - Specimen N85 Large Area of Oxidized Material .....	93
Figure 84 - Specimen N85 Area of Oxidation Where the Fibers and Matrix are Fused Together .....	94
Figure 85 - Specimen N810 Piece of Matrix Material Extending out of Surface and Areas of Oxidized and Non-Oxidized Material.....	95



Figure 86 - Volatilization of the BN Fiber Coating and Oxidation of Fibers and Matrix on Specimen N811 .....	95
Figure 87 - Heavily Oxidized Area Around a Void in Specimen N811 .....	96
Figure 88 - Stove Piping Occurring Along the Length of the Fibers in Specimen N811 .	97
Figure 89 - Specimen N811 Volatilization of BN Coating and Formation of Borosilicate Glass .....	98
Figure 90 - SEM Image of Specimen N811 No Noticeable Damage Due to Combustion Environment.....	99
Figure 91 - SEM Image of Specimen N83 Flame Side Center, 500x.....	103
Figure 92 - SEM Image of Specimen N83 Flame Side Right, 150x.....	104
Figure 93 - SEM Image of Specimen N83 Backside Right, 80x .....	104
Figure 94 - SEM Image of Specimen N83 Backside Center, 424x .....	105
Figure 95 - SEM Image of Specimen N83 Center of Thickness Right Side, 800x .....	105
Figure 96 - SEM Image of Specimen N85 Backside Center, 600x .....	106
Figure 97 - SEM Image of Specimen N85 Backside Right, 160x .....	107
Figure 98 - SEM Image of Specimen N85 Backside Center, 400x .....	107
Figure 99 - SEM Image of Specimen N85 Backside Center, 400x .....	108
Figure 100 - SEM Image of Specimen N85 Backside Left, 400x .....	108
Figure 101 - SEM Image of Specimen N85 Backside Left, 100x .....	109
Figure 102 - SEM Image of Specimen N85 Flame Side Left, 84x.....	109
Figure 103 - SEM Image of Specimen N810 Flame Side Right, 200x.....	110
Figure 104 - SEM Image of Specimen N810 Flame Side Center, 2000x.....	111
Figure 105 - SEM Image of Specimen N810 Flame Side Left, 250x.....	111

Figure 106 - SEM Image of Specimen N810 Flame Side Left, 130x .....	112
Figure 107 - SEM Image of Specimen N810 Back Side Left, 130x.....	112
Figure 108 - SEM Image of Specimen N810 Back Side Left, 1000x.....	113
Figure 109 - SEM Image of Specimen N810 Back Side Center, 150x.....	113
Figure 110 - SEM Image of Specimen N811 Back Side Left, 300x.....	114
Figure 111 - SEM Image of Specimen N811Back Side Left, 2400x.....	115
Figure 112 - SEM Image of Specimen N811 Flame Side Right, 600x.....	115
Figure 113 - SEM Image of Specimen N811 Back Side Right, 300x .....	116
Figure 114 - SEM Image of Specimen N811 Back Side Right, 600x .....	116
Figure 115 - SEM Image of Specimen N811 Back Side Center, 1000x.....	117
Figure 116 - SEM Image of Specimen N811 Back Side Center, 500x.....	117

## **List of Tables**

	Page
Table 1 - HVOF Gas Pressures and Range of Flow Rates .....	35
Table 2 - Fatigue Test Matrix .....	39
Table 3 - Average, Max, and Min Temperatures for Box Area for Each Specimen .....	41
Table 4 - Average, Max, and Mix Temperatures for Circle Area for Each Specimen .....	41
Table 5 - Thermal Strain and Coefficient of Thermal Expansion Calculation .....	58
Table 6 - Fatigue Tests Results Summary .....	59

# **CERAMIC MATRIX COMPOSITE CHARACTERIZATION UNDER A GAS TURBINE COMBUSTION AND LOADING ENVIRONMENT**

## **I. Introduction**

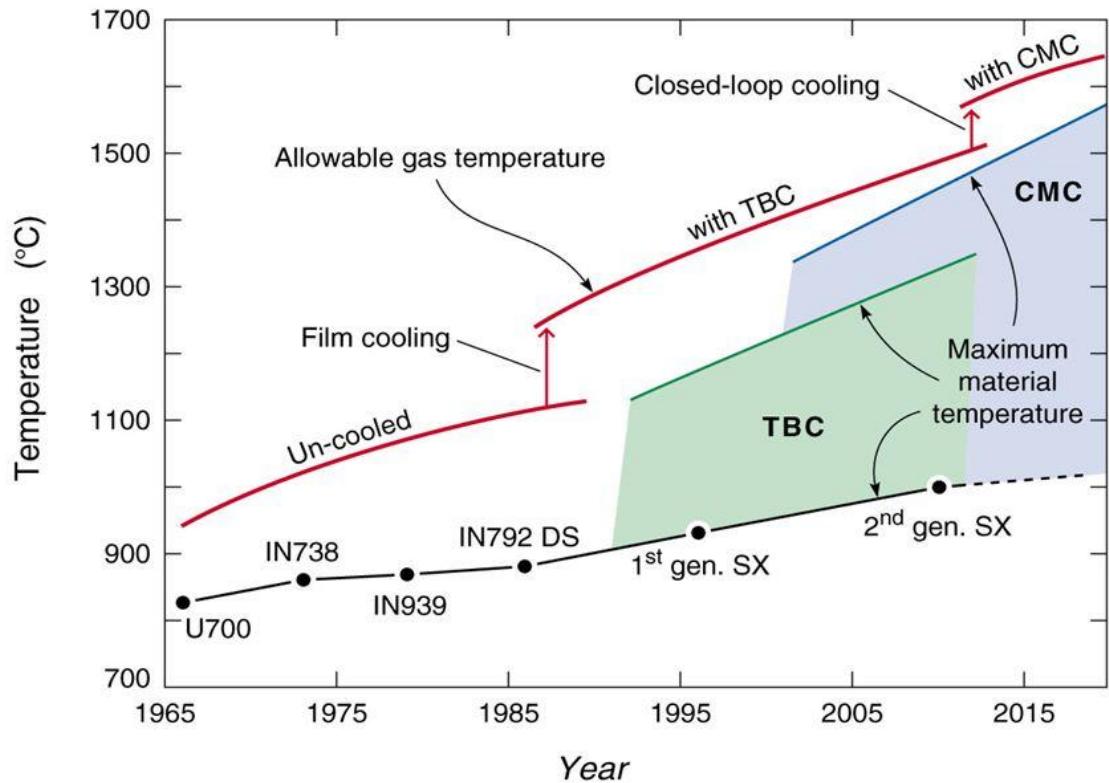
Engineers are constantly looking to improve the performance, efficiency, and reliability of aircraft. Both military and civilian aerospace users are looking for advancements in aircraft to make them fly higher, faster, farther, last longer, and safer. One critical component of an aircraft is the propulsion system. One of the most commonly used propulsion system for commercial and military applications is the gas turbine engine. The need for advancements in the aerospace industry has led to increased demands of higher thrust and higher efficiency turbine engines.

### **1.1. Evolution of Aircraft Propulsion**

One way to increase the efficiency and performance of a turbine engine is by increasing the high-pressure turbine inlet temperature. The turbine inlet temperature has an effect on both the thermal efficiency and the thrust per unit rate of airflow through the engine. The ideal situation is to design the turbine inlet temperature to be as high as the turbine blade material can withstand [9]. This has resulted in research into materials for turbine blades and blade cooling techniques.

Some of the first materials used for manufacturing turbine blades were iron-based alloys that would provide acceptable properties at temperatures up to 650°C [17]. To achieve higher temperatures, nickel-based “superalloys” were developed. In addition to new alloys, new manufacturing methods were also developed that allowed higher turbine inlet temperatures to be reached. Some of these methods include directionally-solidified turbine airfoils and then single crystal turbine airfoils [7]. These materials are able to

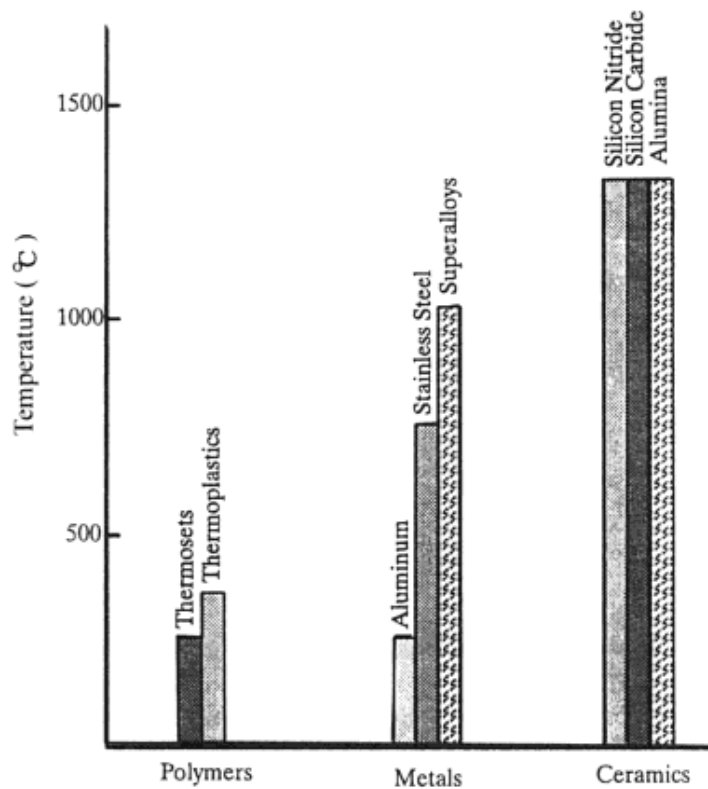
withstand operating temperatures of around 1000°C. Figure 1 shows the evolution of turbine inlet temperatures due to advances in materials, manufacturing processes, and blade cooling techniques [8].



**Figure 1 - Evolution of Turbine Inlet Temperature [8]**

To enable even higher turbine inlet temperatures, blade cooling schemes were developed. The most used cooling design is an open-loop air cooling system which uses bleed air from the compressor core air flow [1]. With open loop blade cooling systems, 20% - 30% of the compressor core air flow bypasses the combustor to be used for turbine cooling [1]. The use of ceramic matrix composites (CMCs) in aircraft engines can either further increase turbine inlet temperatures when used with blade cooling techniques, or

their use can eliminate the need for blade cooling while maintaining present temperatures. Either situation will lead to increased performance and efficiency of turbine engines. Figure 2 contains a comparison of the temperature limits of other materials to ceramics.



**Figure 2 - Temperature Limits of Select Materials [3]**

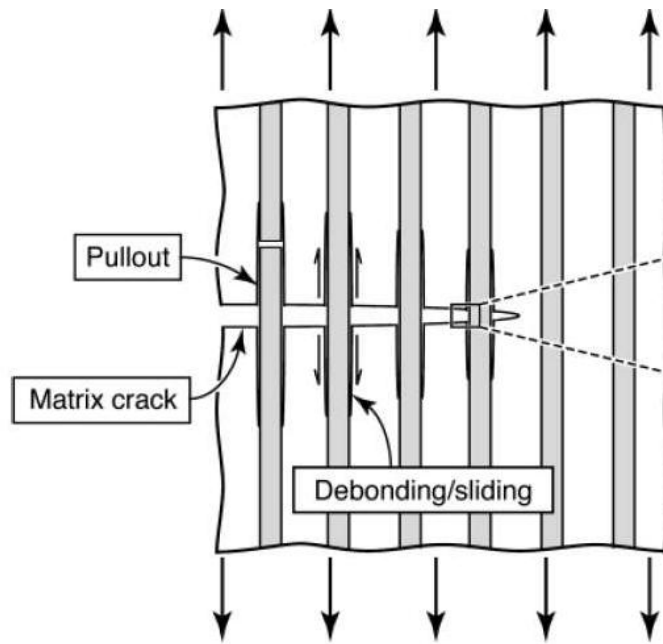
## 1.2. CMCs

Since ceramic materials are able to withstand high temperatures, they are of interest for manufacturing hot turbine engine section parts. Ceramic materials also show good resistance to chemicals, abrasion, and wear. However, due to the mechanical properties of ceramic materials in monolithic form, they are not ideal candidates for parts such as turbine blades and rotors. Monolithic ceramic materials are prone to catastrophic failure under mechanical or thermal loading since they do not show any plasticity [3] and they exhibit poor fracture toughness. This has led to investigation of the use of CMCs for these applications.

Even though monolithic ceramic materials have high theoretical tensile strengths, the existence of flaws in the material keep the actual strength of the material much lower than the theoretical strength. These flaws make catastrophic failure due to fracture a possibility with monolithic ceramics. When tensile loads are applied to monolithic ceramics, the cracks are being stretched apart as opposed to being pushed together in compressive loading. The stretching apart of the cracks in the material allow the cracks to propagate through the material leading to catastrophic failure.

CMCs improve the fracture toughness of ceramic materials reducing the risk of catastrophic failure and making them more suitable for mechanical components of the turbine engine hot section. This is done by including ceramic fibers, particles, or whiskers to reinforce a ceramic matrix. Incorporating the reinforcements introduces energy-dissipating phenomena such as debonding at the fiber/matrix interface, crack deflection, fiber pullout, and other phenomenon. These phenomenon introduce toughening mechanisms and allows the material to show damage tolerant behavior [3].

Figure 3 contains a visualization of the mechanisms previously discussed. The fiber reinforcement used in CMCs works to deflect and prevent cracks from propagating through the material. Fiber pullout, debonding, and sliding of the fibers also dissipate some of the energy that would otherwise contribute to crack propagation in the material. Increased toughness and damage tolerance of CMCs make them more suitable for handling loads in gas turbine engines compared to monolithic ceramic materials.



**Figure 3 - CMC Toughening Mechanisms [4]**

### **1.2.1. Oxidation**

SiC CMC materials are being proposed for use in combustion environments because of their thermal resistance and mechanical properties. One of the qualities associated with a combustion environment is the presence of water. The combustion of hydrocarbon fuels introduces significant amounts of water vapor into the environment. It has been shown that water vapor plays several roles in the degradation of silicon-based



materials. One role that water vapor plays is to increase the intrinsic oxidation rate of these materials relative to the rates observed in dry oxygen or air [11]. Water vapor influences the parabolic rate constant ( $k_p$ ) that governs the growth of SiO<sub>2</sub> on SiC:

$$x^2 = k_p t$$

where  $x$  is the oxide thickness and  $t$  is the oxidation time. Another effect of water vapor on SiC is the formation of volatile products, such as Si(OH)<sub>4</sub>, by its direct reaction with SiO<sub>2</sub>. Under conditions where significant volatility of the SiO<sub>2</sub> can occur, the SiO<sub>2</sub> can grow by the equation presented above, but after a certain time, its thickness is limited by the simultaneous loss of SiO<sub>2</sub> by formation of gaseous products [25].

Boron Nitride (BN) is currently used as an interphase material for SiC/SiC CMCs. Without a crack in the SiC matrix, BN is stable in contact with SiC at high temperatures. In the presence of cracks in the matrix, BN could be exposed to high oxygen potentials. At temperatures above 900°C, BN oxidizes to a liquid oxide (B<sub>2</sub>O<sub>3</sub>) and SiC oxidizes simultaneously. SiC oxidation can occur at even lower temperatures because of the boron interacting with the SiO<sub>2</sub> scale as it forms. The SiO<sub>2</sub> and B<sub>2</sub>O<sub>3</sub> react to form borosilicate glass. Oxygen diffusivities are more rapid in borosilicate glass so SiC oxidation is enhanced. This leads to degradation of the fiber properties and the fiber/matrix bonding [12].

### **1.2.2. Hyper-Therm HTC Sylramic<sup>™</sup>-iBN/BN/CVI SiC**

The Sylramic<sup>™</sup>-iBN/BN/CVI SiC CMC investigated during this research is composed of 10  $\mu\text{m}$  diameter woven Sylramic<sup>™</sup>-iBN SiC fibers produced by COI Ceramics, Inc (San Diego, CA). The fibers have a coating of boron nitride (BN) to act as an interface between the fibers and the matrix. Hyper-Therm HTC, Inc. (Huntington Beach, CA) used chemical vapor infiltration (CVI) to form the SiC matrix around the woven fibers.

### **1.3. Fatigue Loading**

Low cycle fatigue (LCF) can rapidly consume the life of parts in the hot section of gas turbine engines, especially those used in fighter aircraft applications, so there is importance placed on LCF during the design of these engines. Temperature gradients can sometimes give rise to surprisingly high stresses as the material counteracts uneven expansion and contraction. These temperature gradients and stresses can be amplified during the transitions between power settings during the different phases of flight [19].

### **1.4 Combustion Environment**

The combustion environment experienced in the hot section of a gas turbine engine is difficult to reproduce experimentally. The hot gases in this area of the turbine engine can be traveling at speeds approaching mach 1 or higher. This high-speed impingement on the components in the turbine section creates forces that are difficult to account for and replicate in an experimental setup. Another attribute of the combustion environment that is difficult to replicate experimentally is the temperature gradient created on components due to the non-uniformity of the flame. These conditions also

change during the different phases of flight experienced by turbine engines in aerospace applications.

A concern for materials subjected to a combustion environment is the effect of pollutants produced during combustion on the material. The main pollutants produced during combustion are unburned and partially burned hydrocarbons, nitrogen oxides, carbon monoxide, sulfur oxides, and other particulate matter [26]. There are two issues of concern especially for materials such as CMCs. The first is the high-speed impact of these pollutants on the material that can produce additional loads. The other issue is since CMCs are manufactured in a manner that leaves them somewhat porous, these pollutants can possibly penetrate the material and possibly affect the mechanical behavior of the material especially at the high temperatures seen at the exit of the combustion chamber of a gas turbine engine.

## **1.5. Objectives**

CMC materials are currently thought to be the future of high-temperature aerospace applications. There is still work to be done to characterize these materials before they can be used on production structural aerospace components specifically turbine blades and stators.

Past efforts at AFIT resulted in the design of an experimental setup that allows for testing of a material in a combustion environment while under fatigue loading. These kinds of tests have rarely been done due to the difficulty in replicating the conditions seen in the hot sections of gas turbine engines in a laboratory environment.

The purpose of the present research is to observe the fatigue behavior of the Hypertherm Sylramic<sup>tm</sup>-iBN/BN/CVI SiC matrix composite in a combustion environment, to develop stress versus number of cycles diagrams, to investigate the effects of temperature on the fatigue behavior of the material, to estimate material loss due to oxidation and erosion caused by the combustion environment, and to study the microstructure, fracture surfaces, and fiber degradation using scanning electron microscopy and measuring techniques.

The experimental combustion environment is generated by a high-temperature high-speed jet acting on the center of the specimen. The flame of the high-speed jet will heat the surface of the specimen to three target temperatures: 1250°C, 1350°C, and 1480°C. Fatigue loading consists of a tension-tension 1 Hz sinusoidal load with a stress ratio of 0.1.

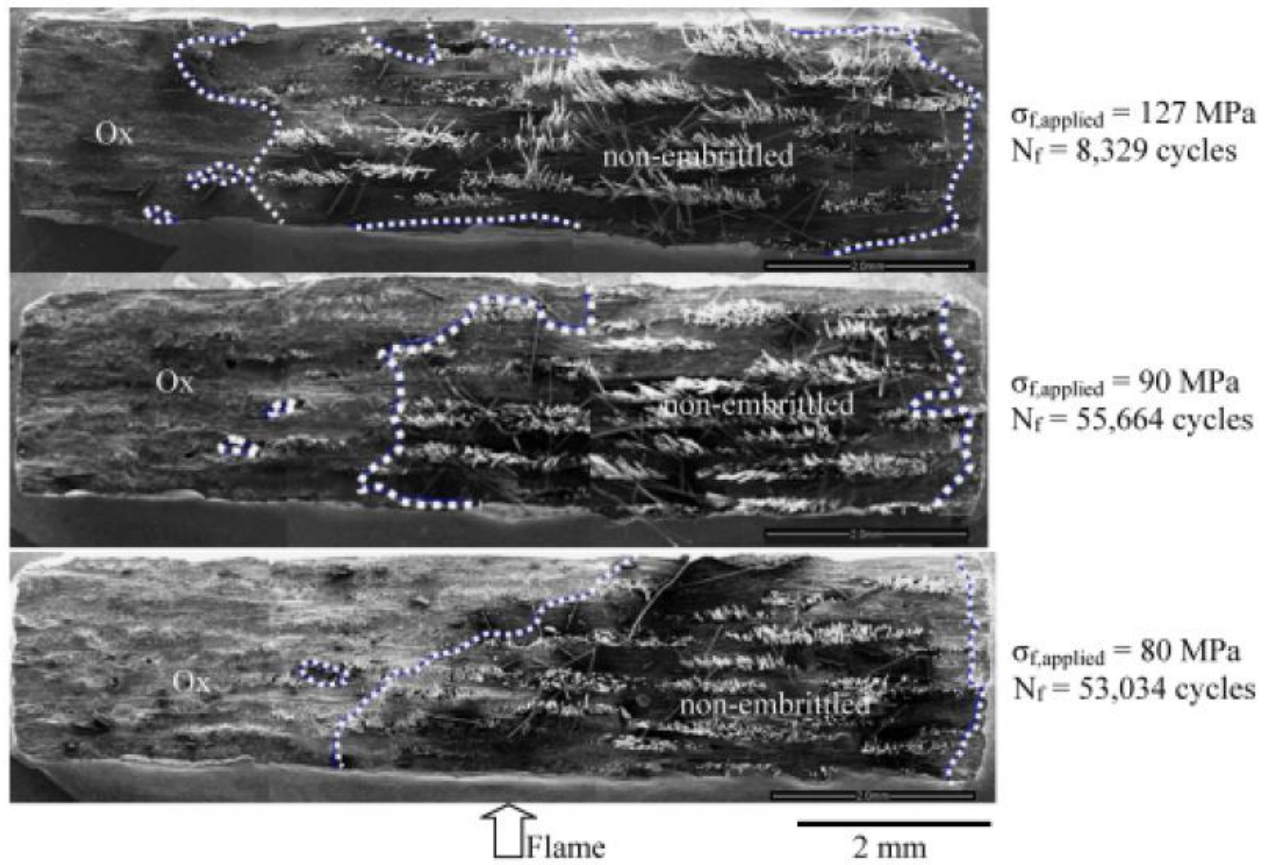
## **II. Literature Review**

### **Chapter Overview**

This chapter presents similar work done on similar materials as well as other work that is relevant to this research.

#### **2.1. Similar Research on Similar Material**

Kim et. al. tested a melt-infiltrated (MI) woven ceramic matrix composite consisting of a silicon carbide matrix reinforced by boron nitride coated Hi-Nicalon type S<sup>TM</sup> SiC fiber under tension-tension fatigue loading in combination with combustion conditions. This environment was representative of those experienced by hot-section components such as turbine blades and vanes in modern gas turbine engines [13]. This testing was performed in the same laboratory apparatus that the present research was performed. All specimens were heated to a surface temperature near 1250°C. Tests were performed at 80 MPa, 90 MPa, and 127 MPa max stress in the burner rig. The specimen tested at 127 MPa survived 8,329 cycles, the specimen tested at 90 MPa survived 55,664 cycles, and the specimen tested at 80 MPa survived 53,034. The fracture surfaces of the specimens tested at 80 and 90 MPa exhibited an area of oxidized material of similar size that was larger than the area of oxidized material exhibited in the specimen tested at 127 MPa [13]. The amount of oxidized material and non-embrittled material is shown in Figure 4 for the three specimens.



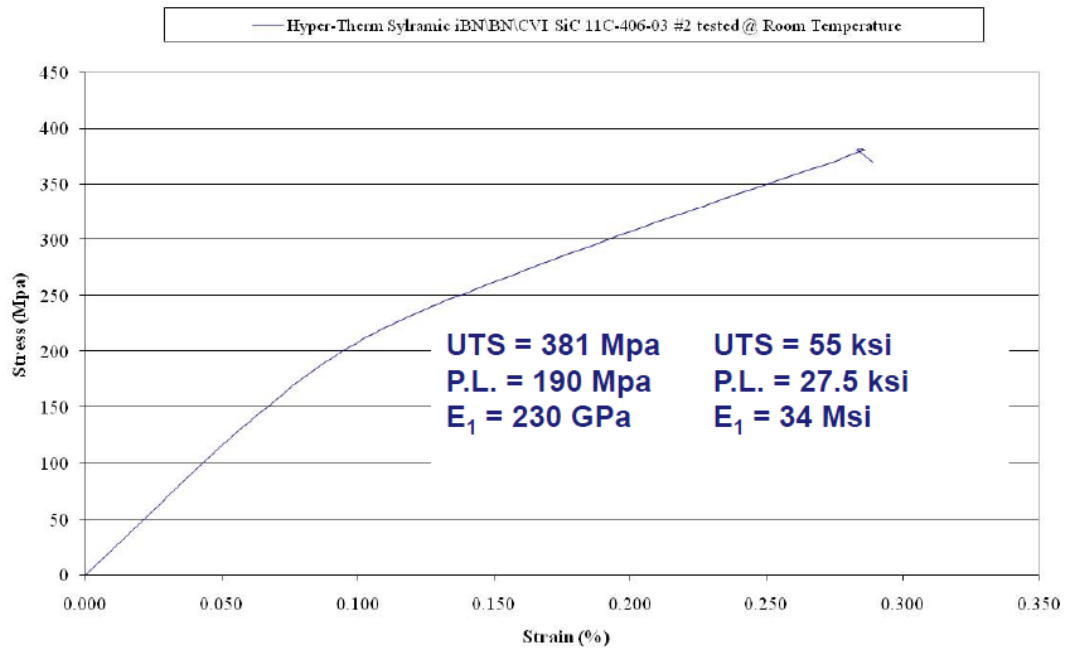
**Figure 4 - Fracture Surfaces of Burner Rig Fatigue Tests Performed By Kim [13]**

## **2.2. SiC Recession**

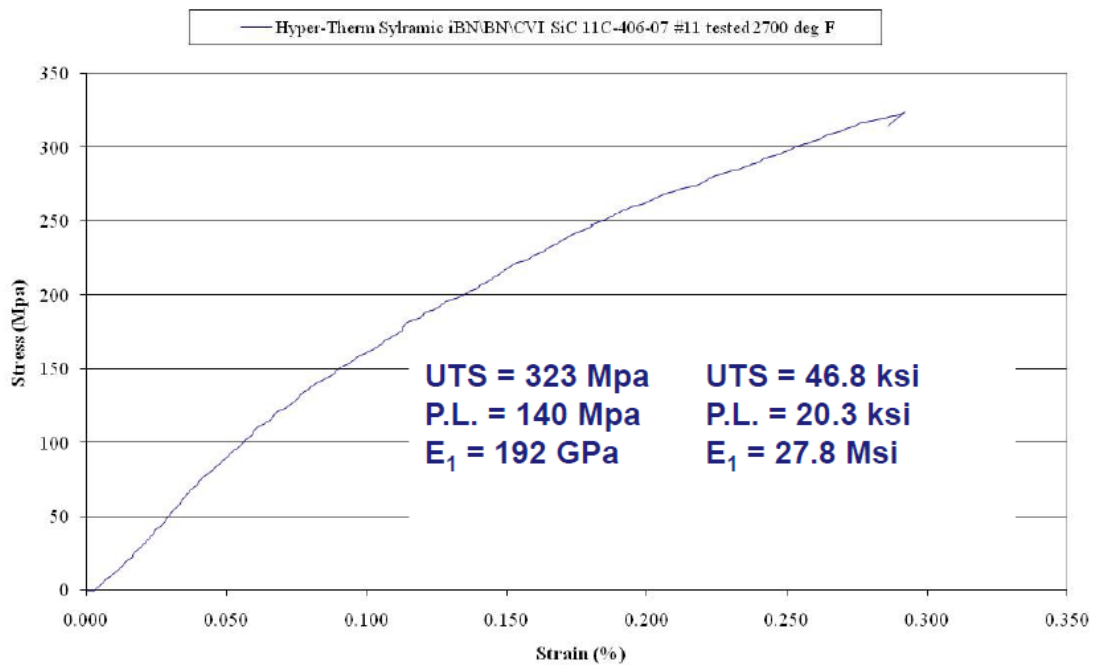
Robinson et. al. developed a high-pressure burner rig to evaluate the response of SiC material during exposure to simulated gas turbine combustor conditions. The testing by Robinson resulted in linear weight loss and surface recession rates as a result of SiO<sub>2</sub> volatility. The second part of Robinson's research developed a chemical model for the volatilization of SiO<sub>2</sub> in complex combustion environments that describes weight loss and surface recession for SiC in combustion environments [21,23].

## **2.3. Rolls Royce Tensile Tests**

Rolls Royce performed tensile tests on the Hyper-Therm HTC Sylramic<sup>tm</sup>-iBN/BN/CVI SiC material. Tests were performed at room temperature and at 1480°C in a furnace. The results of these two tests are presented in the stress-strain diagrams in Figure 5 and Figure 6. The ultimate tensile strength (UTS) for room temperature was determined to be 381 MPa, and the UTS for 1480°C was determined to be 323 MPa [2].



**Figure 5 - Room Temperature Stress-Strain Curve Produced By Rolls Royce [2]**



**Figure 6 - Stress-Strain Curve at 1480°C Produced by Rolls Royce [2]**



### III. Test Equipment and Experimental Procedure

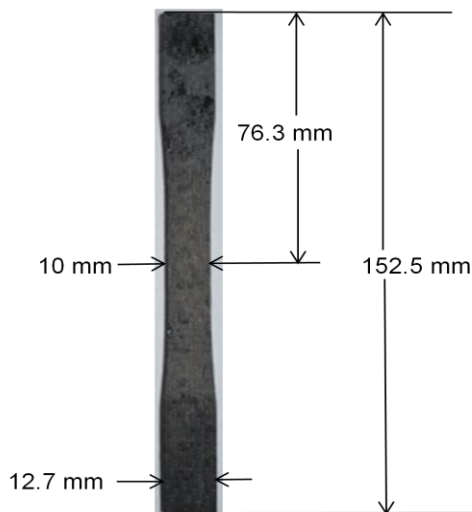
#### Chapter Overview

This chapter reviews the test equipment and experimental procedures used during the present research. The Hypertherm Sylramic<sup>tm</sup>-iBN/BN/CVI SiC material background will be discussed, along with specimen geometry and preparation.

#### 3.1. Material Description and Specimen Geometry

The Hyper-Therm HTC Sylramic<sup>tm</sup>-iBN/BN/CVI SiC material consists of woven Sylramic<sup>tm</sup>-iBN fibers. The SiC matrix is infiltrated into the woven fiber preforms using chemical vapor infiltration.

The specimens for this research were machined from a larger sheet of the material with a water jet. The specimens were cut into a dog-bone shape with the dimensions shown in Figure 7.



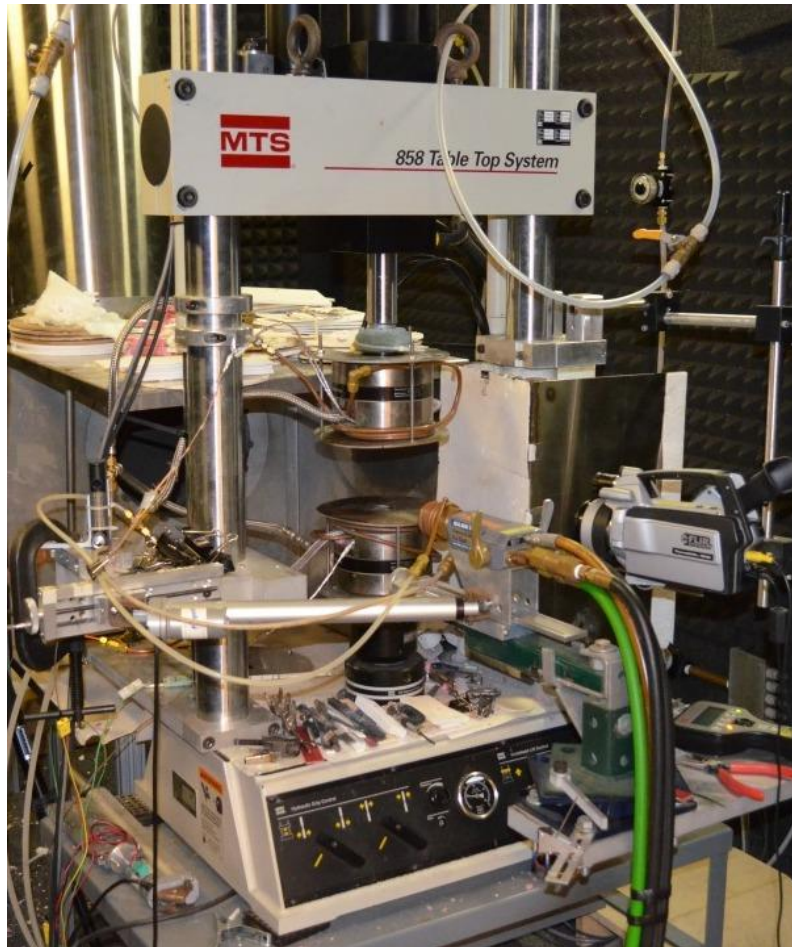
**Figure 7 - Specimen Geometry**

### **3.2. Equipment**

The equipment used during the course of this research consisted of a material test stand (MTS), a high velocity oxygen fuel (HVOF) flame system, a forward looking infrared (FLIR) camera system, an optical microscope, and a scanning electron microscope (SEM).

#### **3.2.1. Material Test Stand**

For this research, fatigue testing was accomplished using a vertically actuated, servo-hydraulic MTS 858 Table Top System test stand. This MTS is rated for a max force of 25,000 N, but during the course of this experiment, the applied force never exceeded 4,000 N [20]. This was due to the specimen geometry. The MTS is controlled through a computer workstation with an MTS TestStar™ II's digital controller and MTS *Multi-Purpose Testware* software. The digital controller provides an interface for signal generation and data acquisition, and the Testware provides a user interface to input testing parameters to the controller. Figure 8 shows the MTS test apparatus.



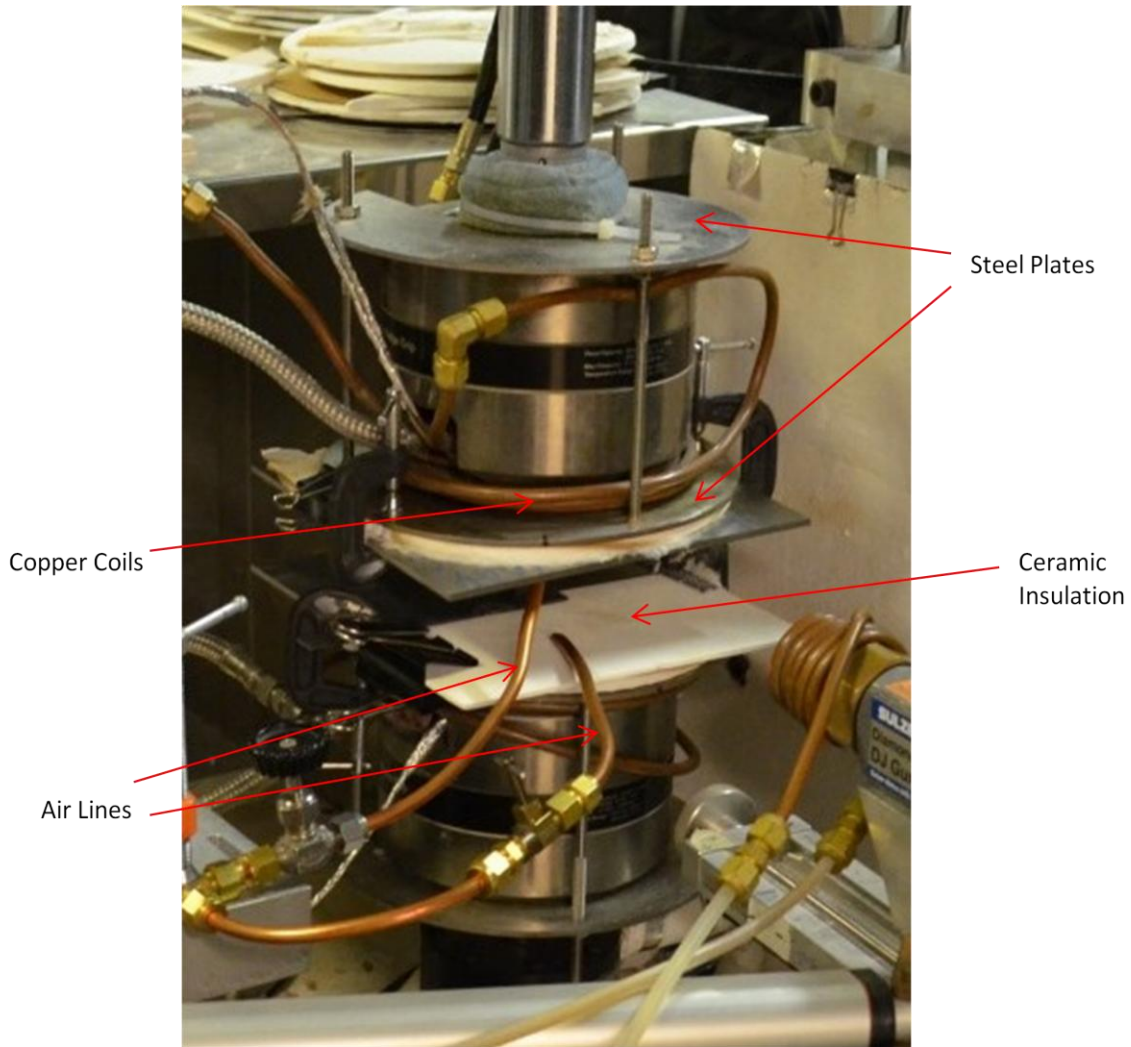
**Figure 8 - Material Test Stand**

Each specimen was gripped with a pair of MTS 647 hydraulic wedge grips. The grip hydraulic pressure used for all specimens was 10 MPa. The flame used to create the combustion environment created a problem with keeping the MTS grips cool, since the flame was un-contained and heat was able to reach the grips. In order to keep the grips cool, an insulating and cooling approach was used. The first technique employed for cooling the grips was copper coils wrapped around each grip held in place by steel plates. Chilled water was run through the copper coils. The water was chilled using a NESLAB RTE 7 chiller (Figure 9) to a temperature of 10°C.



**Figure 9 - NESLAB RTE 7 Chiller**

Since this experiment required higher temperatures than what was previously performed on this experimental setup, a few iterations were necessary to figure out what material would be best to insulate the grips. The material best suited to handle the higher temperature tests turned out to be an oxide CMC material (COI Ceramics Nextel A-N720). Even with the CMC material as insulation, there was still some erosion occurring on the insulating material near the specimen. To combat this, air at 50 psi was directed onto the insulation near the top and bottom of the specimen. Ceramic cloth insulation was also packed around the area where the specimen was gripped to provide further insulation for the hydraulic grips. Figure 10 shows the grip cooling and insulation techniques. Grip temperature during testing was monitored with a thermocouple at each grip. During testing the grip temperatures never exceeded 90°C which is well under the 177°C temperature limit of the grips.

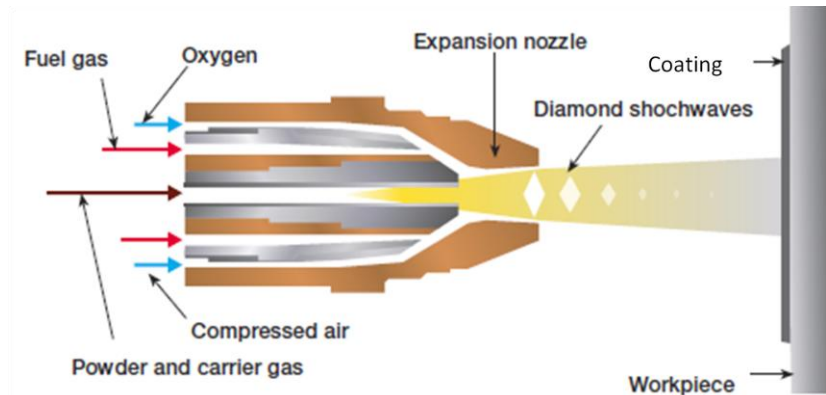


**Figure 10 - Grip Cooling/Insulation Scheme**

Load and grip cross head displacement data were collected during the fatigue tests. This data was collected by a Model 359 Transducer, which is a linear variable displacement transducer (LVDT). The LVDT reads the displacement of the upper grip and outputs it as a function of voltage. The grip displacement data was used in place of an extensometer. This was necessary because the high-speed flame makes it nearly impossible to install an extensometer and could create forces on the extensometer, which could result in erroneous strain data.

### 3.2.2. High-Velocity Oxygen-Fuel Flame System

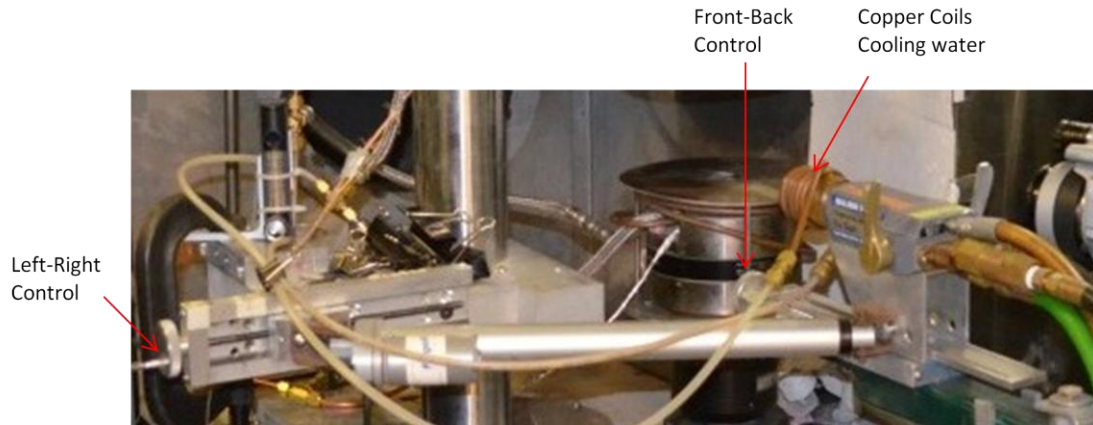
To create the combustion environment, a Sulzer Metco Diamond Jet (DJ) High-Velocity Oxygen Fuel (HVOF) spray gun system was used. The model used was the DJ9A with an air-cooled nozzle. This type of system is normally used for thermal spraying applications. The system uses oxygen, fuel, and air to create a supersonic jet. When used for powder spray application, the powder material and a carrier gas is injected into the jet and melts the powder to create a coating on the material. Figure 11 shows the nozzle of the HVOF spray gun when used for thermal spraying. For the present research, propane was used as the fuel and the powder and carrier gas line was not utilized. To supplement the compressed air cooling of the nozzle, copper coils were wrapped around the nozzle to feed chilled water to it [24].



**Figure 11 - HVOF Nozzle [9]**

The HVOF spray gun was attached to the MTS using a rail system that allows for front -back and left-right movement of the gun. The left-right control was used to aim the flame onto the specimen and front- back movement was used to control temperature. Figure 12 shows the HVOF spray gun mounted to the MTS.





**Figure 12 - HVOF Spray Gun Mount**

To control the gas flow of the flame gun, a DJF Diamond Jet Gas Flowmeter unit was used. The flowmeter unit consists of three rotameters to control oxygen, propane, and air flow independently. These three rotameters allow the accurate control of the amount of each gas being fed to the spray gun to control the flame being produced. Figure 13 shows the DJF gas flowmeter unit.



**Figure 13 - DJF Flowmeter Unit Used To Control Spray Gun**

The propane and oxygen tanks that supply the HVOF spray gun were located outside the laboratory building in a tank farm. There were two 120 gal propane tanks and two liquid oxygen tanks. It is necessary for the propane to be in a gaseous state for the HVOF spray gun to work properly so a Zimmer LPG vaporizer was used to ensure gaseous propane was supplied to the gun. The liquid oxygen containers are able to supply a max pressure of 350 psi of gaseous oxygen. The two containers were connected to a manifold that would draw from one tank at a time. The manifold would switch to the next container when the pressure supplied by the container being used would decrease to below 90 psi.

Since the HVOF spray gun produces a supersonic flame, there is a noise hazard associated with the operation of the gun. Fatigue testing required the gun to be run for long periods of time so it was necessary to contain the sound. To accomplish this, a WhisperRoom SE2000 series sound room was used to contain the MTS machine and HVOF spray gun. Exhaust ducts were added to the room to remove gas products and heat produced by the flame from the room. An HFC-227ea fire suppression system was also installed the room because of the fire hazard associated with an open flame. Figure 14 shows the whisper room.



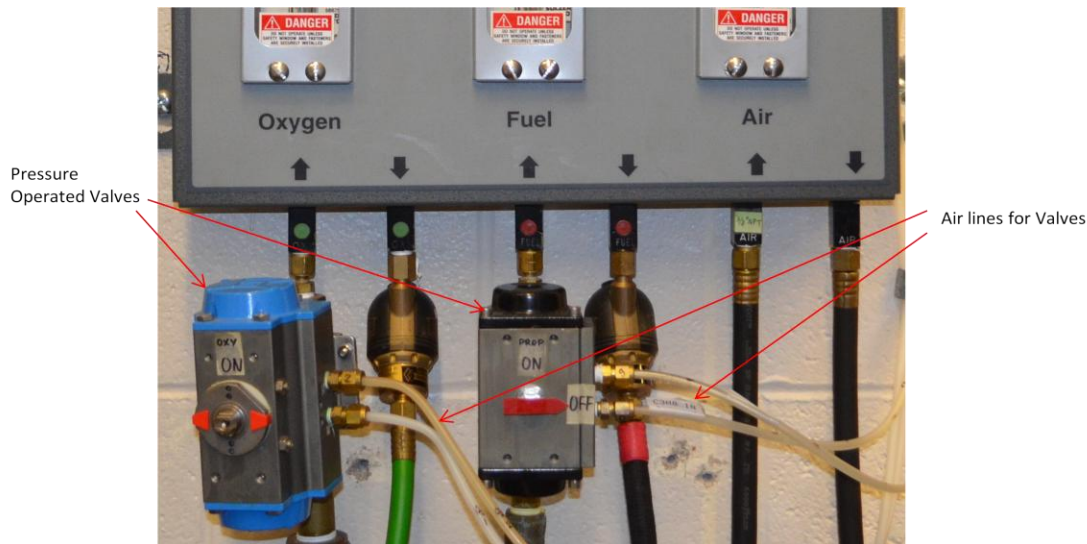


**Figure 14 - Whisper Room Containing Burner Rig Test Setup**

### **3.2.3. Safety Shutdown System**

The use of the HVOF spray gun in a contained environment presents some issues regarding safety such as having combustible gases in a closed space. To mitigate these safety risks, an emergency shut-down system was put in place. The safety shut-down system was controlled by National Instruments LabVIEW 8.2 software.

The LabVIEW software takes in inputs from a National Instruments data acquisition board, and uses limits set in the software to control electro-pneumatic pressure transducers that supply compressed air to pressure-operated valves on the oxygen and propane gas lines. Figure 15 shows the pressure-operated valves installed on the oxygen and propane lines .



**Figure 15 - Pressure-Operated Valves for Oxygen and Propane**

The inputs to the LabVIEW software are thermocouples placed in the whisper room and the LVDT voltage. If the temperature from any of the thermocouples exceeds a set limit in the LabVIEW program, the air pressure being supplied to the valves would be shut off, which would close the pressure operated valves and extinguish the flame. Additionally, if the LVDT voltage exceeds a certain value, which would indicate a failure of the specimen, the pressure-operated valves would close. Airflow operated switches installed in the exhaust duct would also trigger the pressure-operated valves to close in the event of a failure of the exhaust system. As an added layer of safety, there was also a manual emergency button that would shut off power to the pressure transducers and close the pressure-operated valves.

### **3.2.4. Forward-Looking Infrared System**

To measure the temperature of the specimens during testing, an indirect measurement technique had to be employed because it was not possible to directly measure the temperature of the specimen due to the combustion environment. The high

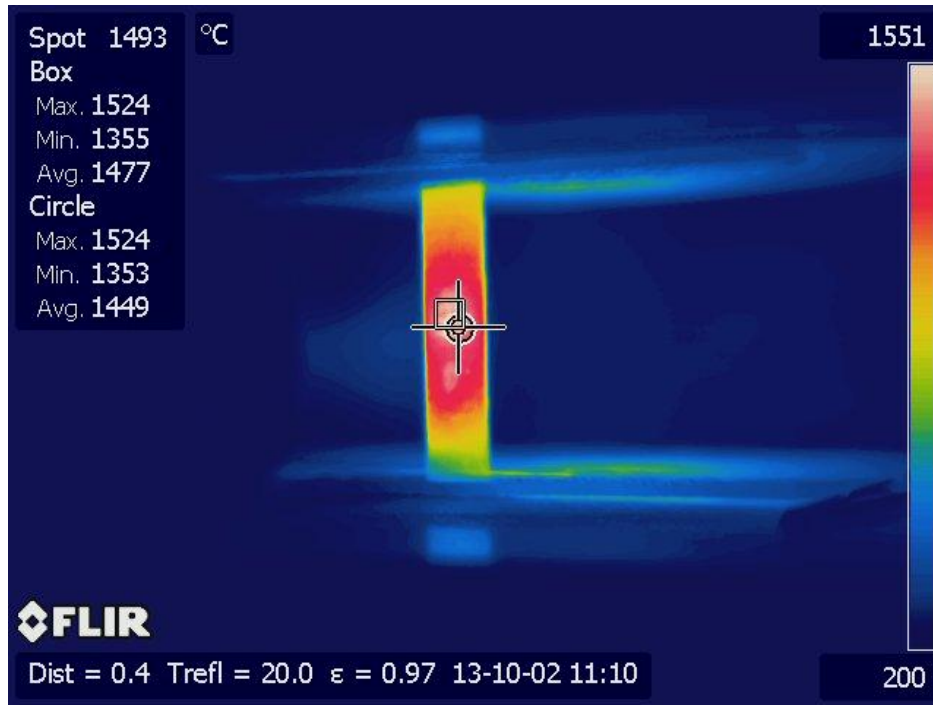
speed flame and high temperatures did not allow for the use of a thermocouple to measure temperature directly. To accomplish this, a Forward Looking Infrared (FLIR) system was employed. The FLIR camera system used for this research was a ThermaCAM P640 manufactured by FLIR Systems Inc. (Willsonville, OR). The FLIR camera was used to monitor the temperature of the front of the specimen. The ThermaCAM P640 has a 640x480 pixel infrared detector, with  $\pm 2\%$  accuracy. The camera is capable of measuring temperatures in a range from -40 to 2000°C. The detector also has a spectral range of 7.5 to 13  $\mu\text{m}$ , with a minimum focus distance of 0.3 m. The thermal sensitivity of the camera is 55mK at 30° C. Figure 1 shows the FLIR camera [5].



**Figure 16 - FLIR Camera In Mount**

To obtain maximum accuracy during temperature measurement, it is important to record the ambient temperature and humidity in the test area. The camera settings allow for the input of these data points in order to get a more accurate temperature reading from the camera. A Springfield Instruments Temperature and Humidity Monitor was used inside the Whisper Room to record temperature and humidity data. The room temperature and humidity data is included in Table 6.

The built-in camera software has multiple ways to monitor and record temperature while in operation. To monitor and record the temperature of an area of interest in the camera's field of view, there are spot and area measurement modes. The spot mode measures the temperature in a spot selected by the user. The area modes consist of either a circle or square area. The size and position of the circle or square is controlled by the user. The camera records and displays the maximum, minimum, and average temperatures in the area designated [5]. During testing, the spot, circle, and square measurements were all monitored and recorded. All three were placed at the center where the flame was impinging on the specimen unless there was something of interest at a location away from the center of the specimen. Figure 17 shows an example of the output from the FLIR camera. In this case, the box area measurement tool is slightly off-center to monitor an area of interest.



**Figure 17 - FLIR Camera Output During Testing**

Thermacam software was used to analyze FLIR camera images after testing was completed. The Thermacam software is embedded into Microsoft Word and allows the user to measure temperature in different areas, produce temperature profile graphs, adjust the temperature range of the image, and change the parameters of the image if necessary.

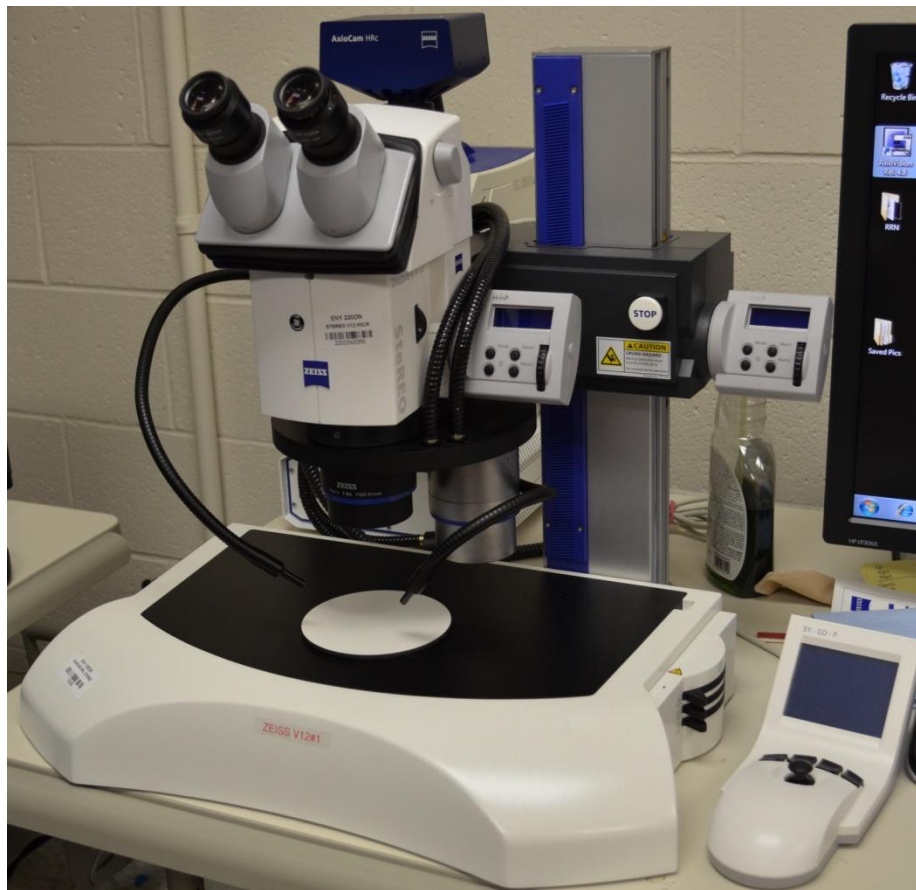
To measure temperature from an IR signature, it is important to consider thermal emissivity. The thermal emissivity of a material is its ability to emit energy in the form of radiation. Thermal emissivity is measured by a dimensionless quantity,  $\epsilon$ , where the thermal emissivity of a true black body is equal to one. The FLIR camera used in this research allows for the input of a thermal emissivity. During the course of this research, the value used was:  $\epsilon = 0.97$ . This value was determined based on previous research



done on a similar material [13]. With an emissivity error of  $\pm 0.02$ , the error in temperature would be  $\pm 20^{\circ}\text{C}$  which is within the range of temperature fluctuations during testing due to the nature of the flame gun operation.

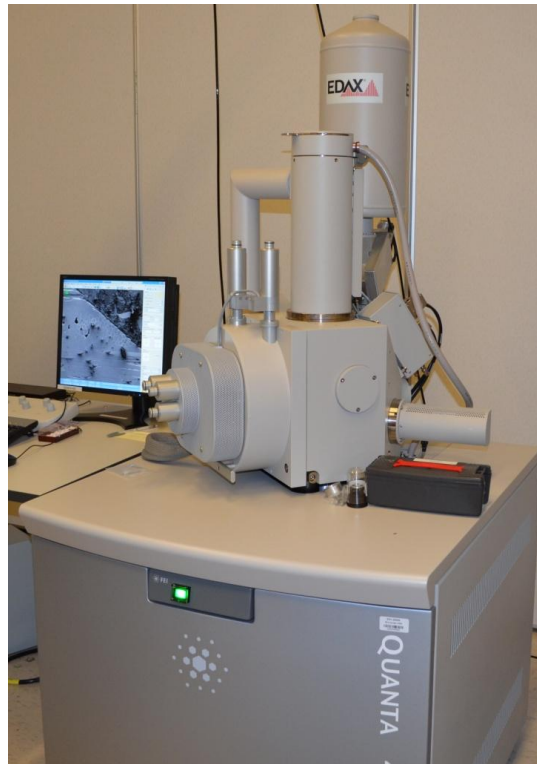
### 3.2.5. Specimen Imaging Equipment

All specimens were imaged with a low power microscope after testing to observe the fracture surfaces and identify flaws in the material. The images were obtained using a Zeiss Discovery V12 microscope with an attached Zeiss Axiocam HRc. Figure 18 shows the optical microscope used for the current research.



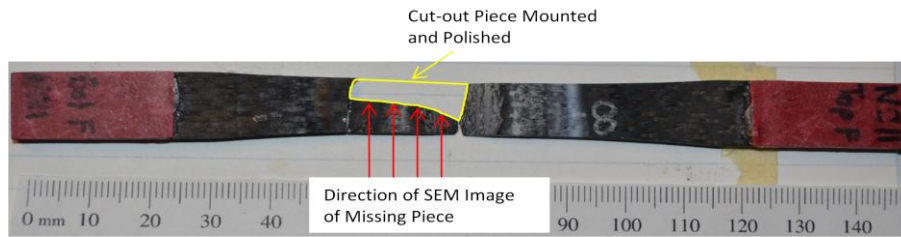
**Figure 18 - Optical Microscope Used to Image Specimens**

To further investigate the microstructure of the material after fatigue testing, a scanning electron microscope (SEM) was used to obtain images of higher magnification than what is possible with the optical microscope. The SEM used for this research was a Quanta 200. An SEM image is formed by a focused electron beam that scans over the surface area of the specimen. The signal electrons emitted from the specimen are collected by a detector, amplified, and used to reconstruct an image according to a one-to-one correlation between scanning points on the specimen and picture points on a screen such as a liquid crystal display to produce an image that can be analyzed [15]. Figure 19 shows the SEM used during this research.

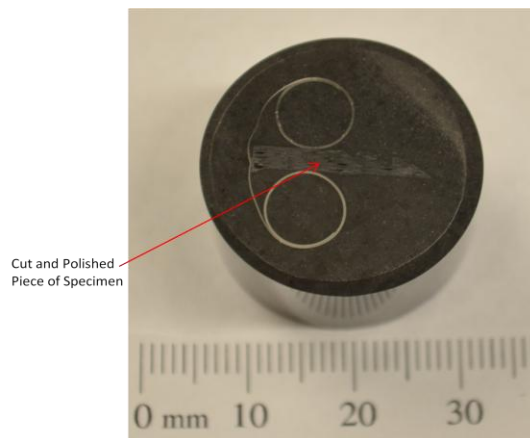


**Figure 19 - SEM Used to Image Specimens**

Sometimes it is necessary to coat specimens with a thin layer of conductive material to ensure good images can be obtained with the SEM. This was not the case for the material tested during this research. The material was conductive enough to obtain good images with no coating. Specimen preparation for the SEM consisted of cutting the fractured specimen to fit in the SEM and mounting the cut piece to a specimen holder. The specimen that survived the longest at the highest temperature (specimen N811, 1480°C, 16.67 hrs) was chosen to observe any phenomenon occurring within the material down the length of the specimen away from the area of the flame. To do this, the specimen was cut as shown in Figure 20 and then mounted and polished as shown in Figure 21 to be imaged in the SEM.



**Figure 20 - Cut-out of Specimen N811 for SEM Imaging**



**Figure 21 - Specimen Mounted and Polished for SEM**



### 3.3. Test Procedure

This chapter describes the procedures used during testing of the material. Microsoft Excel was used to collect and analyze the data collected during the experiments.

#### 3.3.1. Specimen Inspection and Processing

Each specimen was inspected for major flaws such as edge damage or roughness that could have occurred during the water cutting process. The width and thickness of each specimen was measured with digital calipers at the thinnest region of the dog-bone. These measurements were used to calculate the cross-sectional area of the specimen using the following formula:

$$A = w * t$$

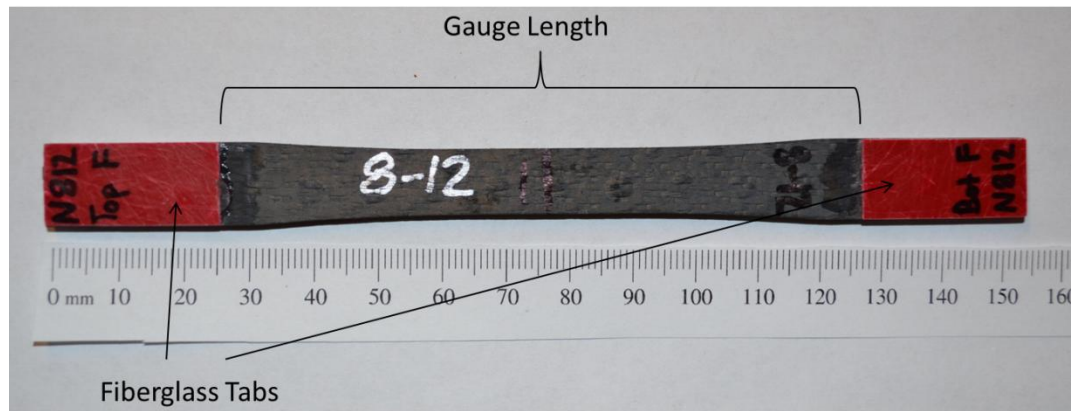
Where  $w$  is the width and  $t$  is the thickness of the specimen. The following formula was used to calculate the stress at the measured cross-sectional area:

$$\sigma = \frac{P}{A}$$

Where  $A$  is the cross-sectional area and  $P$  is the axial load placed on the specimen.

In order to prevent the grips on the MTS machine from causing damage to the specimen during the experiment, it was necessary to install tabs on the specimens at the grip locations. The tabs used were fabricated from a glass fabric/epoxy material. The tabs were secured to the specimens using M-Bond 200 adhesive. This adhesive is a two-part adhesive, so the catalyst was applied to both the specimen and the fiberglass tabs first. Then, the adhesive was applied to the tabs. Once the tabs were secured, the

specimens were placed in a vice under pressure to ensure a good bond between the tabs and the specimens.



**Figure 22 - Specimen Prepared for Testing**

Once the tabs were applied, the gauge length of the specimen was measured. This measurement was used to record changes in displacement during testing measured by the LVDT. The weight of each specimen was recorded after the fiberglass tabs were applied to be compared with the weight after testing was accomplished.

### **3.3.2. Equipment Start-up and Specimen Loading**

Before starting an experiment, the hydraulic pump for the MTS was turned on and allowed to warm up. The Multi-Purpose Testware (MPT) was loaded onto the workstation as well as the LabVIEW control system software. The MTS procedure was edited as per the required loading conditions for the specific test and then loaded into the MPT. The specimen file name, data acquisition rate, and data file destination was also selected.

At this point, the specimen was ready to be installed in the MTS machine. To accomplish this, the grips on the MTS were placed in the open position and in displacement control mode so the upper grip could be moved into a position to allow the specimen to be placed between the grips. The specimen was secured in the upper grip first. The specimen was placed in the upper grip so that the left edge (when looking at the front of the MTS) was touching the alignment tool. The alignment tool is used to ensure that the specimen is installed as vertical as possible in the MTS grips. There is an alignment tool on both the upper and lower grip. The upper grip would then be closed, and the specimen was inspected using a mirror and flashlight to ensure that the specimen tabs were gripped completely. This is necessary because of the steel plates installed on the MTS grips for thermal insulation purposes. The upper grip would then be lowered under displacement control until the lower specimen tabs were within the lower grips of the MTS. At this point, the upper grip was opened enough to allow the specimen to be placed against the alignment tool on the lower grip as well as the upper grip. The lower grip was then closed with the upper grip still open to ensure the specimen tabs were fully gripped. The lower grip was opened and the upper grip was closed while being careful to not allow any vertical movement of the specimen. The MTS was set to "force command" and the commanded force was zeroed out before closing the lower grip. This was done to prevent the specimen from being unintentionally compressed. A flashlight and mirror was again used to verify that the specimen was gripped correctly. A small bubble level was used to confirm the vertical alignment of the specimen as well. Once the specimen was installed in the MTS, insulation was placed to protect the hydraulic grips from the high temperatures created by the HVOF. Ceramic fabric

insulation was stuffed into the holes in the steel plates covering the grips. Ceramic plates were then installed covering the steel plates. The ceramic plates were secured with clamps to keep them from moving during the experiment. The cooling air setup was then installed.

### **3.3.3 HVOF and Temperature Measurement Start-up**

The Zimmer LPG vaporizer was turned on first to gasify the liquid propane. The liquid propane and liquid oxygen tanks were then opened. The NESLAB chiller was then turned on to allow the MTS grips and the HVOF spray gun nozzle to cool to a temperature of 10°C at the start of testing. The FLIR camera was turned on, and the ambient temperature and humidity settings were adjusted to the values measured inside the whisper room. The two exhaust fans were turned on and the LabVIEW control system is started to begin recording temperature data and allow the compressed air valves for the oxygen and propane to open. Figure 23 shows the LabVIEW software display screen before the start of testing. The valve for the cooling air system was then opened.



**Figure 23 - LabVIEW Software Display Before Start of Test**

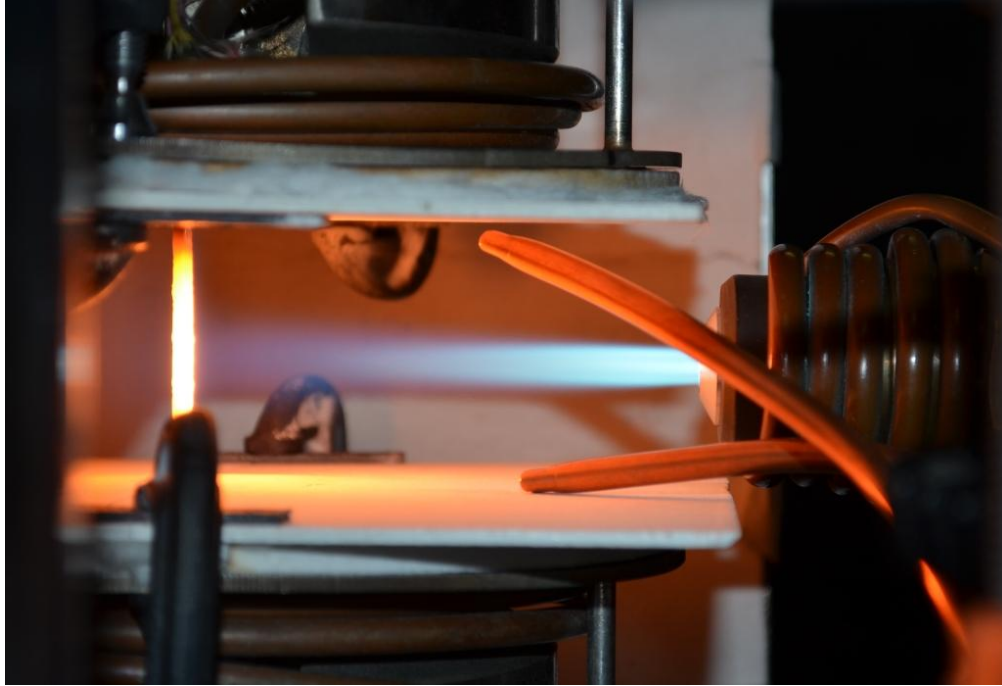
Once the propane had been vaporized enough to reach a pressure of about 50 psi before the regulator for the HVOF, the oxygen, propane, and air valves to the regulators and flowmeters were turned on. The spray gun was pointed away from the specimen before lighting the flame. This was done to ensure an obstacle-free path for the flame to start and stabilize. The cooling air valve was then opened. Then the spray gun valve was opened and the flame was lit and allowed to stabilize. The flow parameters were checked and adjusted as necessary at this point.

Table 1 contains the range of flow rates and the pressures used for this research. The heat output is estimated to be near 18 kW. This is based on calculations performed during the original setup of the test apparatus [14].

**Table 1 - HVOF Gas Pressures and Range of Flow Rates**

<b>Gas</b>	<b>Flow Rate (scfh)</b>	<b>Pressure (PSI)</b>
Oxygen	220 - 230	45
Propane	50 - 75	20
Air	364 - 368	30

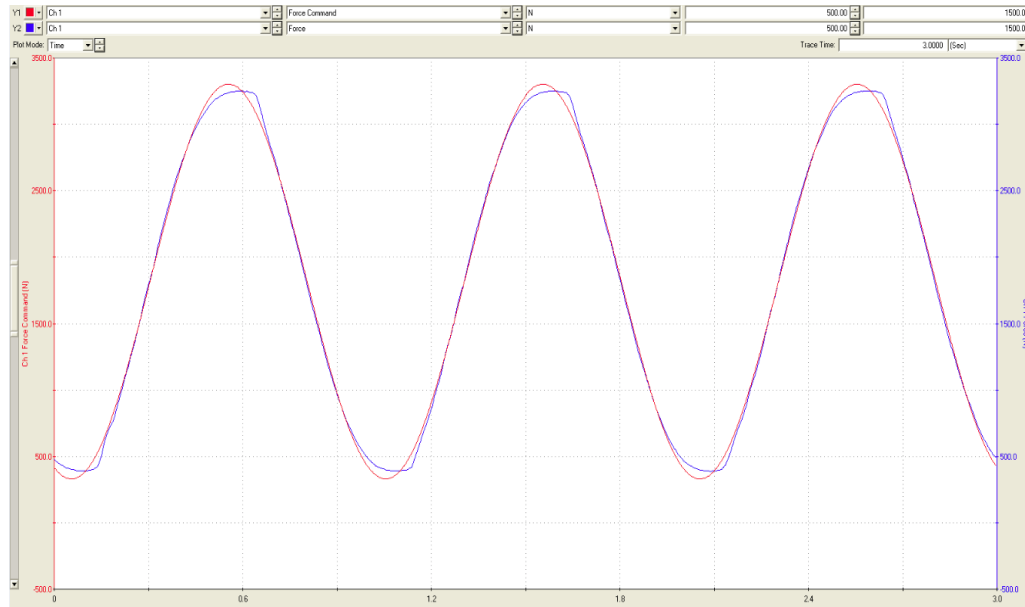
After the flame was stable and at the correct parameters, the gun was slowly moved in position to achieve the required specimen temperature. Figure 24 shows the flame gun in position and heating a specimen. The FLIR camera was used to determine when the correct temperature was reached. To control the temperature, the flame gun was moved closer or farther away from the specimen. Since the experimental setup was originally designed to achieve a surface temperature of 1250°C, it was not possible to move the flame close enough to the specimen for the higher temperatures due to the insulation and cooling scheme required for the MTS grips. To achieve the higher specimen surface temperatures such as 1480°C, it was sometimes necessary to adjust the flow of propane to increase the temperature of the flame. Once the correct temperature of the specimen was reached, the FLIR camera was programmed to record an image every ten minutes.



**Figure 24 - Flame Gun In Operation**

#### **3.3.4. Fatigue Tests**










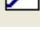
All of the specimens tested were loaded under a tension-tension fatigue test sequence while in the combustion environment provided by the HVOF spray gun. The fatigue loading was applied with a 1Hz sinusoidal wave. The stress ratio used for all tests was 0.1. To ensure the loads applied by the MTS matched the commanded loads as closely as possible, Peak/Valley Compensation (PVC) was used. Figure 25 shows a screen shot of the cyclic loading during testing. The red curve is the force commanded by the MTS control system versus time and the blue curve represents the actual force seen by the specimen versus time.



**Figure 25 - Cyclic Fatigue Loading With PVC**

During fatigue testing, time and date, test run-time, maximum and minimum force, cross-head displacement, and cycle count data was collected. Hysteresis and peak and valley data collection modes were used for collecting fatigue data. The peak and valley data collection gathered the maximum and minimum force and displacement data for each cycle throughout testing. The hysteresis data was collected on log cycles. Both were recorded at a rate of 1024 Hz. The force ramp-up data before the fatigue testing began was also recorded. The fatigue run-out for this testing was at 90,000 cycles, which is 25 hours. This threshold was decided on because this is the amount of time the hot section of a turbine engine in an aircraft application will see the maximum temperatures during the life of the engine. Figure 26 shows the MPT procedure used for conducting fatigue tests.



Type	Name	Start	Interrupt
	Initial Conditions	<Procedure>.Start	
	Failure	Initial Conditions.Done	
	Ramp Up	Initial Conditions.Done	
	Monitor Ramp Up	Initial Conditions.Done	Ramp Up.Done
	Test Termination Criterion	Ramp Up.Done	
	counter	Ramp Up.Done	
	LCF	Ramp Up.Done	Test Termination Criterion.Done
	Cyclic DAQ	Ramp Up.Done	Test Termination Criterion.Done
	peak and valley acquisition	counter.Buffer Full	Test Termination Criterion.Done
	Disp to -25 mm after failure	Test Termination Criterion.Done	

**Figure 26 - MPT Procedure for Fatigue Tests**

### 3.3.5. Residual Strength Tests

It was of interest to investigate the retained strength of the specimens that made it to the run-out condition. To accomplish this, tensile tests were performed on these specimens. The testing was performed on an MTS 810 test stand. Load data was collected with an MTS 661 Force Transducer. To collect strain data, an MTS 632.53E-14 extensometer was used. The extensometer was placed directly on the specimen and held in place by spring tension. The monotonic testing used a force control rate of 42.5 N/sec. The load and strain data were collected at 10 Hz until specimen failure.

### 3.4 Test Matrix

Table 2 contains the test matrix used for the combustion environment fatigue testing conducted during this research.

**Table 2 - Fatigue Test Matrix**

<b>Spec. ID</b>	<b>Temp. (°C)</b>	<b>Stress (MPa)</b>
<i>N82</i>	1480	210
<i>N83</i>	1350	210
<i>N84</i>	1250	210
<i>N85</i>	1250	175
<i>N86</i>	1250	125
<i>N87</i>	1480	175
<i>N88</i>	1480	125
<i>N810</i>	1480	80
<i>N811</i>	1480	0
<i>N812</i>	1350	125
<i>N813</i>	1350	90

## **IV. Analysis and Results**

### **Chapter Overview**

This chapter presents the results and analysis of the fatigue testing of the CMC in the combustion environment.

#### **4.1. Specimen Temperatures in Testing**

Since the combustion of the flame is a harsh and turbulent environment, it is difficult to maintain a temperature with more than  $\pm 20^{\circ}\text{C}$  accuracy on the surface of the specimen. The temperature of the front surface of the specimen was recorded using the FLIR camera by taking IR images about every ten minutes during a test. An average, maximum, and minimum temperature in a circular area of  $17\text{ mm}^2$  and a square area of  $21\text{ mm}^2$  was recorded with each image. To get an overall average, maximum, and minimum temperature each specimen endured during testing, the average was taken of each temperature of the temperatures previously mentioned that were recorded in ten minute intervals. Table 3 and Table 4 contain the temperatures each specimen was subjected to during testing. Table 3 contains the average of the maximum, minimum, and average temperature recorded in the box area on the FLIR camera for each specimen for the entire length of test.

**Table 3 - Average, Max, and Min Temperatures for Box Area for Each Specimen**

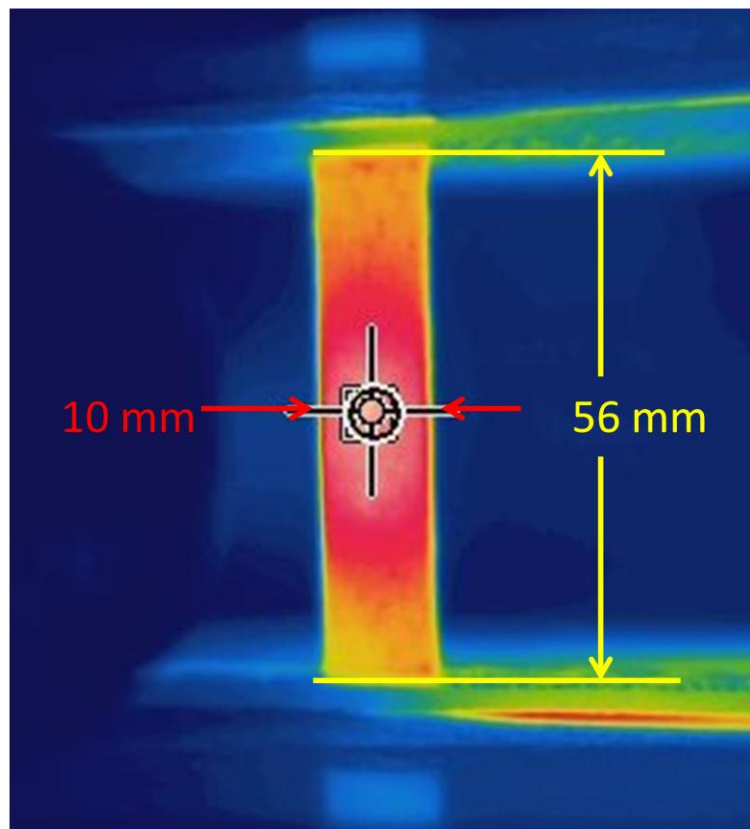
<b>Specimen ID</b>	<b>Maximum (°C)</b>	<b>Minimum (°C)</b>	<b>Average (°C)</b>	<b>Target Temperature(°C)</b>
<i>N82</i>	1464	1346	1412	1480
<i>N83</i>	1591	1230	1271	1350
<i>N84</i>	1309	1197	1237	1250
<i>N85</i>	1296	1200	1237	1250
<i>N86</i>	1294	1192	1235	1250
<i>N87</i>	1458	1384	1420	1480
<i>N88</i>	1523	1363	1459	1480
<i>N810</i>	1524	1389	1463	1480
<i>N811</i>	1523	1386	1463	1480
<i>N812</i>	1443	1297	1347	1350
<i>N813</i>	1405	1294	1345	1350

Table 4 contains the average of the maximum, minimum, and average temperature recorded in the circle area on the FLIR camera for each specimen for the entire length of test.

**Table 4 - Average, Max, and Mix Temperatures for Circle Area for Each Specimen**

<b>Specimen ID</b>	<b>Maximum (°C)</b>	<b>Minimum (°C)</b>	<b>Average (°C)</b>	<b>Target Temperature(°C)</b>
<i>N82</i>	1469	1349	1408	1480
<i>N83</i>	1605	1234	1273	1350
<i>N84</i>	1309	1198	1237	1250
<i>N85</i>	1296	1202	1238	1250
<i>N86</i>	1297	1203	1237	1250
<i>N87</i>	1456	1377	1419	1480
<i>N88</i>	1521	1359	1440	1480
<i>N810</i>	1513	1389	1455	1480
<i>N811</i>	1519	1324	1446	1480
<i>N812</i>	1443	1300	1345	1350
<i>N813</i>	1405	1294	1345	1350

Figure 28 through Figure 38 show the temperature profile of each specimen during testing from images taken by the FLIR camera. For each image, a temperature profile was measured down the length of the specimen from top to bottom at the center and across the width of the specimen at the center. The graph below each IR image shows the temperature along the line associated with each profile. The length of the specimen that is visible in the IR image between the insulation was between 42 mm and 56 mm depending on the exact insulation setup used for that particular test. The width of each specimen was 10 mm at the center of the specimen. Figure 27 shows the measurements of the exposed area of specimen N88 as an example.



**Figure 27 - Specimen N88 IR Image With Measurements**

Figure 28 shows the temperature profile down the length and across the center of specimen N82. The target temperature for this specimen was 1480°C. The profiles show an increase in temperature at the center of the specimen where the flame is impinging on the specimen. This material does appear to conduct heat well, so the far ends of the specimen were at temperatures near 1200°C

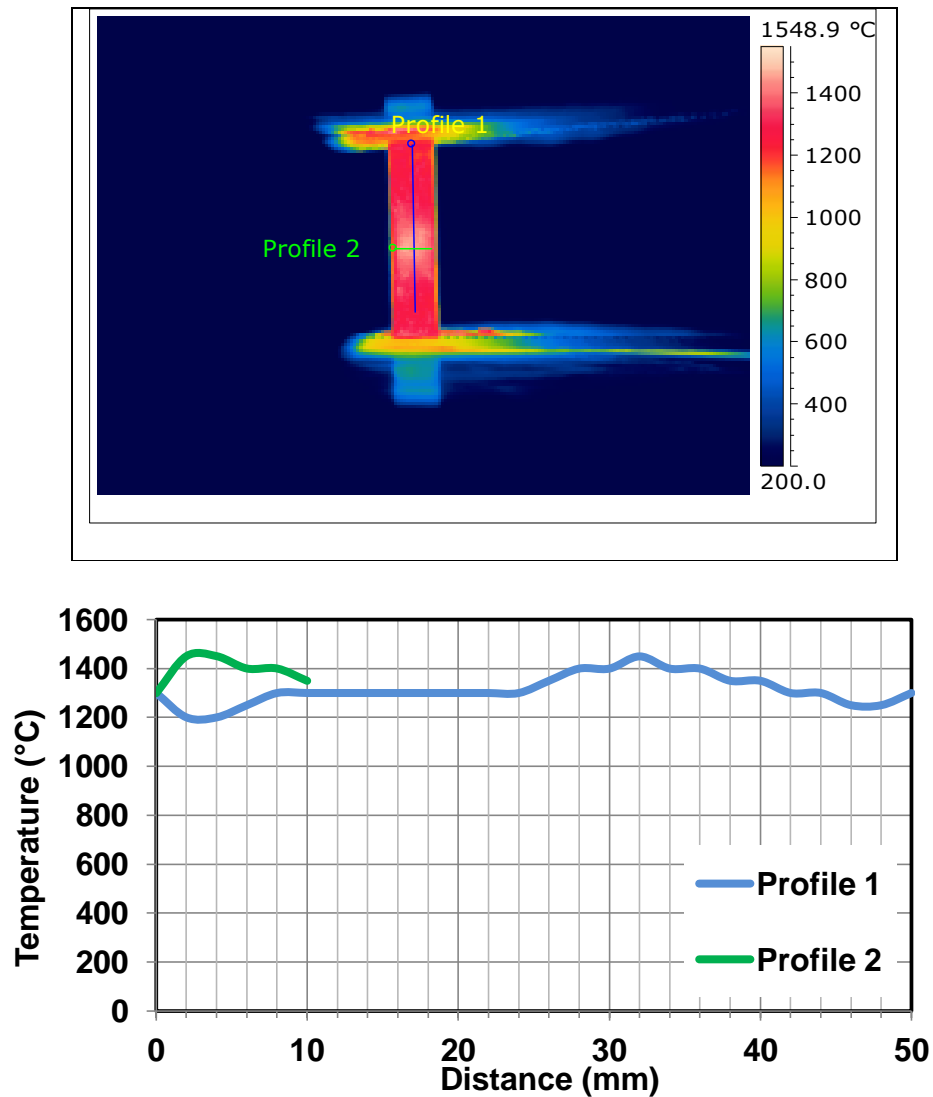


Figure 28 - Temperature Profile Specimen N82

Figure 29 shows the temperature profiles of specimen N83. The target temperature of this specimen was 1350°C. In this IR image, there are some of hot spots on the surface of the specimen that appear white in color on the image. One of the spots are evident in a spike in the temperature profile. There is not a significant drop-off in temperature at the edges of the specimen due to the thermal conductivity of the specimen.

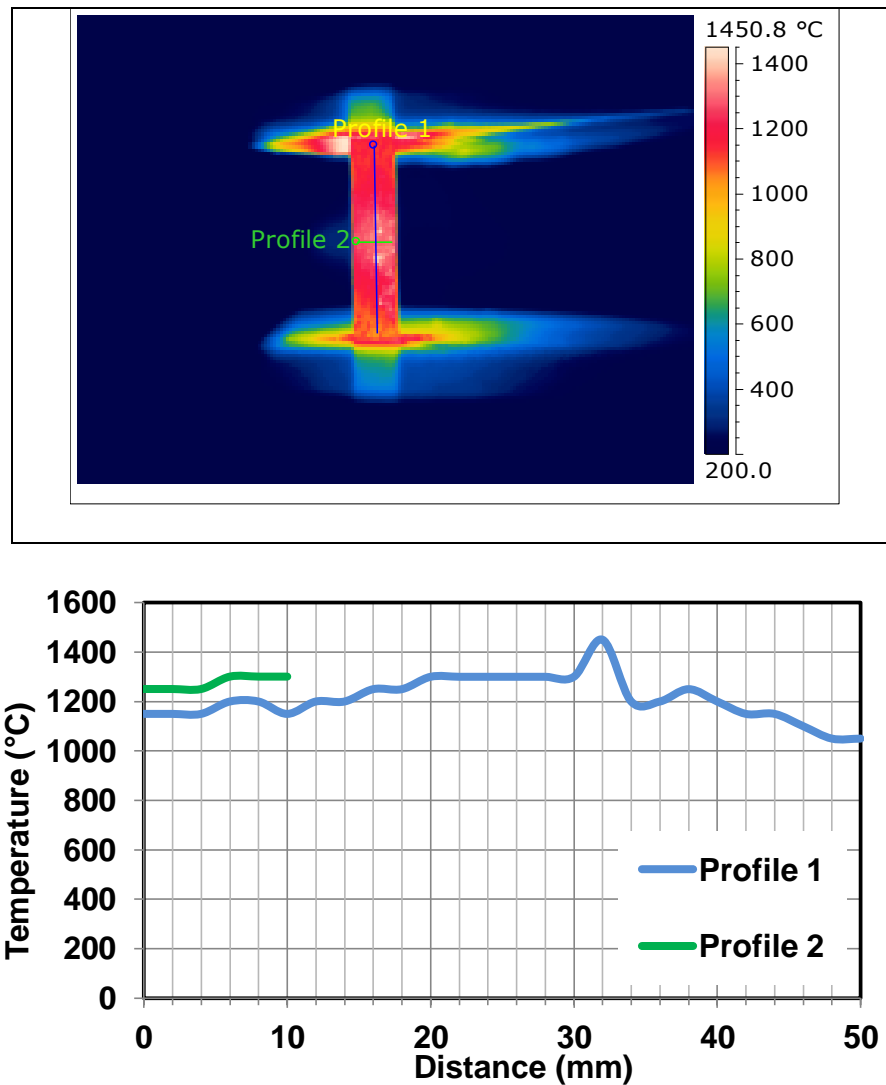


Figure 29 - Temperature Profile Specimen N83

Figure 30 contains the temperature profile of specimen N84. The target temperature for this specimen was 1250°C. The temperature on the surface of this specimen was relatively uniform at above 1200°C through most of the length of the specimen with the center near 1250°C.

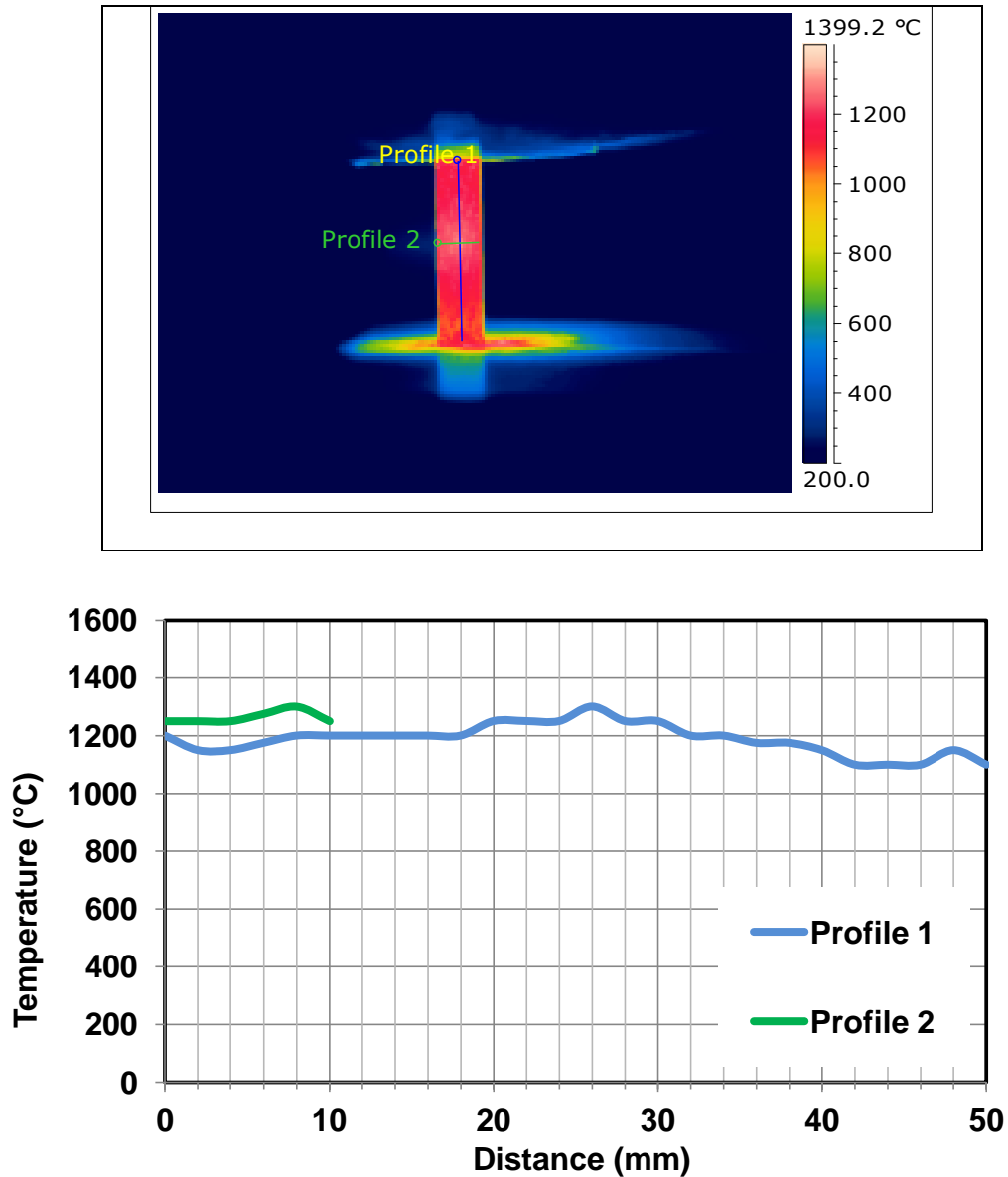


Figure 30 - Temperature Profile Specimen N84



Figure 31 contains the temperature profiles and IR image of specimen N85. This specimen was tested at a target temperature of 1250°C. The temperature profiles for this specimen were similar to the profiles of the previous specimen.

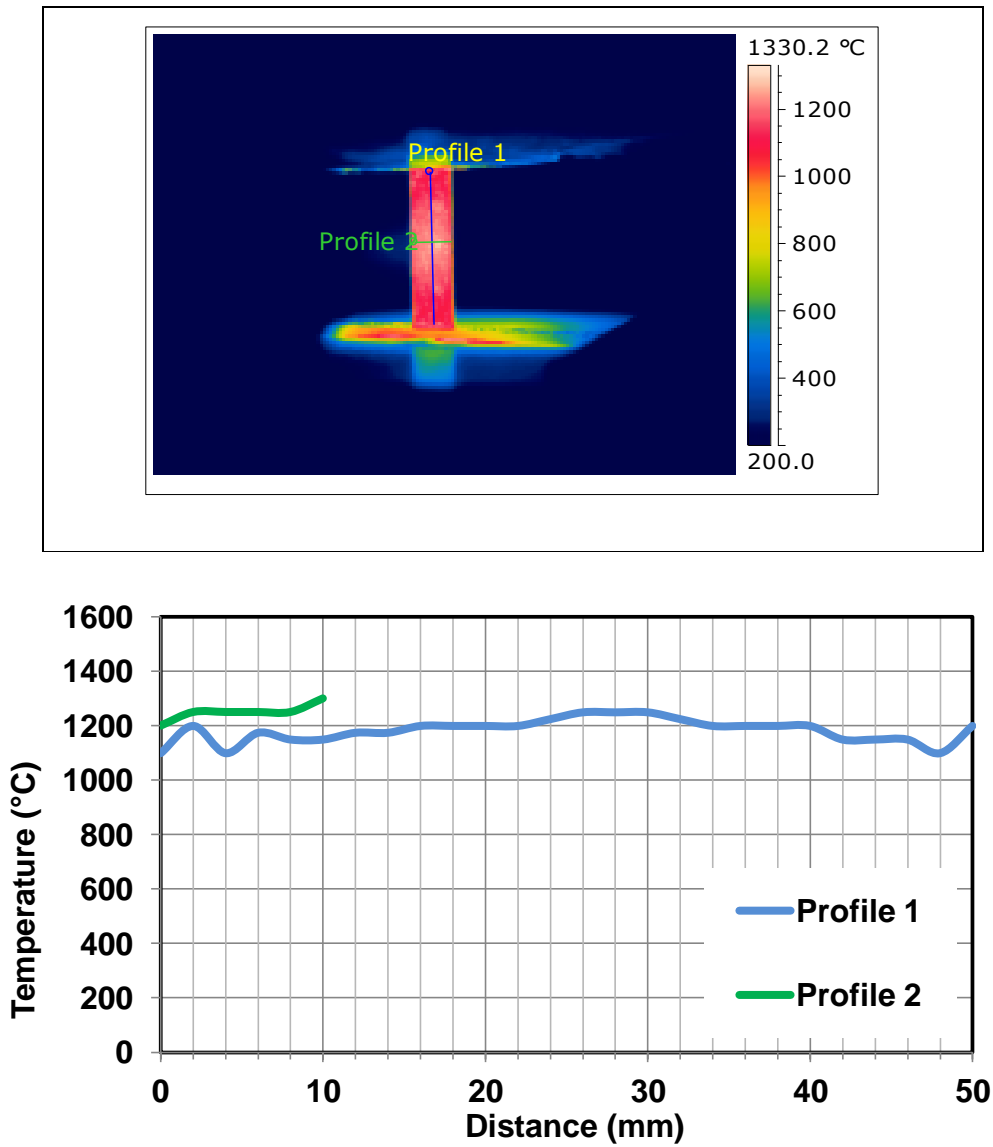


Figure 31 - Temperature Profile Specimen N85

Figure 32 shows the temperature profiles with the associated IR image of specimen N86. The target temperature for this specimen was 1250°C. The temperature profiles for this specimen are similar to the profiles for the two previous specimens.

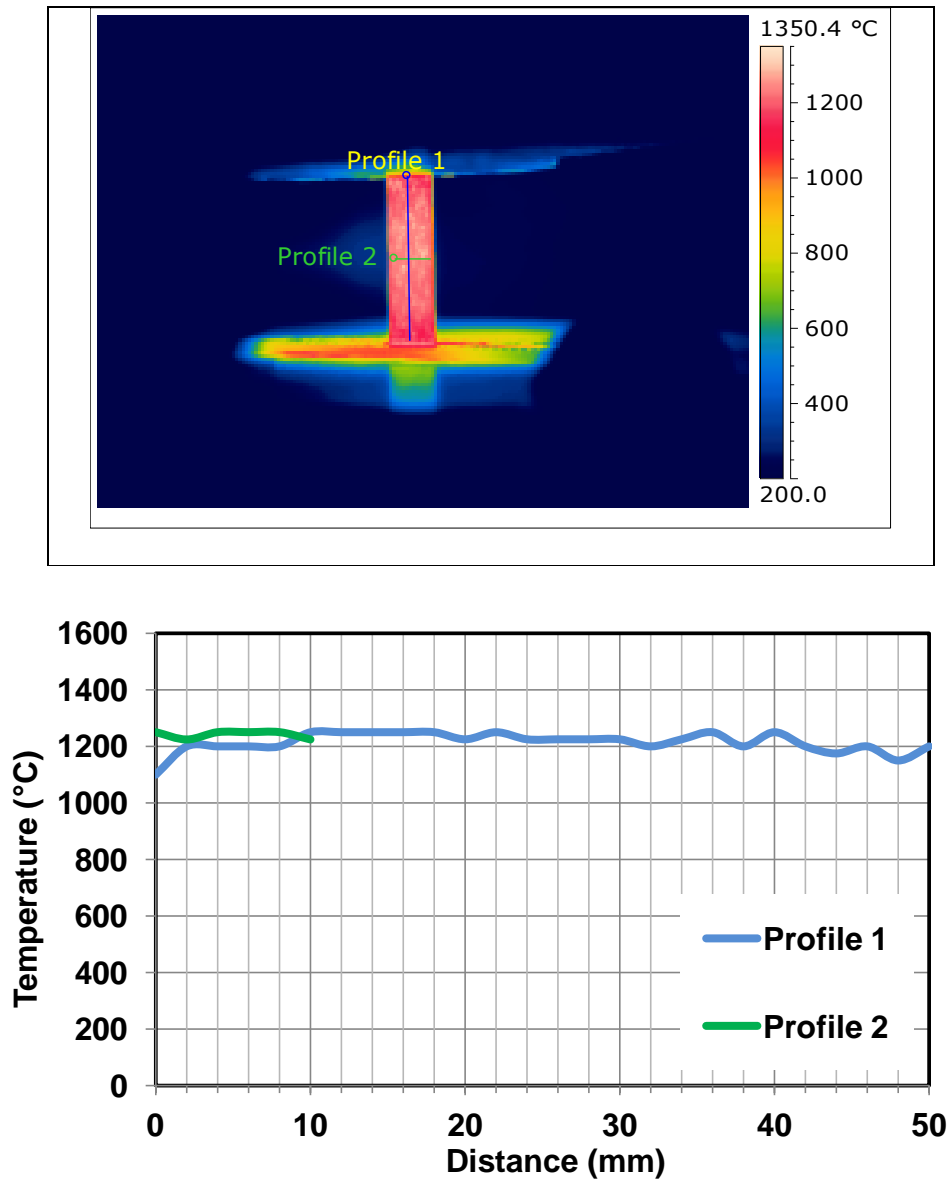


Figure 32 - Temperature Profile Specimen N86

Figure 33 shows the temperature profiles for specimen N87. The target temperature for this specimen was 1480°C. The profile from top to bottom on this specimen differs from the previous specimens due to a change in the grip cooling scheme. To better cool the grips, air was directed at the very top and very bottom of the specimen to protect the grips from the heat conducted by the specimen. The average temperature on the surface of the specimen was still able to be maintained near the target temperature. The rest of the specimens tested after this point also show this characteristic because the cooling air was used throughout the remaining testing.

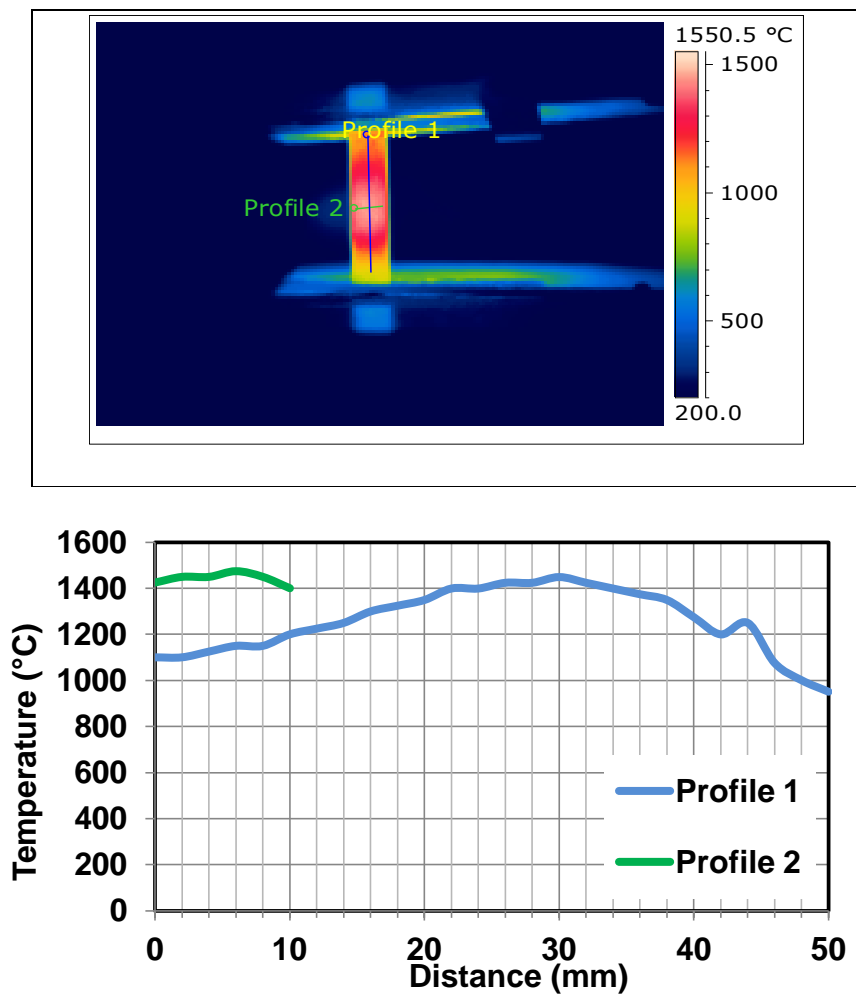
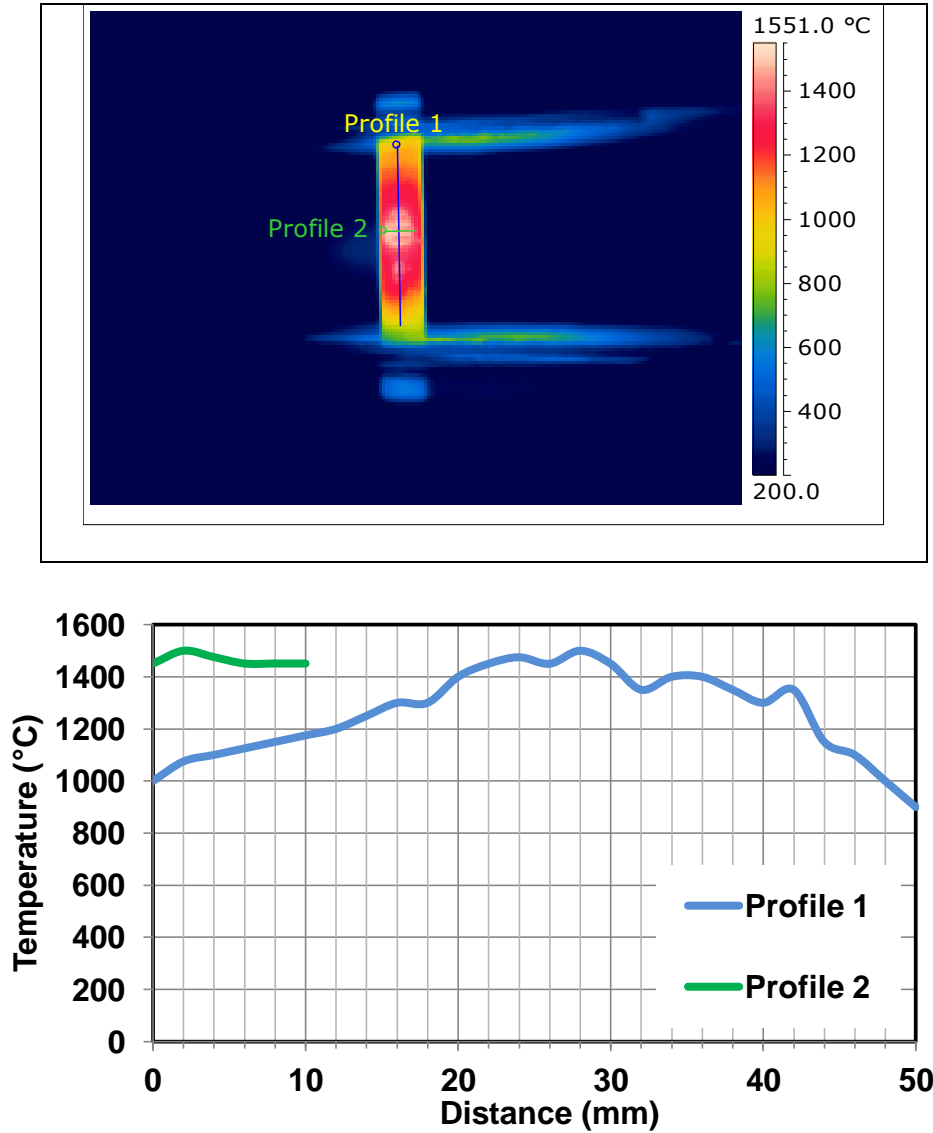


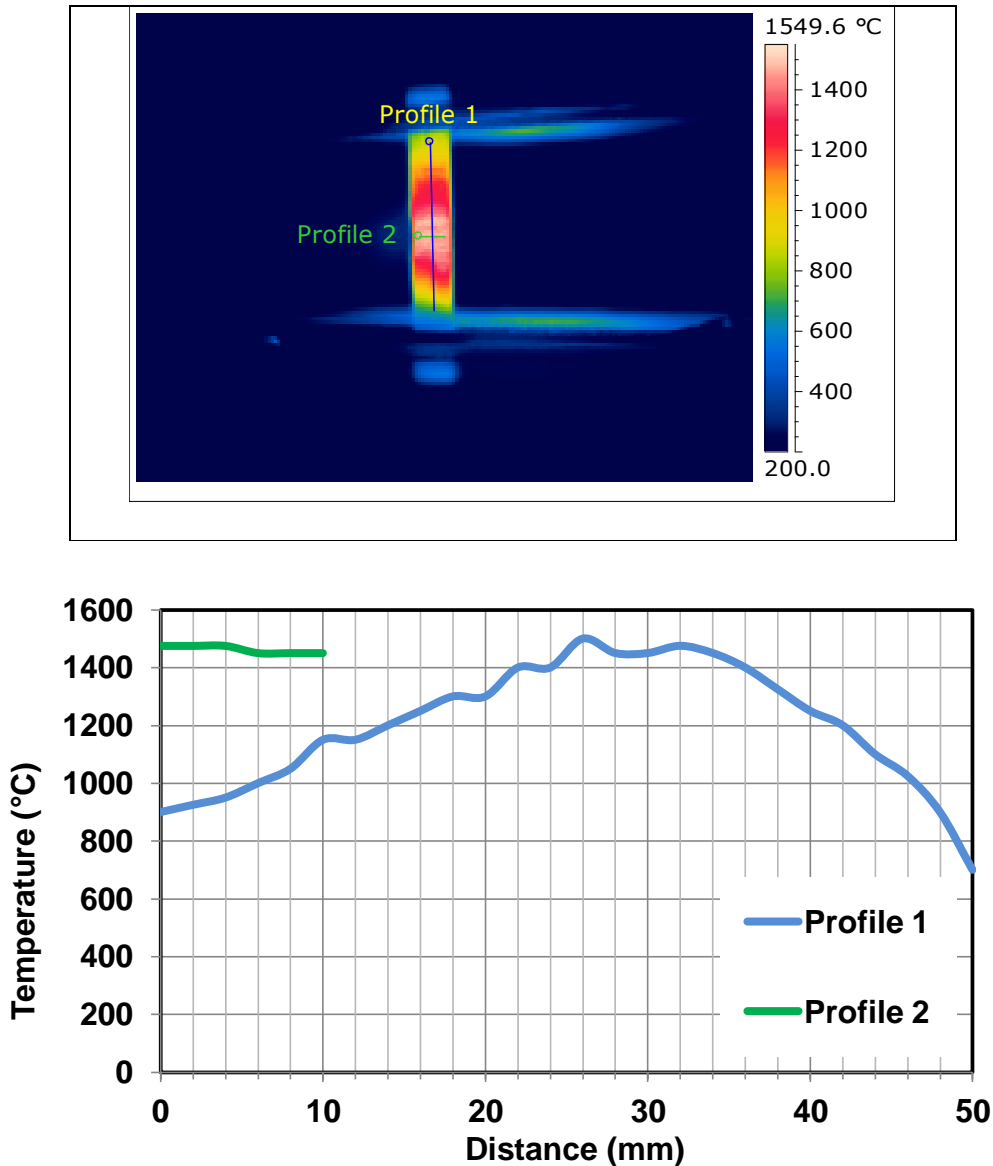
Figure 33 - Temperature Profile Specimen N87

Figure 34 shows the temperature profile of specimen N88. The target temperature for this specimen was 1480°C. The profiles are similar to the profiles of the previous specimen. The area in the center of the specimen that is at the hottest temperatures corresponds to an area of a loss of material on the surface of the specimen (Figure 66).



**Figure 34 - Temperature Profile Specimen N88**

Figure 35 shows the temperature profiles associated with an IR image of specimen N810. The target temperature of the is specimen was 1480°C. The temperature profiles of this specimen resemble the profiles of the previous two specimens. As with the previous specimen, the area at the hottest temperature corresponds to an area of a loss of material on the surface of specimen N810 (Figure 67).



**Figure 35 - Temperature Profile Specimen N810**

Figure 36 contains temperature profiles associated with an IR image of specimen N811. The target temperature for this specimen was 1480°C. The higher temperature area in the center of the specimen corresponds to an area of erosion on the surface of the specimen. For this specimen, the area of higher temperature was eventually removed completely (Figure 71).

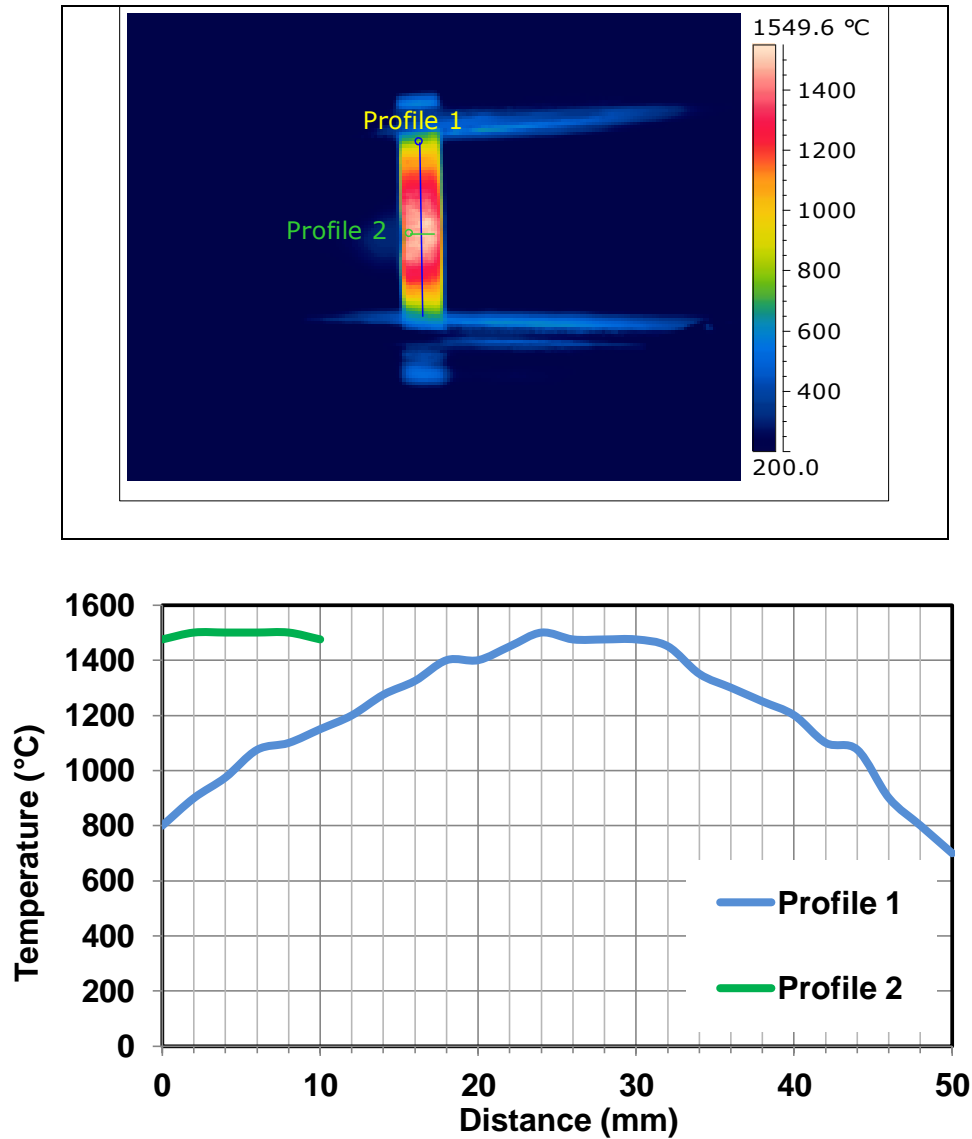
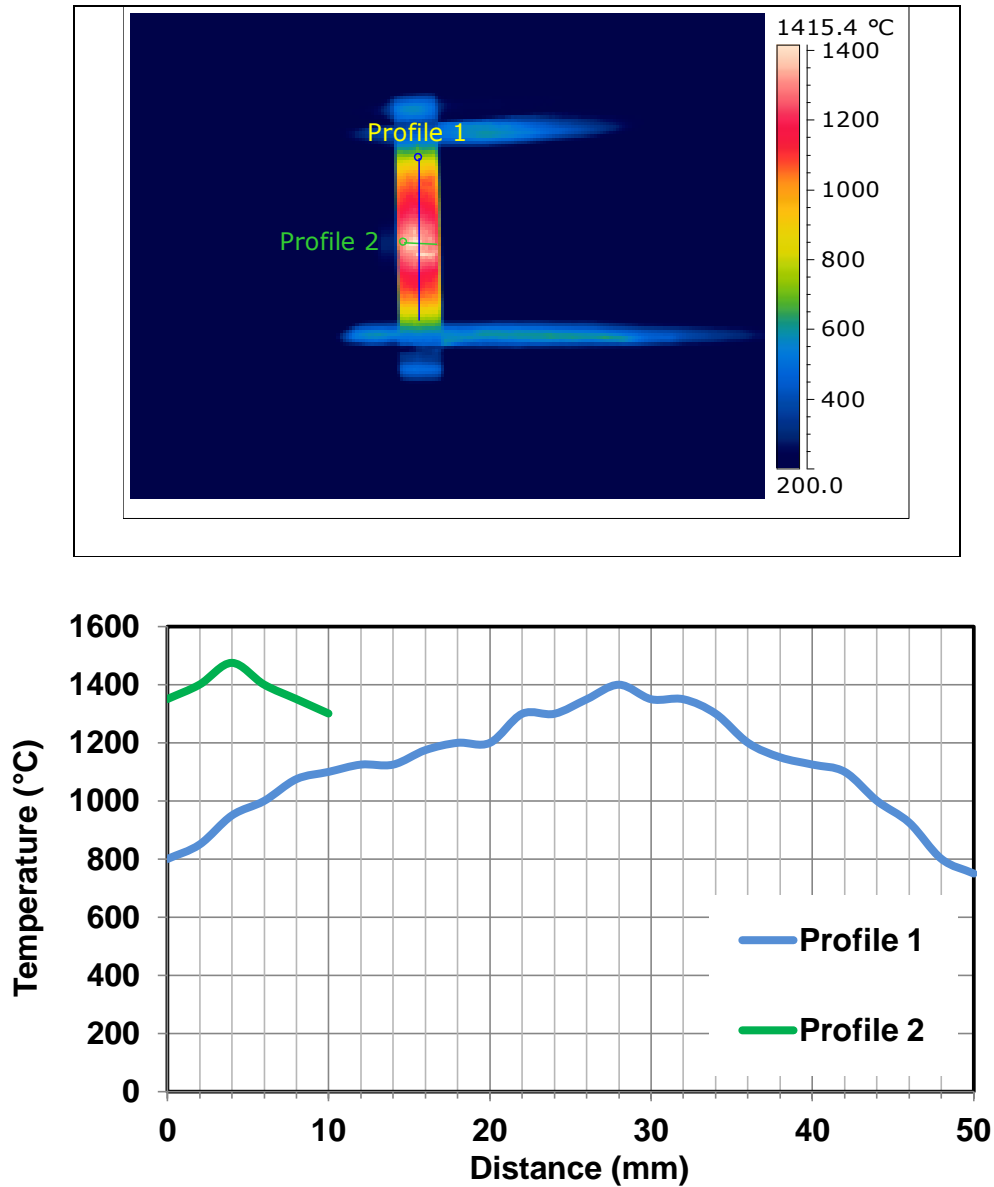


Figure 36 - Temperature Profile Specimen N811

Figure 37 contains the temperature profiles of specimen N812. The target temperature for this specimen was 1350°C. The profile shows a temperature approaching 1500°C near the center of the specimen even though the average temperature in the circle and square areas during the test were near 1350°C. This is a phenomenon that was noticed throughout the test especially with the specimens tested above 1300°C.



**Figure 37 - Temperature Profile Specimen N812**

Figure 38 shows the temperature profiles for specimen N813. The target temperature for this specimen was 1350°C. The profiles for this specimen appear to be similar to the profiles of the previous specimen.

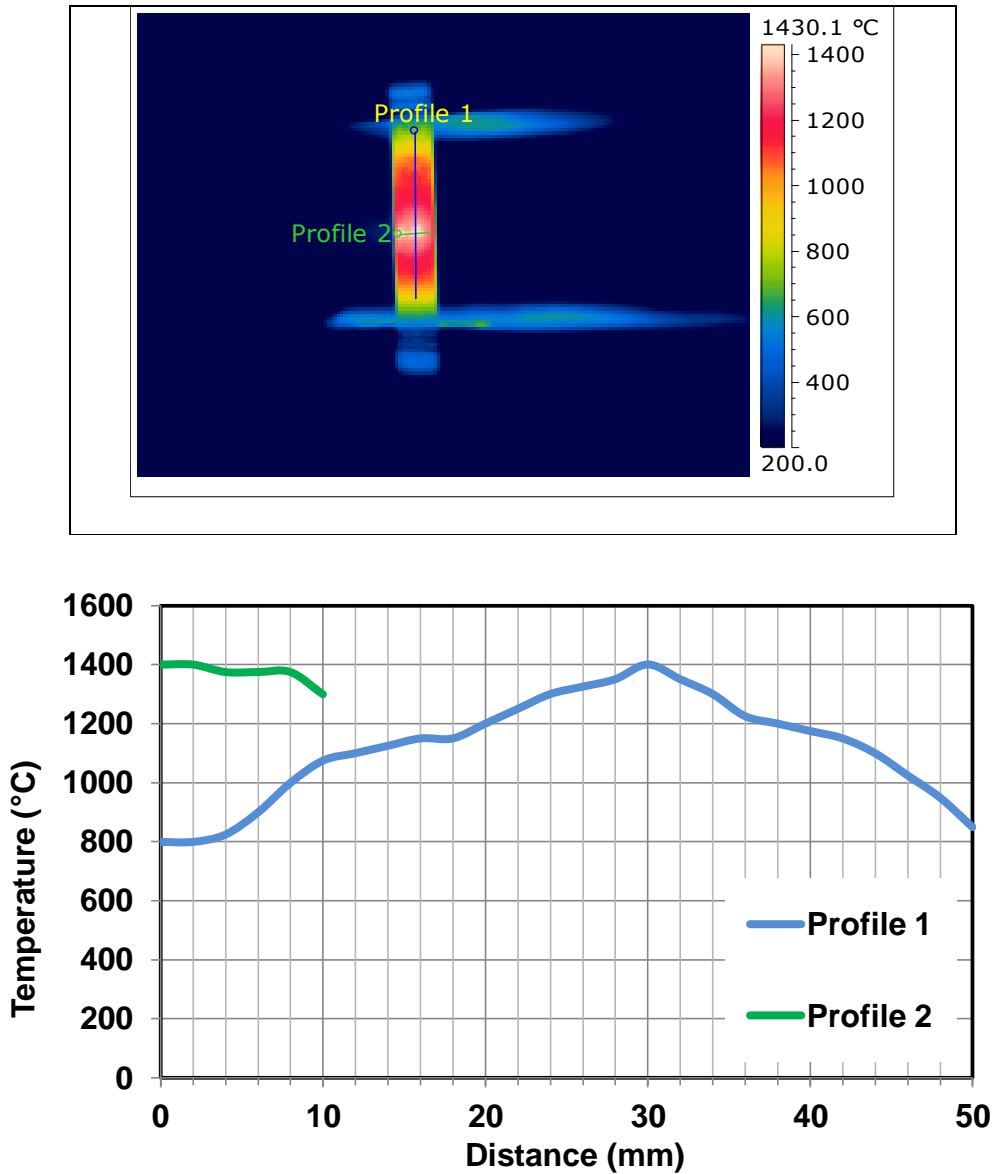
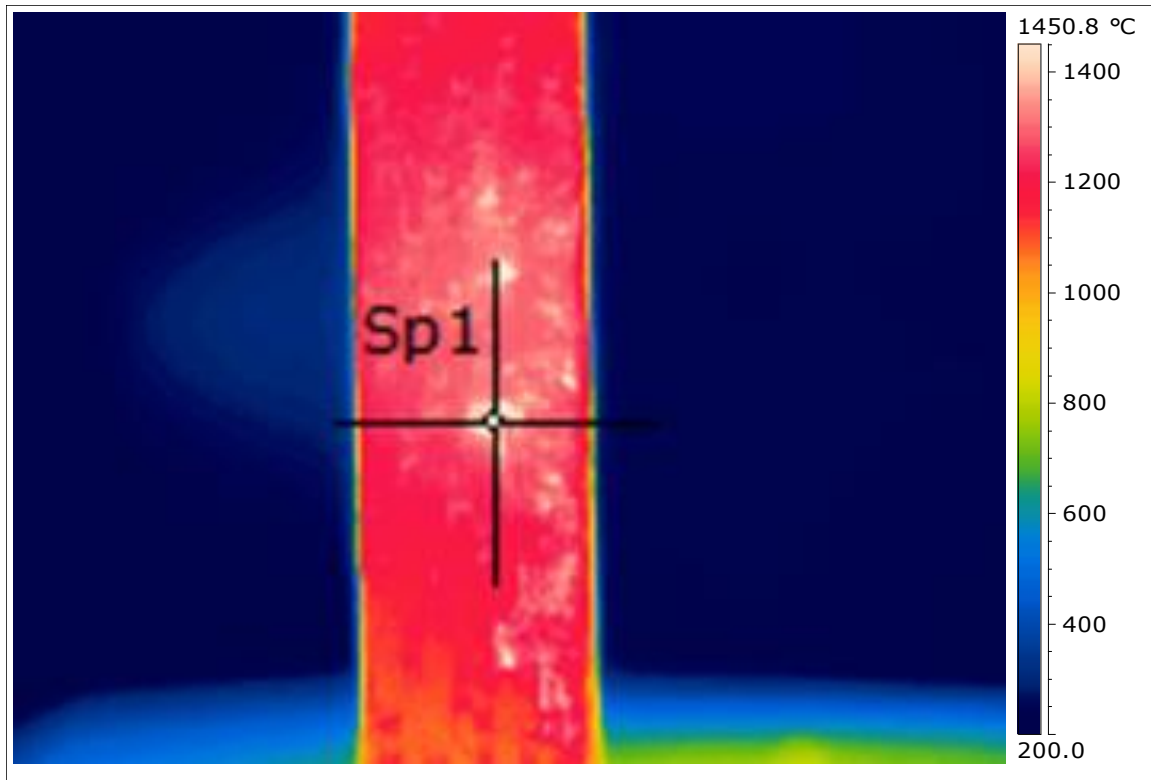


Figure 38 - Temperature Profile Specimen N813

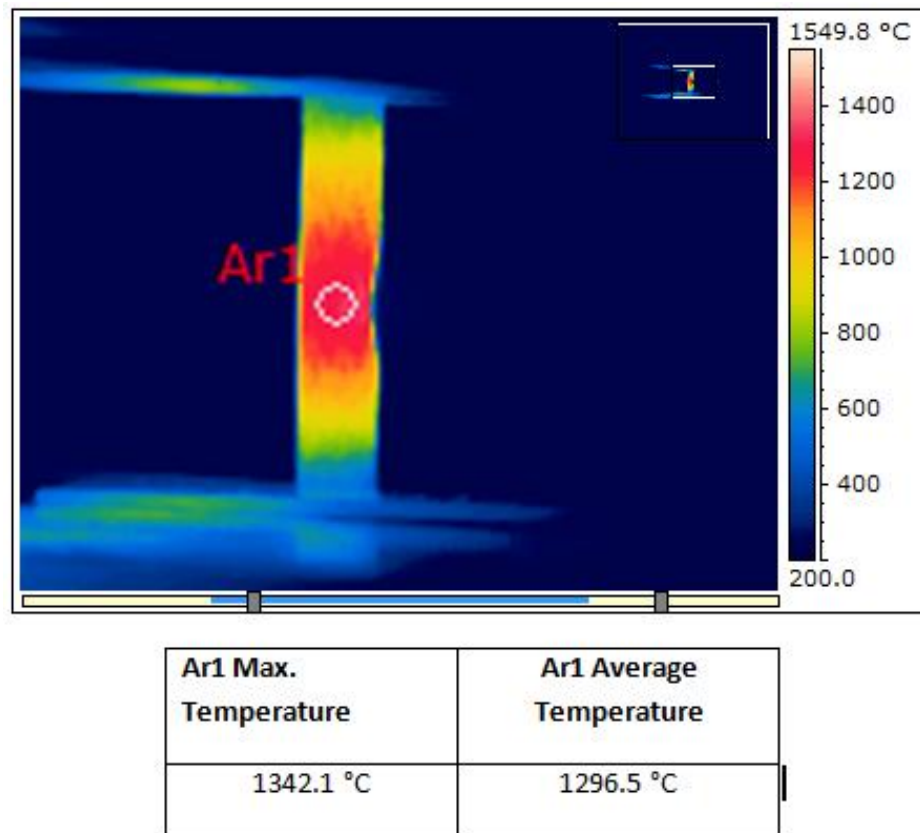


At the start of testing, it was difficult to achieve the higher temperatures which is why some of the actual average temperatures are lower than the target temperatures. Issues with insulation of the grips did limit the ability to achieve the 1480°C target temperature during the first high temperature test. Once the insulation problems were solved, temperatures closer to the target temperatures were achieved. Another issue with keeping a steady temperature was the development of hot spots on some of the specimens. This was especially the case with the specimens tested at the highest temperature. Spots would develop on the specimens where temperatures would be 20°C to 50°C higher than the average temperature inside the circle or square. These areas of higher temperatures will be referred to as hot spots throughout this paper. This was the case with specimen number N83. The data in Table 3 and Table 4 show this. Figure 39 shows one of the hot spots on specimen N83. The hot spots are also why the average temperature in both the square and circle areas are off of the target temperature for specimen N83. It was decided to decrease the overall temperature somewhat since some of the localized temperatures were getting over 50°C higher than the average temperatures in the circle and square. The hot spot issue will be further discussed in chapter 4.5. Some of the differences in the temperatures between the box and circle areas are due to moving the box area to the hotspots in order to monitor them closely. The circle area was always positioned at the center of the specimen.



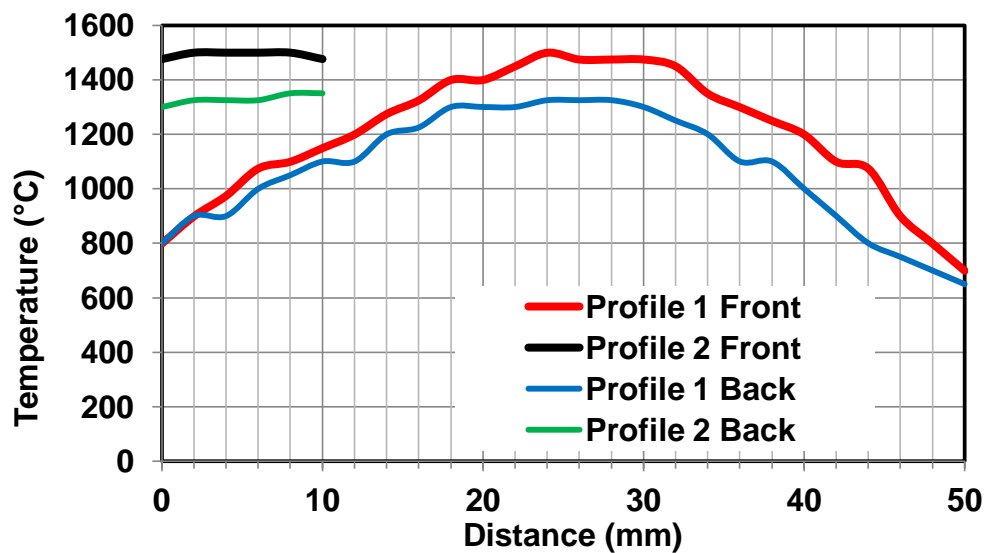
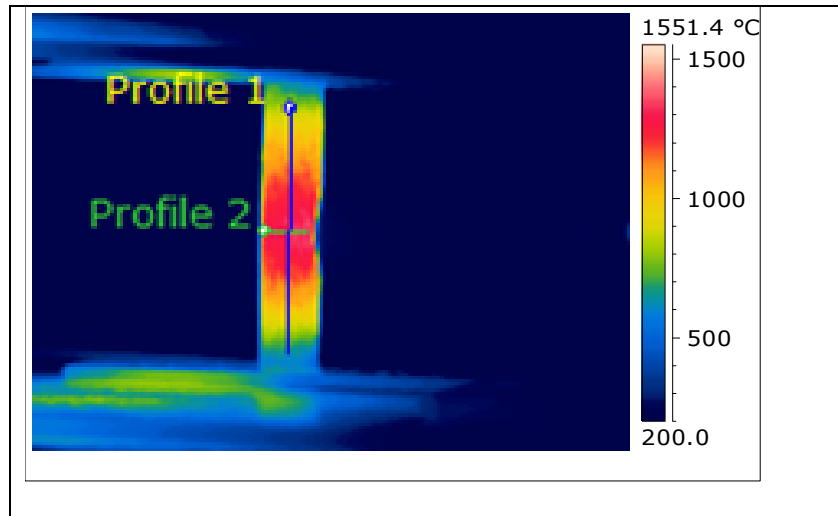
**Figure 39 - Hot Spot on Specimen N83 at 1529°C**

The temperature of the backside of one of the specimens was also observed for a short time to get an idea of what the temperature profile through the specimen looks like. This was done for specimen N811 while the front of the specimen was at a temperature of about 1460°C. Figure 40 shows the thermal image of the backside of specimen N811. The circular area where the temperature was recorded measured about 21 mm<sup>2</sup>. The average temperature in the area was measured at 1297°C.



**Figure 40 - Thermal Image of Specimen N811 Backside**

Figure 41 shows a thermal image of the back of specimen N811 with temperature profiles along the length of the backside of the specimen and across the width of the backside of the specimen as well as the same temperature profiles on the front of the specimen.



**Figure 41 - IR Image of Backside N811 and Front and Back Temperature Profiles**

#### **4.2. Thermal Strain During Testing**

With the specimens being heated to very high temperatures, there was a significant amount of thermal strain exhibited by the material. To characterize how much thermal strain occurred during testing, the cross-head displacement of the MTS was recorded while the specimen was at room temperature while installed in the MTS and

then the displacement was recorded again after the flame was applied to the specimen. From this data, it was possible to calculate a coefficient of thermal expansion ( $\alpha_t$ ) for each specimen. The variation in  $\alpha_t$  could be attributed to the fluctuations in the flame from one test to another. The flame also heats the specimen in a non-isothermal manner. This could lead to a difference in the  $\alpha_t$  calculated during this testing compared to an  $\alpha_t$  found with the material heated isothermally.

**Table 5 - Thermal Strain and Coefficient of Thermal Expansion Calculation**

<b>Specimen</b>	<b>Measurement Temp (°C)</b>	<b>Thermal Strain (%)</b>	<b><math>\alpha_t</math> (<math>10^{-6}/^{\circ}\text{C}</math>)</b>
<i>N82</i>	1250	0.43	3.48
<i>N83</i>	1230	0.45	3.73
<i>N84</i>	1200	0.39	3.33
<i>N85</i>	1215	0.37	3.09
<i>N86</i>	1240	0.41	3.37
<i>N87</i>	1430	0.59	4.23
<i>N88</i>	1451	0.51	3.59
<i>N810</i>	1424	0.48	3.44
<i>N811</i>	1405	0.46	3.32
<i>N812</i>	1328	0.37	2.80
<i>N813</i>	1309	0.36	2.81
		Average	3.38
		St. Dev.	0.41

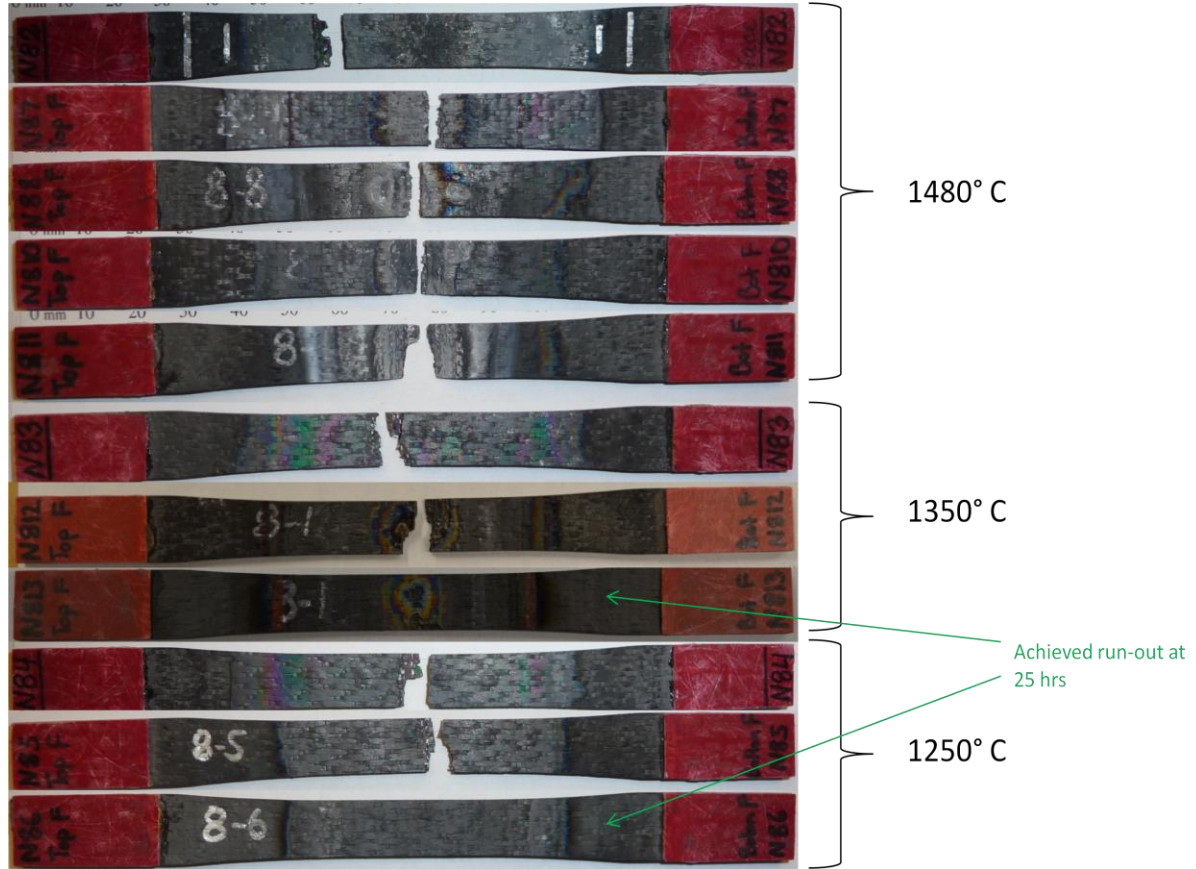
### 4.3. Fatigue Tests

This research consisted of 10 fatigue tests in a combustion environment and one test in the combustion environment with no loading. Fatigue loading consisted of sinusoidal loading at 1 Hz with a stress ratio of 0.1. Fatigue testing lasted until the specimen either failed or reached run-out at 25 hrs. Table 6 contains a summary of the results of all tests.

**Table 6 - Fatigue Tests Results Summary**

<b>Spec. ID</b>	<b>Temp. (°C)</b>	<b>Stress (MPa)</b>	<b>% of UTS</b>	<b># of Cycles to Failure</b>	<b>Location of Failure</b>	<b>Room Temp. (°C)</b>	<b>Room Hum. (%)</b>
<i>N82</i>	1408	210	55	2144	15 mm from center	24	49
<i>N83</i>	1273	210	55	4587	5 mm from center	25	56
<i>N84</i>	1237	210	55	9464	0 mm from center	22	47
<i>N85</i>	1238	175	46	19769	6 mm from center	22	38
<i>N86</i>	1237	125	33	90058	run-out	24	45
<i>N87</i>	1419	175	46	7200	6 mm from center	23	35
<i>N88</i>	1440	125	33	12574	0 mm from center	22	52
<i>N810</i>	1455	80	21	15462	1 mm from center	21	40
<i>N811</i>	1446	0	0	60010	0 mm from center	25	30
<i>N812</i>	1345	125	33	67920	2 mm from center	24	25
<i>N813</i>	1345	90	24	90070	run-out	25	25

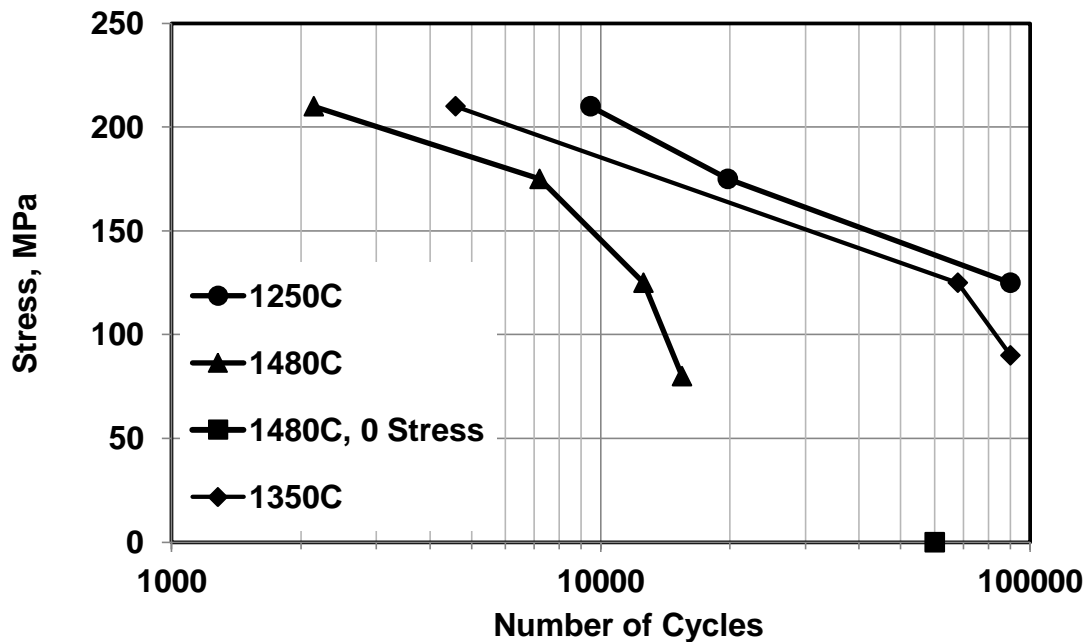
Most of the specimens failed near the center of the specimen. The first specimen tested at 1480°C and a max stress of 210 MPa did fail 15 mm away from the center; however, this area of the specimen did see temperatures above 1300°C. Figure 42 shows all specimens after testing. Two of the specimens achieved run-out and the rest failed during fatigue testing.



**Figure 42 - All Specimens After Tests**

The data collected during testing allowed for the development of a stress vs. cycles curve (S-N curve). Figure 43 shows the S-N curve developed during this research. The S-N curve shows that there is a significant loss of fatigue strength in temperatures above 1400°C. There is also a temperature dependence on fatigue life for temperatures under 1400°C. Specimens tested at the same max stress showed a decrease in fatigue life with increasing temperature. This is evident in Figure 43. At a max stress of 210 MPa,

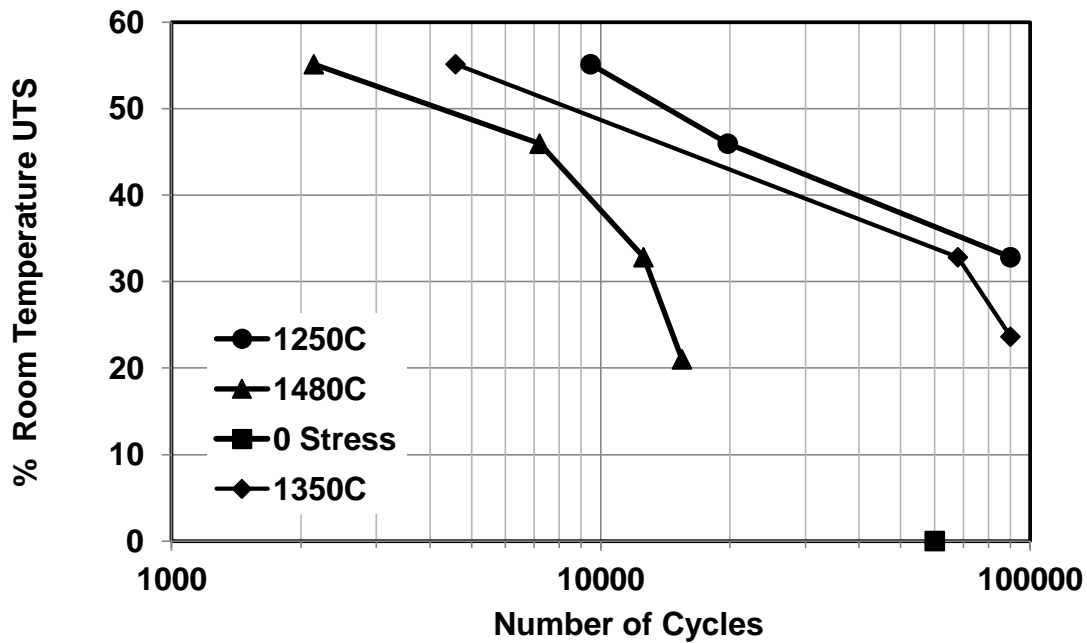
the specimen tested at 1350°C saw a fatigue life that was 52% less than the specimen tested at 1250°C and the specimen tested at 1480°C saw a fatigue life that was 77% lower than the fatigue life of the specimen tested at 1250°C. For a max stress of 175 MPa, the specimen tested at 1480 saw a fatigue life that was 64% lower than the specimen tested at 1250°C. At a max stress of 125 MPa, the specimen tested at 1350°C saw a fatigue life that was 25% lower than the specimen tested at 1250°C, and the specimen tested at 1480°C saw a fatigue life that was 86% lower than the fatigue life of the specimen tested at 1250°C.



**Figure 43 - S-N Curve Developed From Experimental Data**

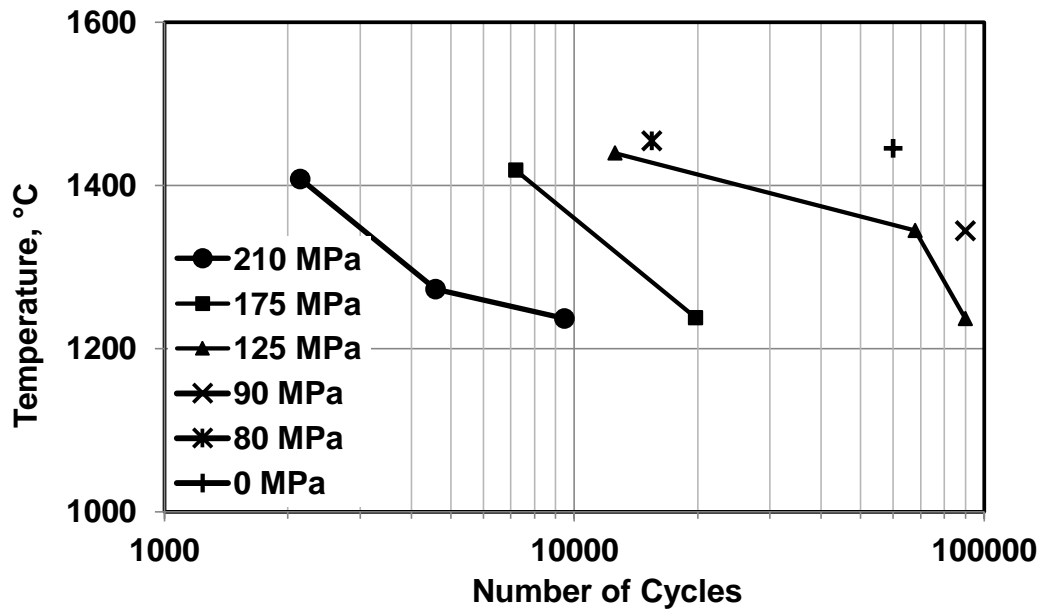


Figure 44 shows the S-N curve normalized to the room temperature UTS of 381 MPa that was obtained from experiments performed by Rolls Royce.



**Figure 44 - S-N Curve Normalized to The Room Temperature UTS Provided by Rolls Royce**

Figure 45 contains the temperature vs. number of cycles plot for all specimens tested. This figure again shows the loss of fatigue strength due to increasing temperature provided by the combustion environment.



**Figure 45 - Temperature vs. Number of Cycles for All Specimens**

Figure 46 through Figure 56 show the maximum extension of each specimen tested. The specimen extension was measured as the difference in MTS cross-head displacement over time and the cross-head displacement measured at the beginning of the test with the specimen at temperature before applying the fatigue loading. The specimen extension data in the following figures represents the extension when the maximum stress was applied during the cyclic fatigue loading. This measurement includes changes in the length of the specimens due to changes in temperature along the length of the specimen. The changes in the length of the specimen due to thermal expansion is why there are some fluctuations in the data. During testing, especially at the highest temperatures, there were some fluctuations in the MTS grip temperature due to changes or improvement in the grip insulation and cooling scheme as testing progressed. Figure 46 through Figure 49 contain specimen extension vs. number of cycles for the specimens tested at 1480°C.

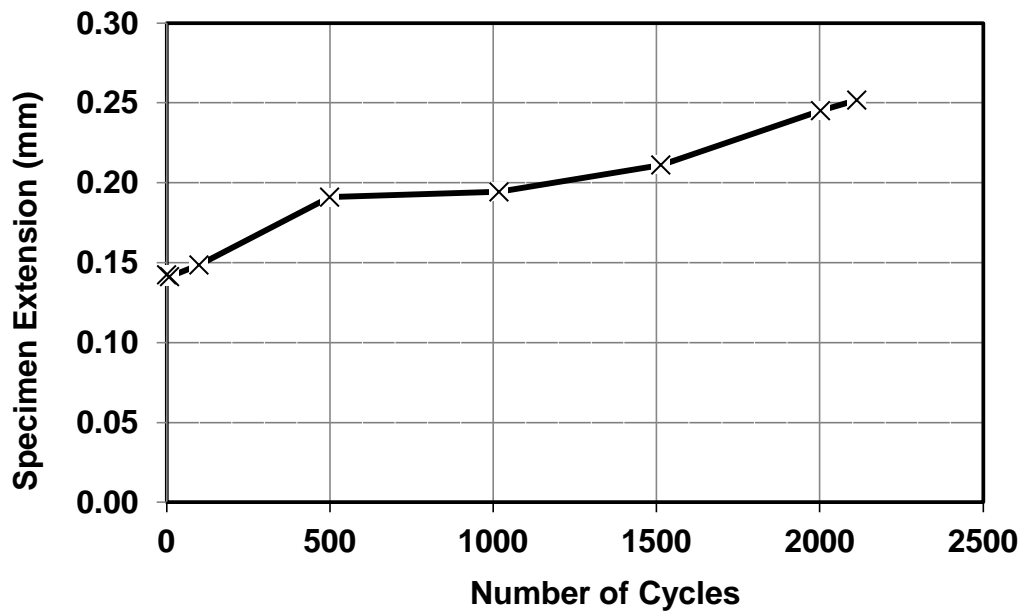


Figure 46 - 210 MPa 1480°C (#N82) Specimen Extension vs Number of Cycles

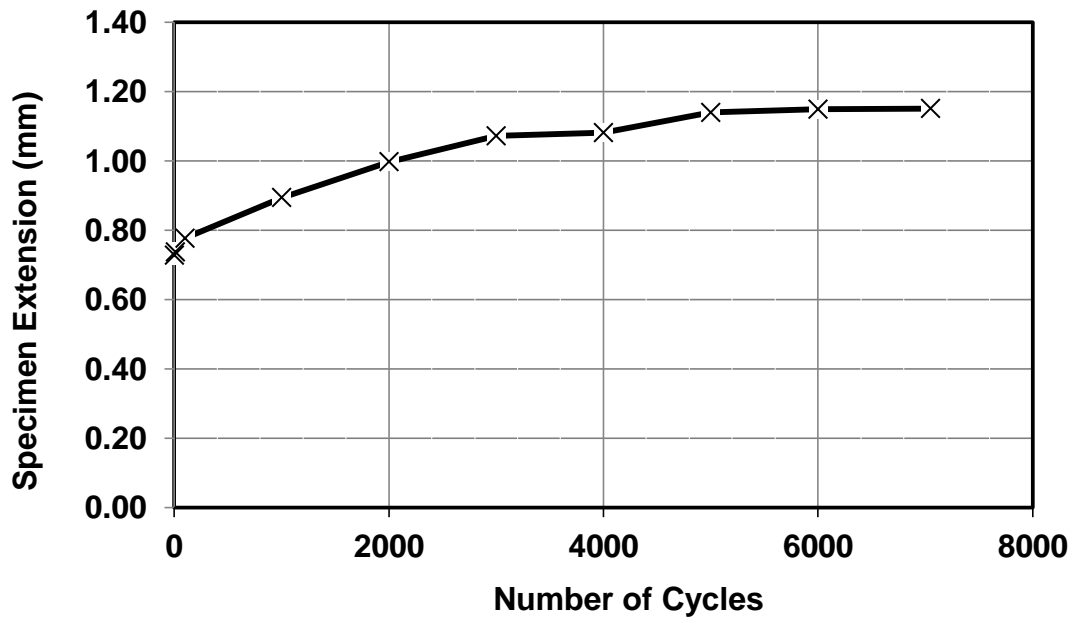
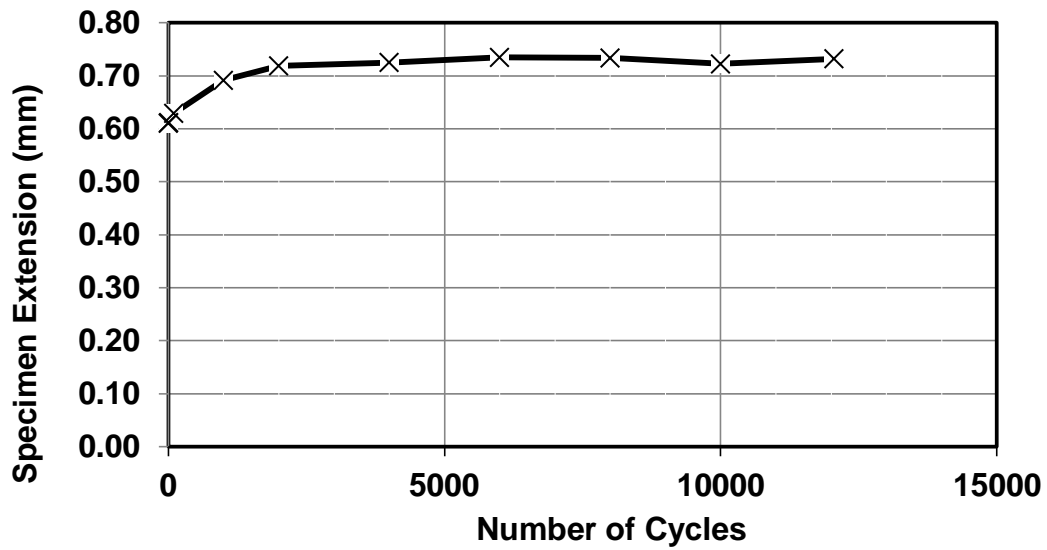
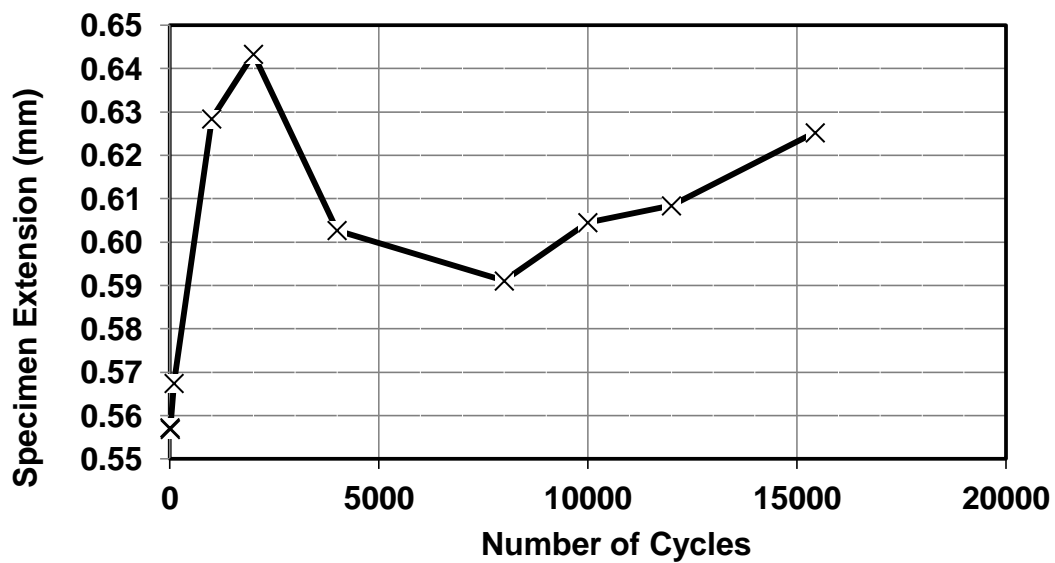


Figure 47 - 175 MPa 1480°C (#N87) Specimen Extension vs. Number of Cycles



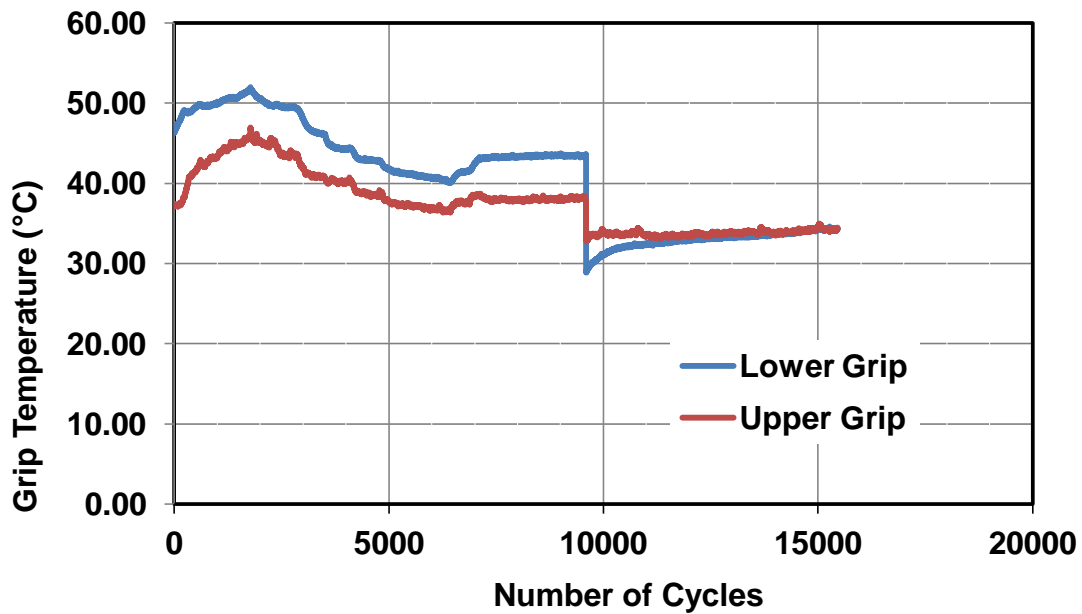
**Figure 48 - 125 MPa 1480°C (#N88) Specimen Extension vs. Number of Cycles**

The specimen tested at 80 MPa max stress and a temperature of 1480°C (#N810) saw a spike in grip temperature at around 2000 cycles. This corresponds with the spike in specimen extension that is present in Figure 49.



**Figure 49 - 80 MPa 1480°C (#N810) Specimen Extension vs. Number of Cycles**

Figure 50 shows the grip temperature vs. number of cycles for specimen N810. The spike in grip temperature near the 2000 cycle mark corresponds to the increase in specimen extension present in Figure 49. This increase in specimen extension can be attributed to thermal expansion of the material. This increase in grip temperature was due to an issue with the insulation or the grip cooling scheme.



**Figure 50 - Grip Temperature vs. Number of Cycles for Specimen N810**

Figure 51 through Figure 53 show the specimen extension vs. number of cycles for the specimens tested at 1350°C.

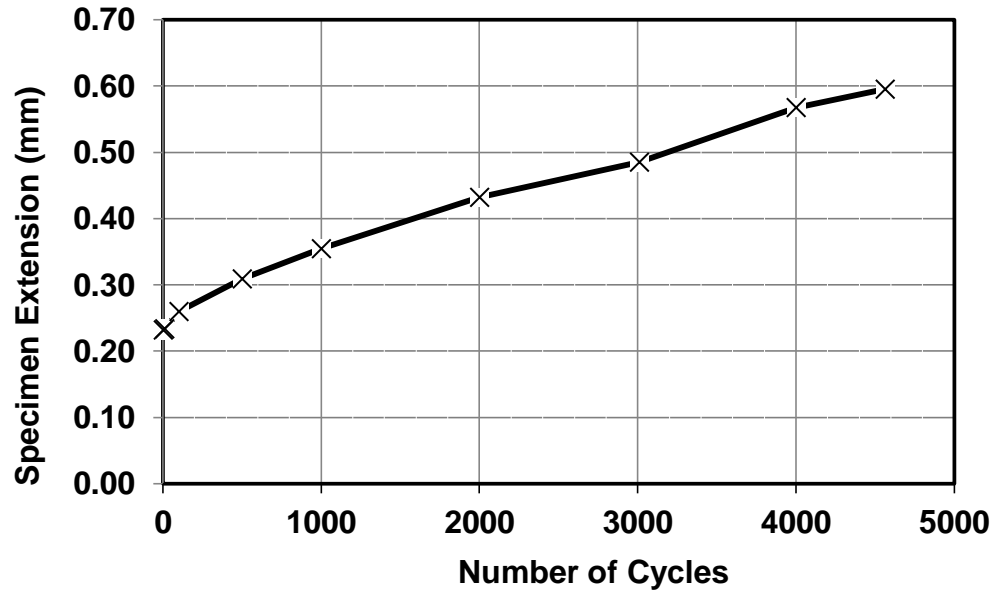


Figure 51 - 210 MPa 1350°C (#N83) Specimen Extension vs. Number of Cycles

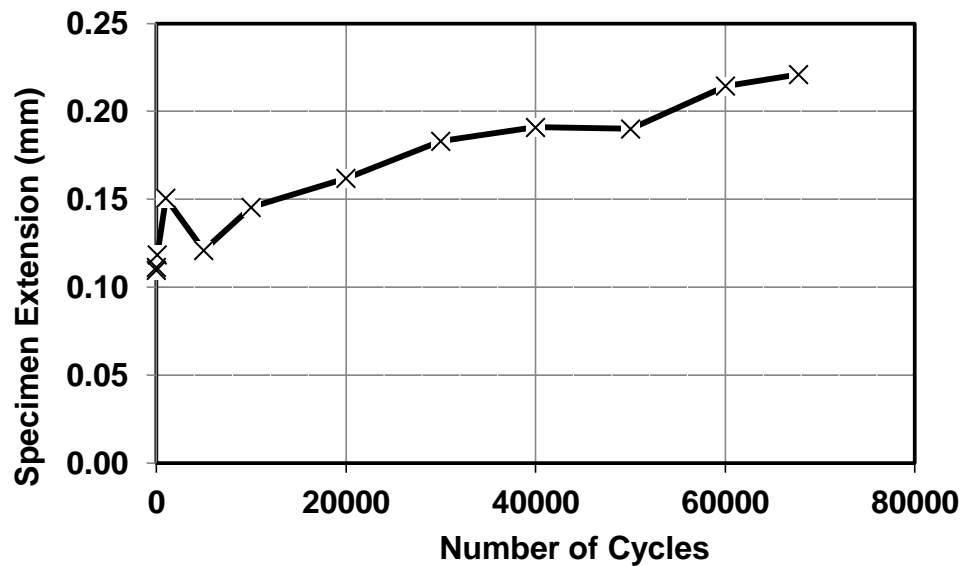
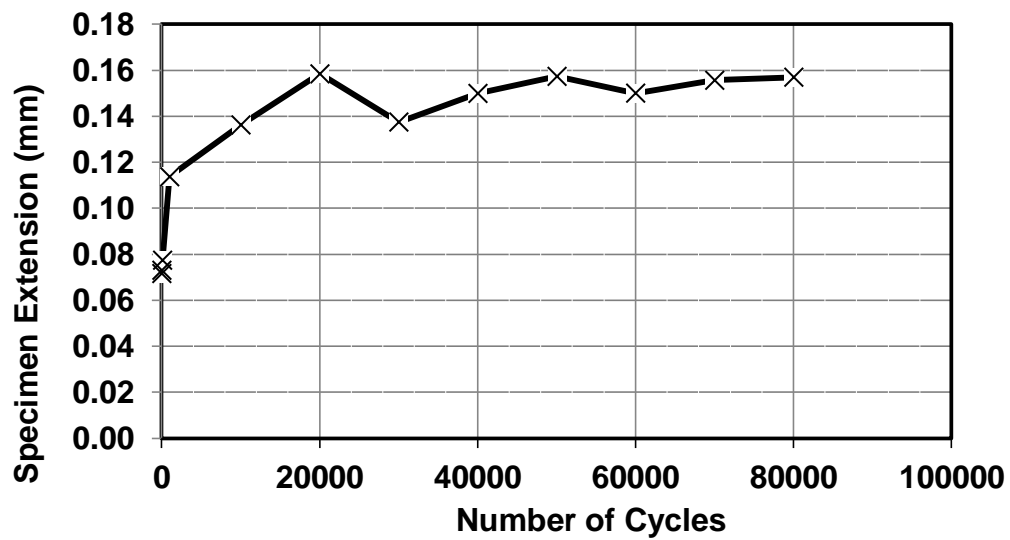
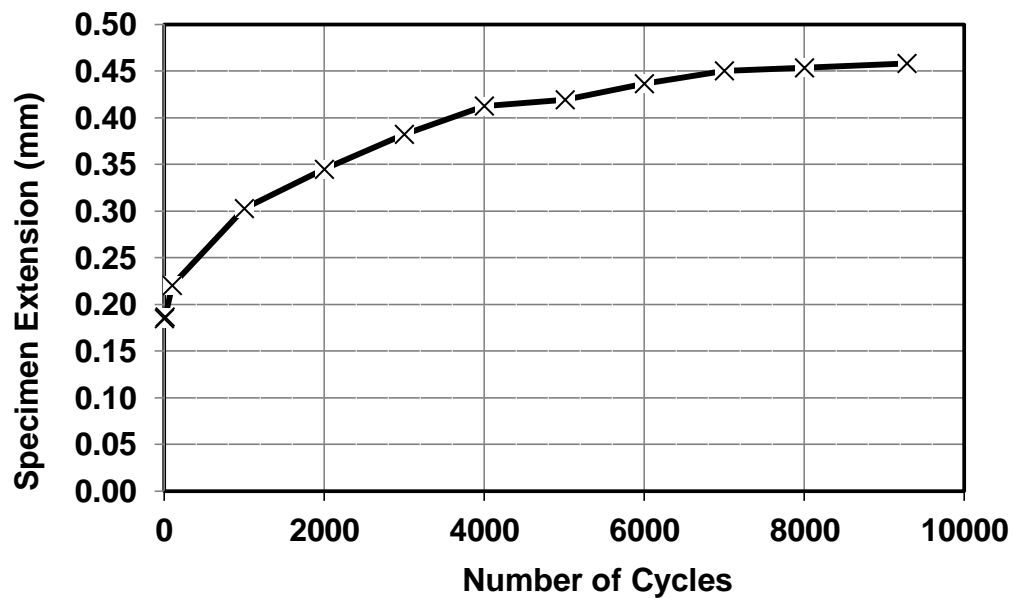


Figure 52 - 125 MPa 1350°C (#N12) Specimen Extension vs. Number of Cycles



**Figure 53 - 90 MPa 1350°C (#N813) Specimen Extension vs. Number of Cycles**

Figure 54 through Figure 56 are the specimen extension vs. number of cycle plots for the specimens tested at 1250°C.



**Figure 54 - 210 MPa 1250°C (#N84) Specimen Extension vs. Number of Cycles**

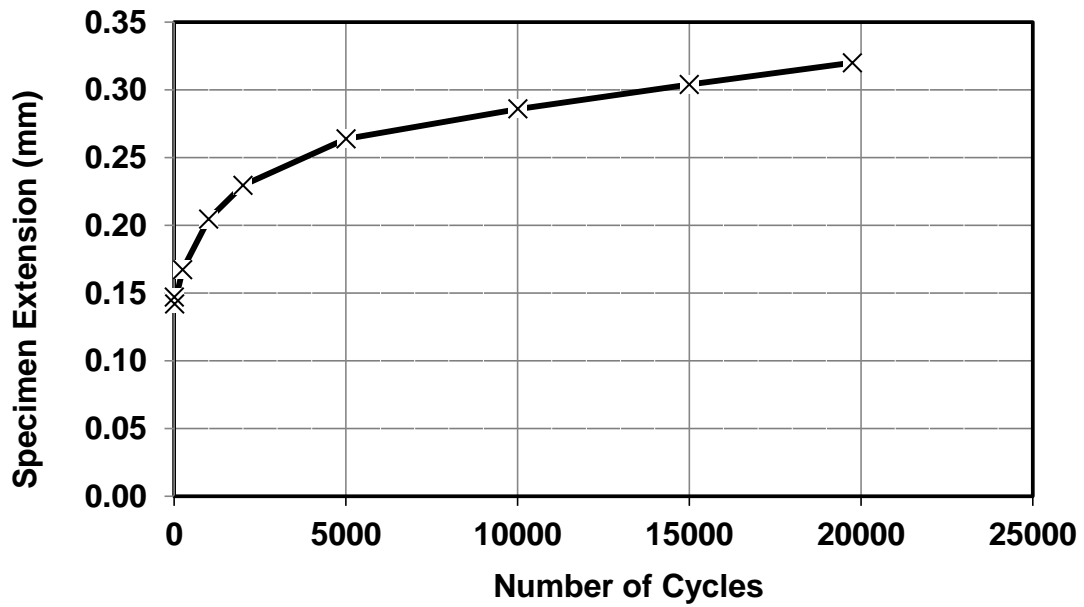


Figure 55 - 175 MPa 1250°C (#N85) Specimen Extension vs. Number of Cycles

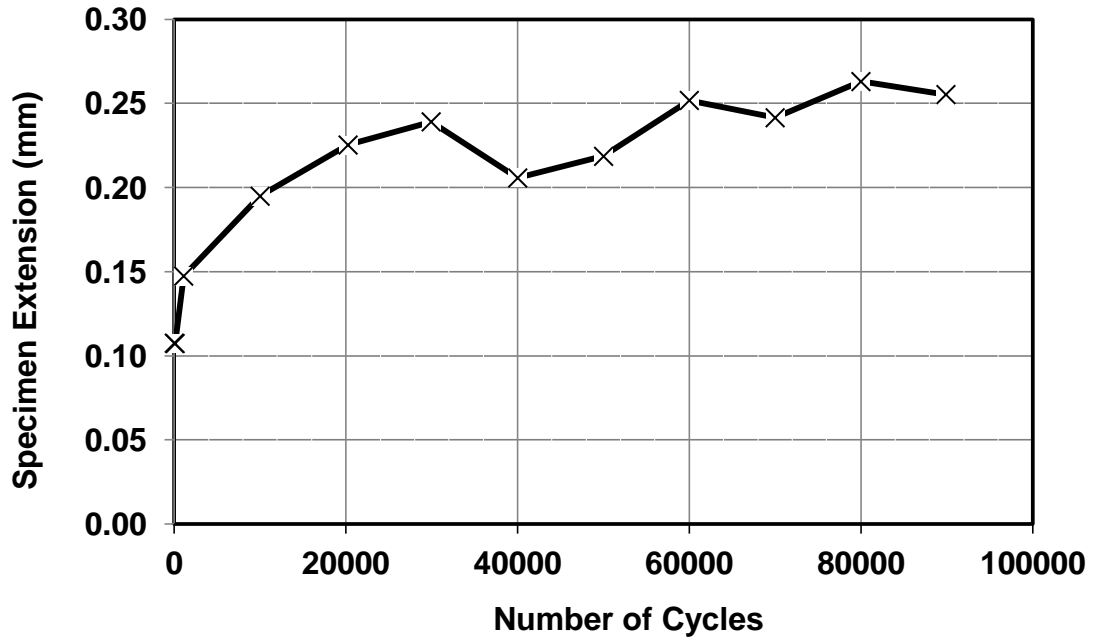


Figure 56 - 125 MPa 1250°C (#N86) Specimen Extension vs. Number of Cycles



#### 4.4. Residual Strength Tests

To get an idea of the retained strength of the specimens that survived through the run-out condition, tensile tests of the two specimens were performed. Specimen N86 was tested at 1250°C with a max stress of 125 MPa applied during fatigue loading for 25 hours. The max stress before failure for specimen N86 residual strength test was 126 MPa which is 33% of the UTS at room temperature. A modulus of elasticity, E, was calculated from the stress-strain data to be 88 GPa. The modulus of elasticity from the residual strength test was 38% of the modulus of elasticity at room temperature. Figure 57 shows the stress-strain data collected during the residual strength test of specimen N86.

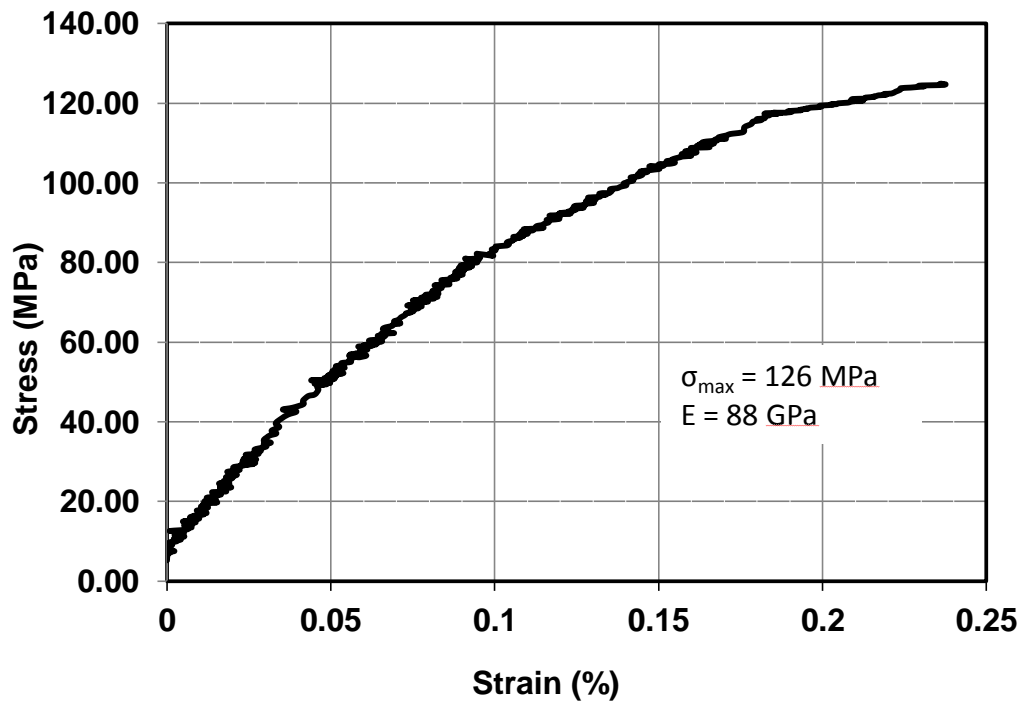
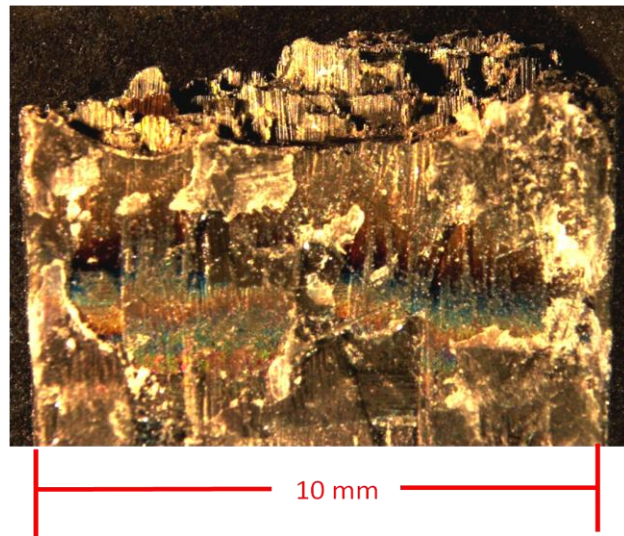


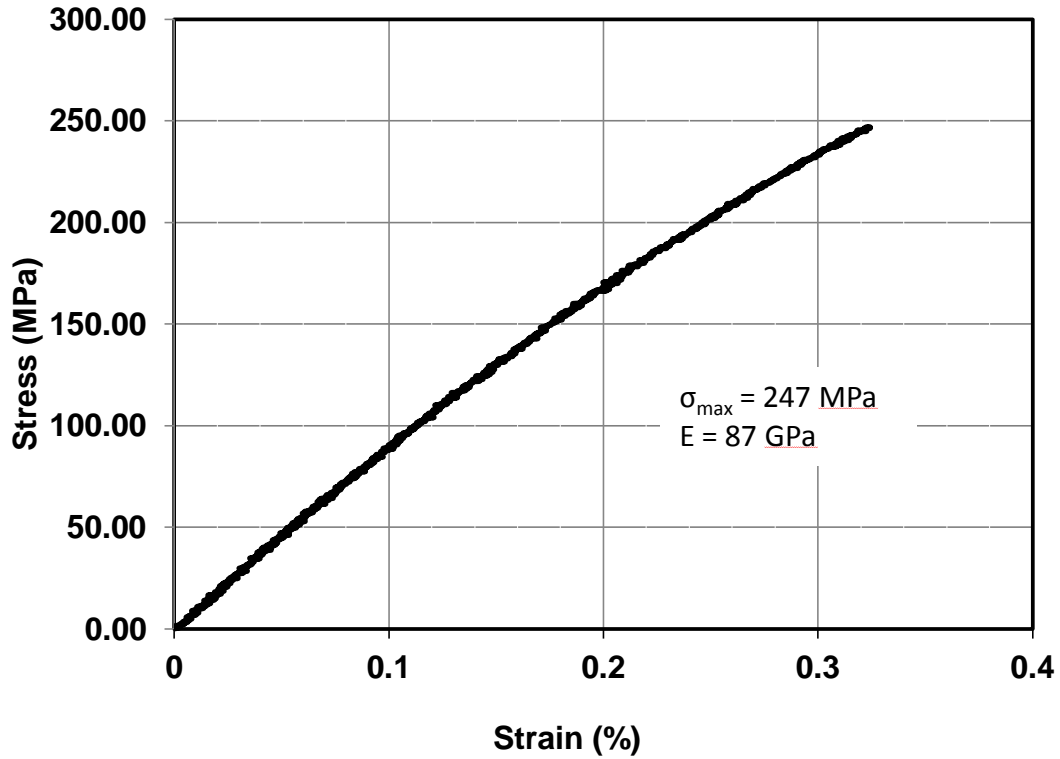
Figure 57 - Specimen N86 Residual Strength Test Stress vs. Strain

Figure 58 is an optical microscope image of the area of the fracture that occurred during the residual strength test of specimen N86.



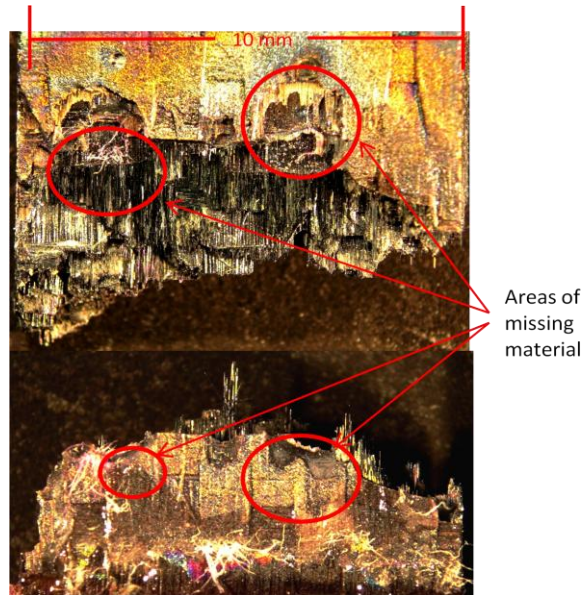
**Figure 58 - Fracture Surface of Specimen N86 After Residual Strength Test**

Specimen N813 was tested at a temperature of 1350°C with a max stress of 90 MPa applied during fatigue loading for 25 hours. The stress-strain curve for the residual strength test of specimen N813 is shown in Figure 59. The max stress before failure for the residual strength test of specimen N813 was 247 MPa which is 65% of the room temperature UTS. The calculated modulus of elasticity was 87 GPa which is 38% of the room temperature modulus.



**Figure 59 - Specimen N813 Residual Strength Test Stress vs. Strain**

The failure of specimen N813 during the residual strength test occurred in the heated area. The fracture appears to pass through areas of missing material that occurred during the original fatigue test as pointed out in Figure 60. These areas of missing material can be seen in Figure 68 also.



**Figure 60 - Fracture Surface of Specimen N813 After Residual Strength Test**

#### **4.5. Material Loss - Oxidation and Erosion**

During testing at the highest temperature (almost 1480°C), there was an obvious loss of material that occurred on the specimens that survived more than a couple of hours. This phenomenon was mostly observed with specimens tested at temperatures above 1400°C, but two specimens tested near 1350°C also started to show signs of material loss after exposure to the combustion environment of a significant amount of time. Each specimen was weighed before and after testing. This data was recorded to get an idea of how much material is lost during testing. Figure 61 shows the weight loss in grams versus amount of time each specimen was exposed to the combustion environment, and Figure 62 shows the weight loss normalized to the original weights of each specimen. The specimens tested near 1480°C show significant weight loss with increasing exposure to the combustion environment. The specimens tested at or below 1350°C did not exhibit this behavior.

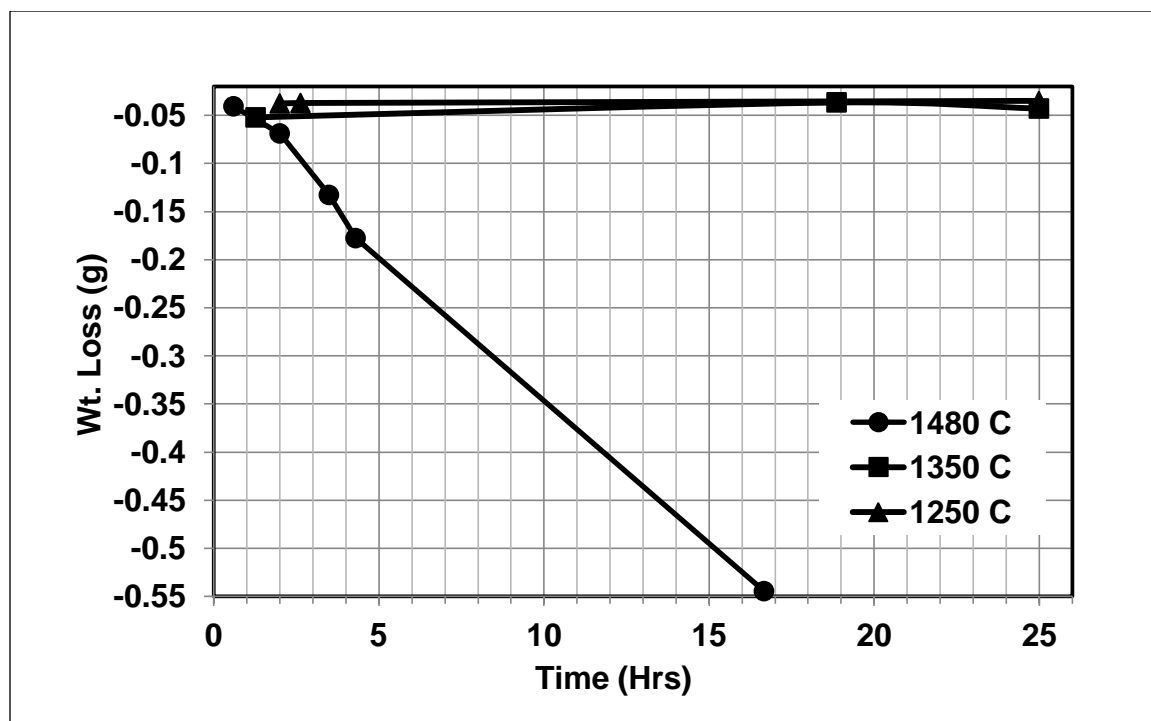


Figure 61 - Weight Loss vs. Time for All Specimens

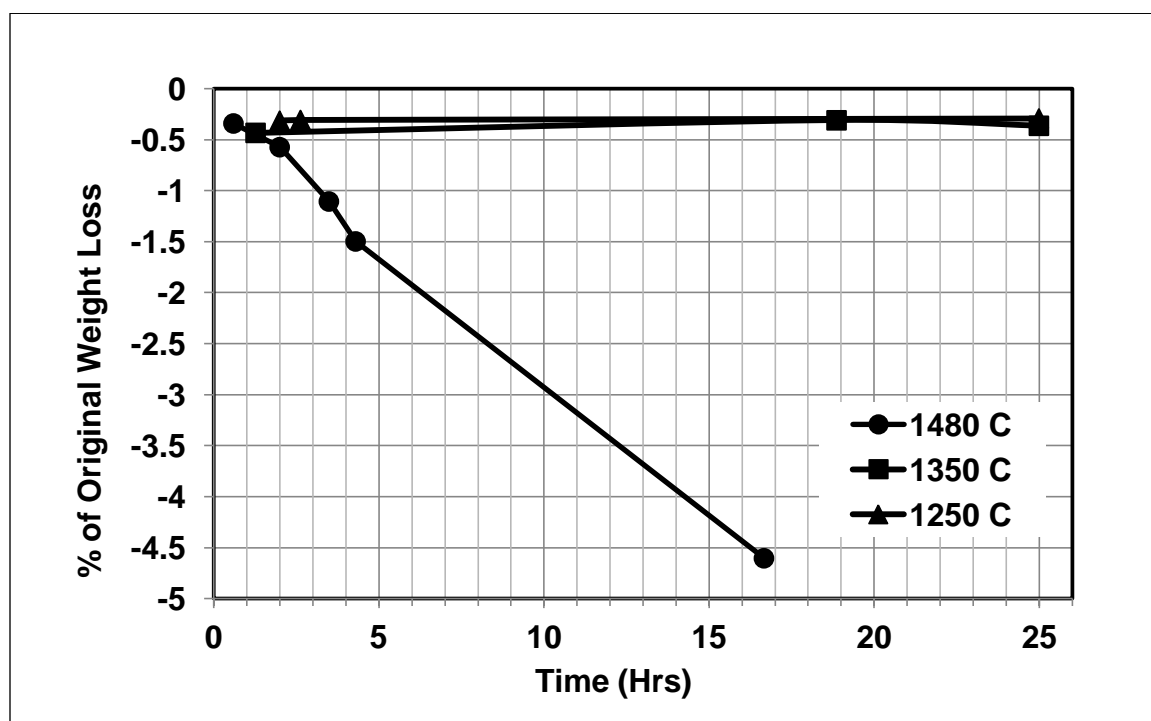
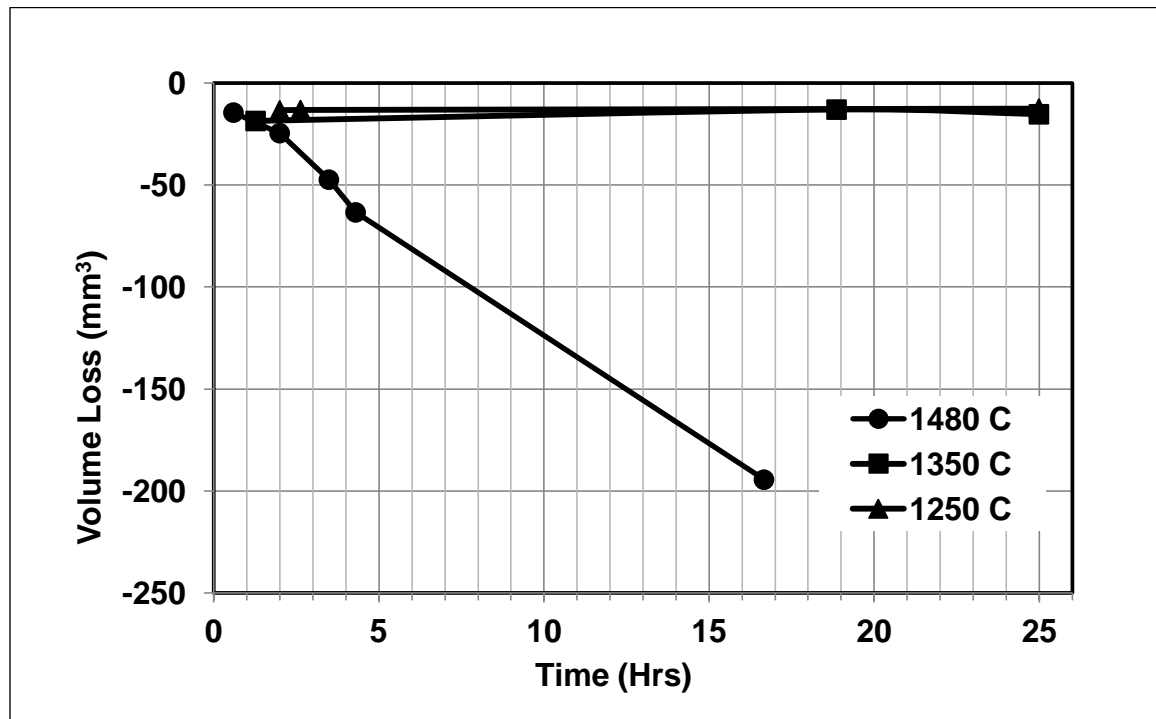


Figure 62 - Weight Loss Data Normalized to Original Weights

The density of the material is reported to be  $2.8 \text{ g/cm}^3$  from the manufacturer [27]. Using this, it was possible to come up with an estimate of the volume of material lost during testing. Figure 63 contains the volume lost over time for each specimen. An interesting amount of volume was lost on the specimens tested at temperatures near  $1480^\circ\text{C}$ .



**Figure 63 - Volume Loss vs. Time for All Specimens**

The loss of material during testing was evident upon visual inspection of the specimens that suffered material loss. Some of the specimens that did not readily show signs of material loss during a visual inspection did show some signs of material loss when viewed under the optical microscope. Most of the specimens that showed signs of

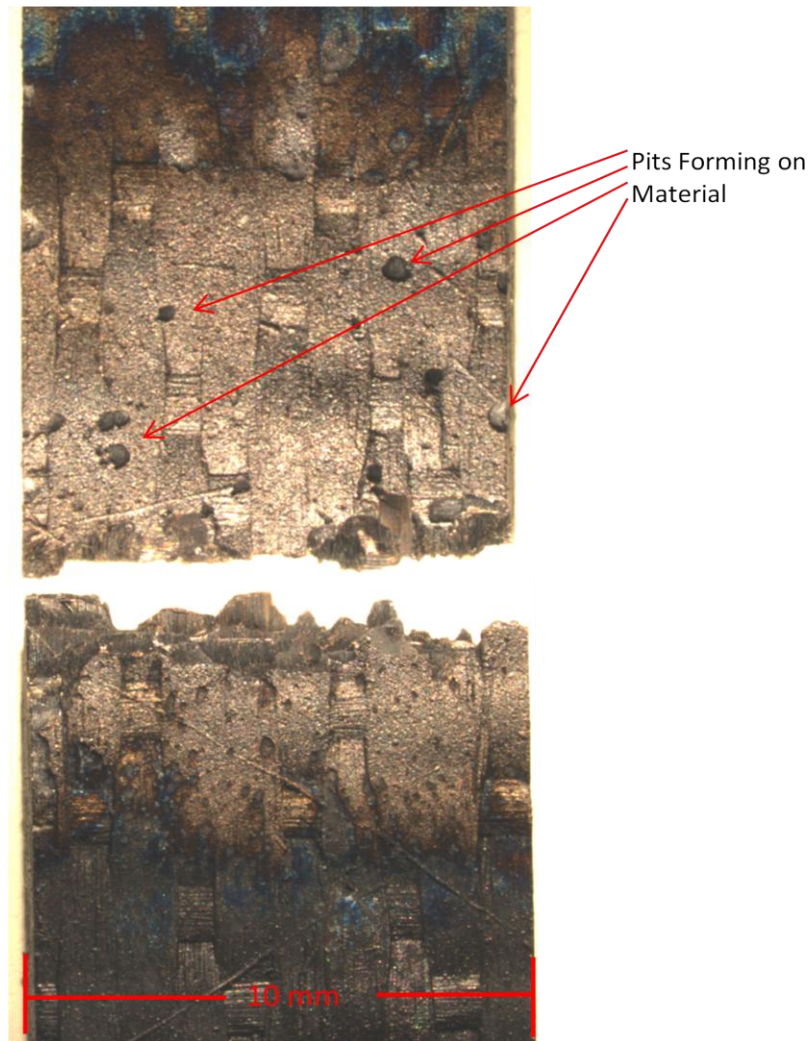
material loss were subjected to temperatures of over 1400°C. Figure 65, Figure 66, and Figure 67 show the material loss that occurred on specimens N87, N88, and N810 respectively. There was only one specimen that showed some material loss at the lower temperatures. Specimen N813 was subjected to 25 hrs of temperatures around 1350°C and after the test was over it did show signs of material loss taking place. This is evident in Figure 68.

Figure 64 shows the area of fracture for specimen N82. This image is of the side facing the flame. This specimen did not show any noticeable signs of material loss as evident in the following figures.



**Figure 64 - Flame Side of Specimen N82 After Fatigue Test With no Material Loss**

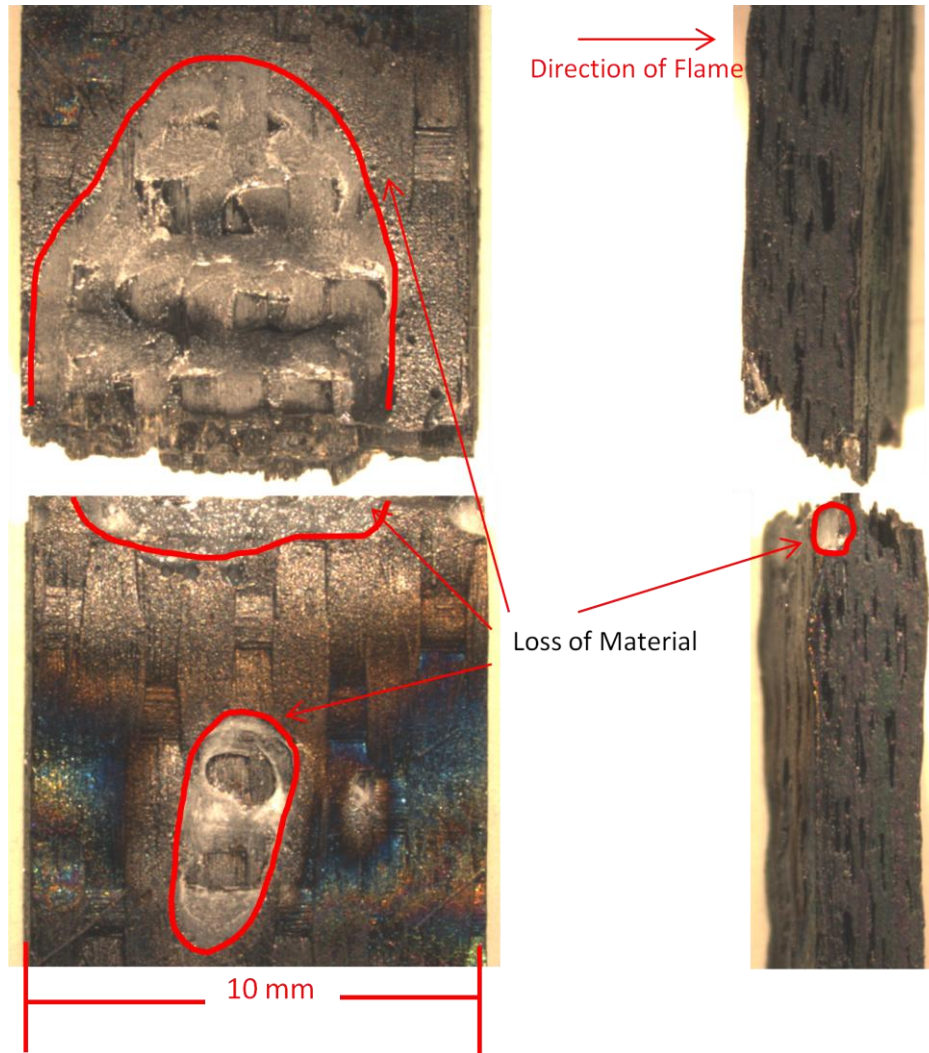
Figure 65 shows the beginning of material loss taking place on specimen number N87. This specimen survived two hours of combustion conditions with a surface temperature close to 1480°C. Pits are starting to form in the area where the flame was impinging on the specimen.



**Figure 65 - Specimen N87 Shows Signs of Erosion After 2 hrs**

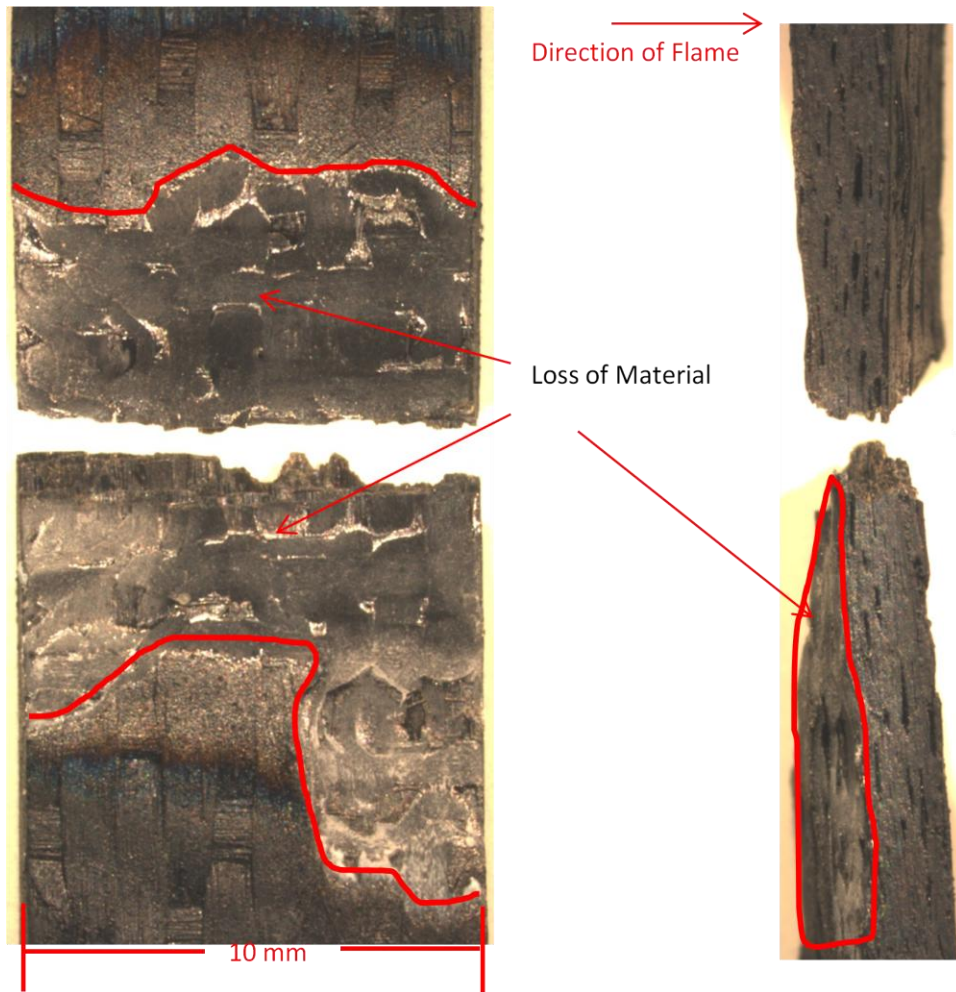


Figure 66 shows the material loss that occurred after 3.5 hrs of exposure to the combustion environment at a temperature near 1480°C. There is a cavity of material loss that developed where the flame was impinging on the specimen. The specimen fractured near where the majority of the erosion has taken place. There were also some pits that formed a little lower on the specimen as well.



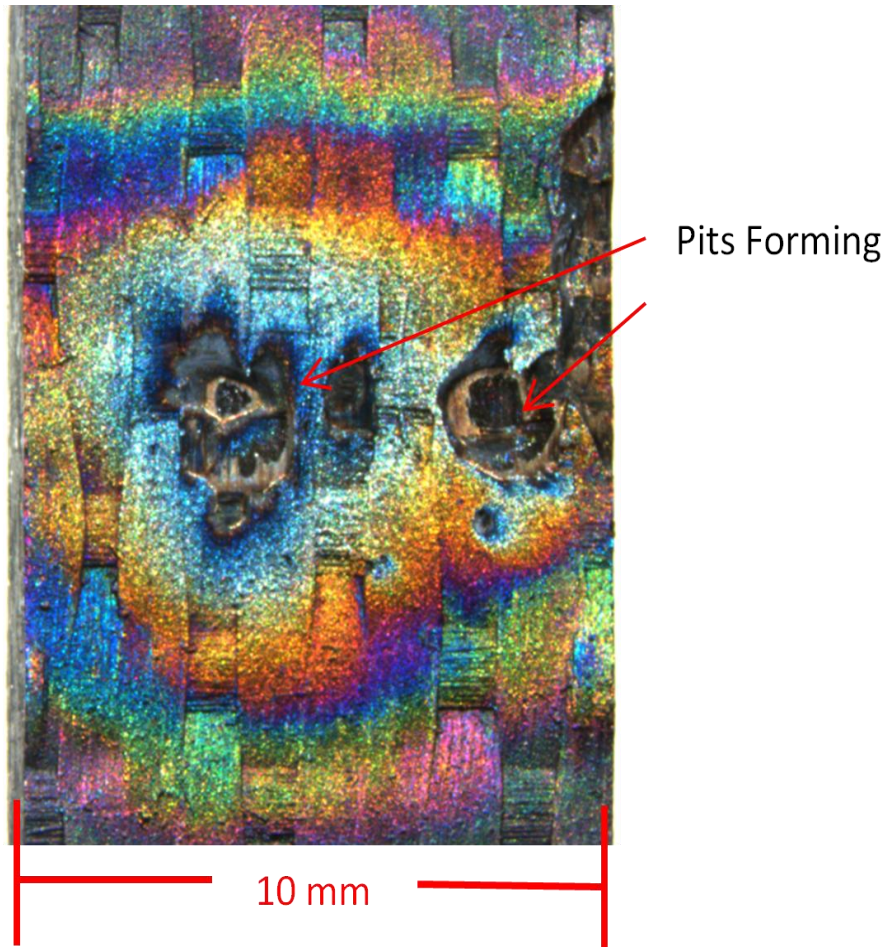
**Figure 66 - Specimen N88 With Obvious Material Loss After 3.5 hrs**

Figure 67 is an image of specimen N810 showing significant material loss after 4.3 hours of exposure to the combustion environment at temperatures near 1480°C. Most of the area central to where the flame was impinging on the specimen has been removed. The specimen fractured at about the center of this area where material was removed.



**Figure 67 - Specimen N810 With Obvious Material Loss After 4.3 Hrs**

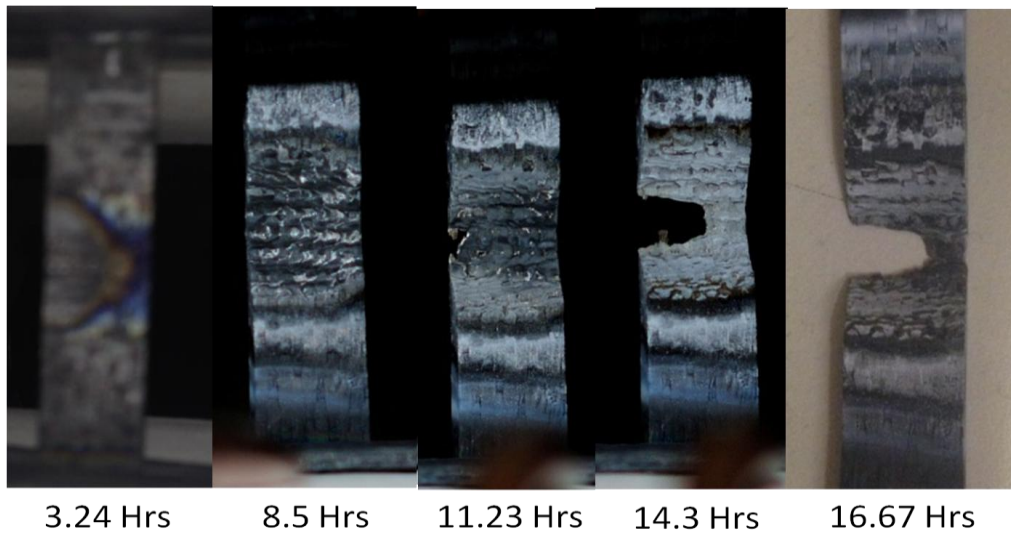
Figure 68 is an image of the only one of the specimens tested at temperatures at or under 1350°C that showed any signs of material loss. Specimen N813 survived 25 hours in the combustion environment at temperatures near 1350°C. At the conclusion of the test, there were noticeable pits in the front surface of the specimen in the area of impingement of the flame.



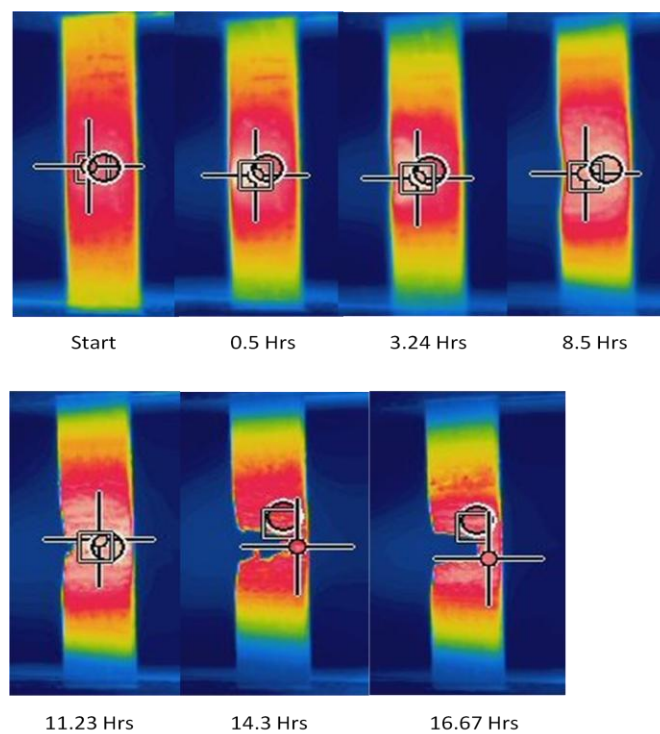
**Figure 68 - Pits Starting to Form on Specimen N813**

After it was realized that there was a significant amount of material being lost while the specimens were tested in the combustion environment, it was decided to run a test with no fatigue loading at the highest temperature. Specimen N811 was installed into the MTS, and the force control was set to zero to ensure no load would be placed on the specimen as it expanded due to heating. Figure 69 shows the progress of the material loss at different periods of time during the test. This phenomenon can also be observed in the thermal images taken during testing as in Figure 70. A hot spot developed at around the 30 minute mark. This is where the material loss started and eventually progressed through the width of the specimen until the force of the flame was enough to cause the remaining material to fracture. It is theorized that these hot spots may be forming where there are voids within the material due to the manufacturing process or on areas where the weave pattern forms a dip in the surface of the material. This could cause an area where hot gases from the flame collect and cause the local temperature of the specimen in that area to be much higher than the rest of the area impinged on by the flame as observed during testing (see Figure 39).



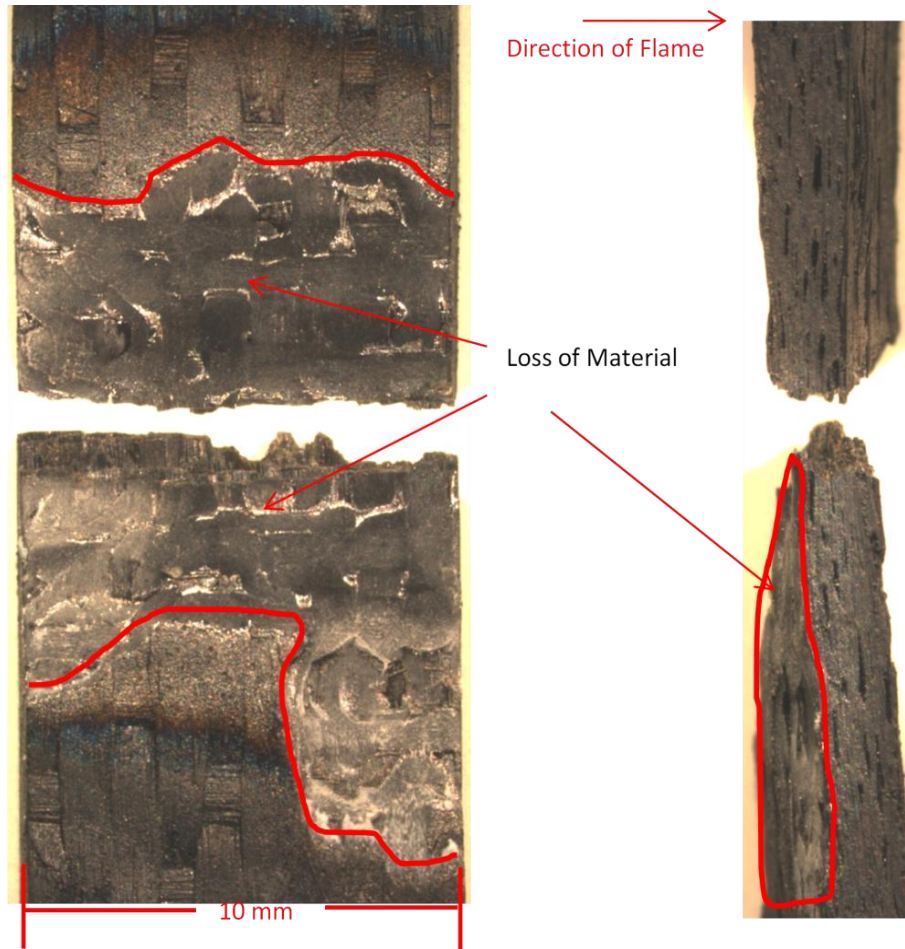


**Figure 69 - Specimen N811 Material Loss Over Time**



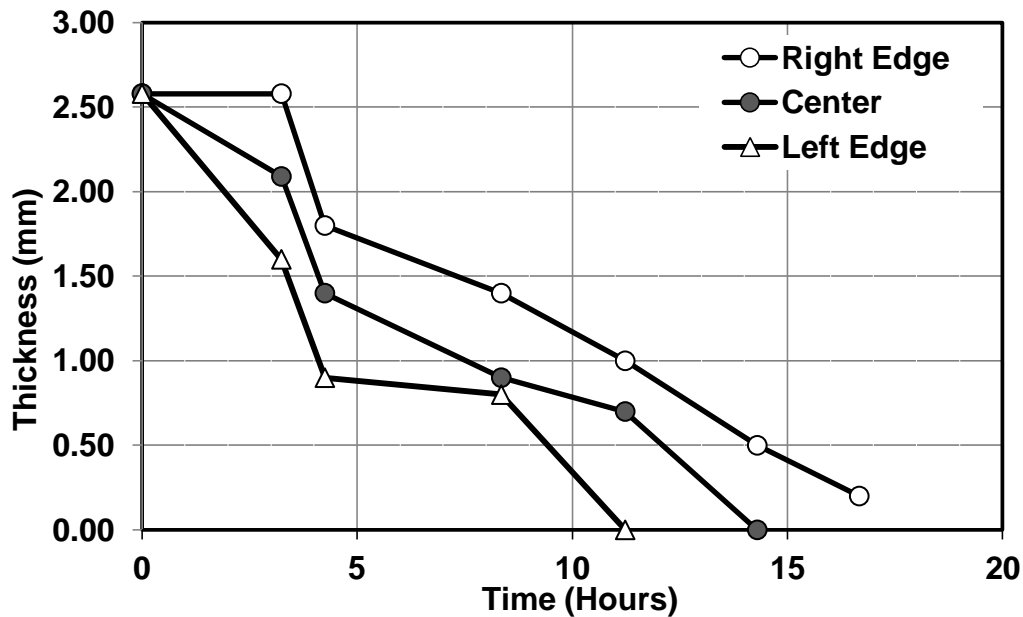
**Figure 70 - Thermal Images of Specimen N811 Hot Spot Development and Erosion**

Figure 71 shows images of specimen N811 after it was subjected to 16.7 hours of temperatures near 1480°C. It is clear that a large amount of the specimen was lost due to oxidation and erosion. Using the weight before and after testing and the density of the material, an estimated 194 mm<sup>3</sup> of material was lost. All of the material loss took place on the area where the flame impinged on the specimen.



**Figure 71 - N811 Loss of Material After 16.7 Hrs at a Temperature of 1480°C**

The combustion conditions that were present during this research were entered into the SiC recession empirical model developed by Robinson et al. The conditions that were input into the model were: a temperature of 1480°C, a gas composition of 14% O<sub>2</sub> and 35% H<sub>2</sub>O, a flame velocity of 100 m/s, and a pressure of 5 atm. With these conditions, the model predicts a recession rate of 3.5 µm/hr for pure SiC. Under these conditions the scale evaporates as fast as the material oxidizes, and reaches a steady state thickness of 0.8 µm [22]. The gas compositions that were entered into the model were based on measurements obtained by Kim et. al. during the initial setup of the burner test rig while achieving a surface temperature of 1250°C. To get the higher temperatures during this research the propane flow rate was increased so the model's predicted recession rate could be higher due to a difference in stoichiometry. However, the rates of recession of the material observed during testing were higher than what was predicted by the model. During the testing of specimen N811 (the zero stress specimen), measurements were taken of the right, left, and center thickness in the area of the flame. This data is shown in Figure 72. A recession rate of 0.18 mm/hr was calculated using this data. This shows that the force of the flame and the gases and particulate matter in the flame are removing material through erosion after the material is oxidizing due to the combustion environment.



**Figure 72 - Right, Center, and Left Edge Thickness Measurements of Specimen N811 vs. Time**

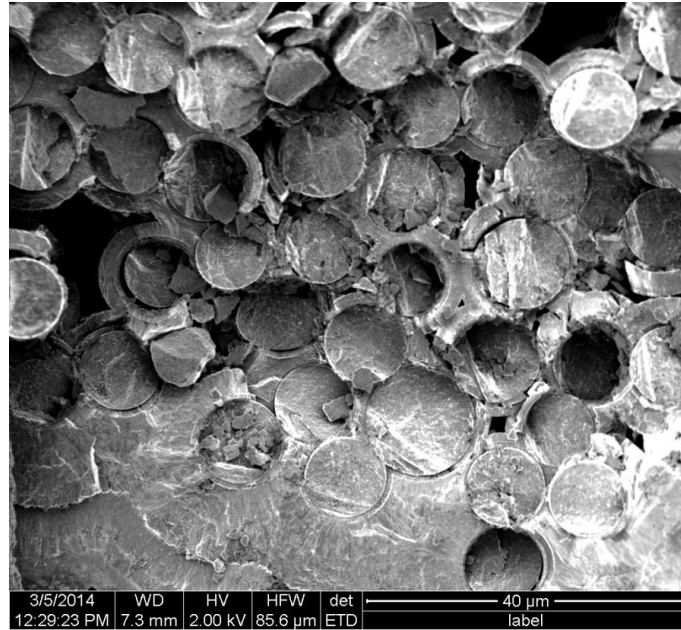
#### 4.6. Microstructural Analysis

Four specimens were selected to perform microstructural analysis on using images taken by the SEM as well as a specimen as fabricated. One specimen was chosen from each selected temperature and specimen N811 since it had the most loss of material. One side of the fracture surface was imaged in the SEM. Specimen N811 was also cut and polished as described in chapter 3.2.5 to observe any stovepiping or other phenomenon that may have traveled down the length of the specimen. Stovepiping is a phenomenon where gases from combustion travel down the length of the fibers of the CMC. Figure 73 and Figure 74 show SEM images of the cut surface of an un-tested specimen.



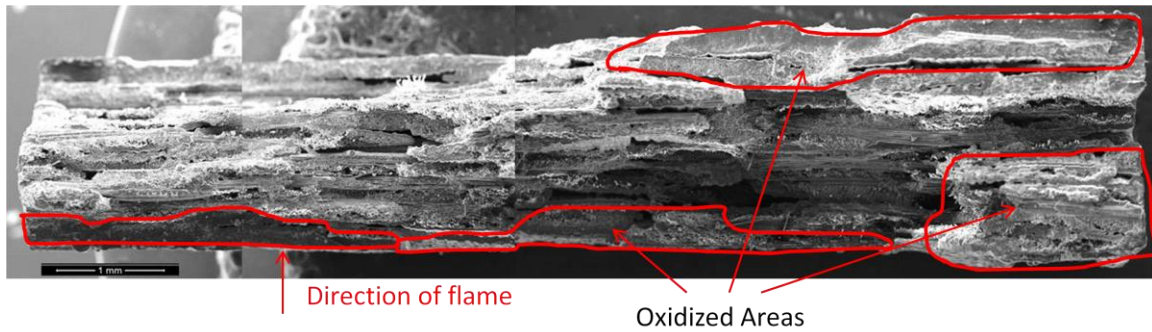


**Figure 73 - SEM Image of Un-tested Specimen**



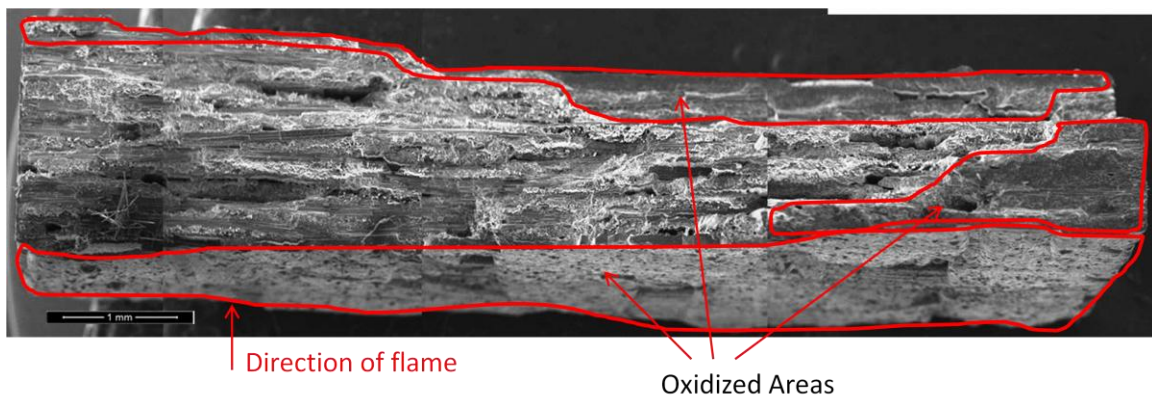
**Figure 74 - SEM Image of Un-tested Specimen Zoomed In to See Fibers**

Figure 75 through Figure 78 show SEM images of the overall fracture surfaces of each of the four specimens chosen for SEM imaging. Areas of oxidation and erosion are pointed out on the images. Areas of oxidation can be noticed by the fusing together of the matrix and the fibers. Areas of erosion will look the same, but there is a loss of material. All specimens show signs of oxidation along the surface of the specimen; that is not pointed out in these figures. Figure 75 is the overall fracture surface of the specimen tested at 1350°C and 210 MPa (N83). There are significant areas of oxidation on the material.



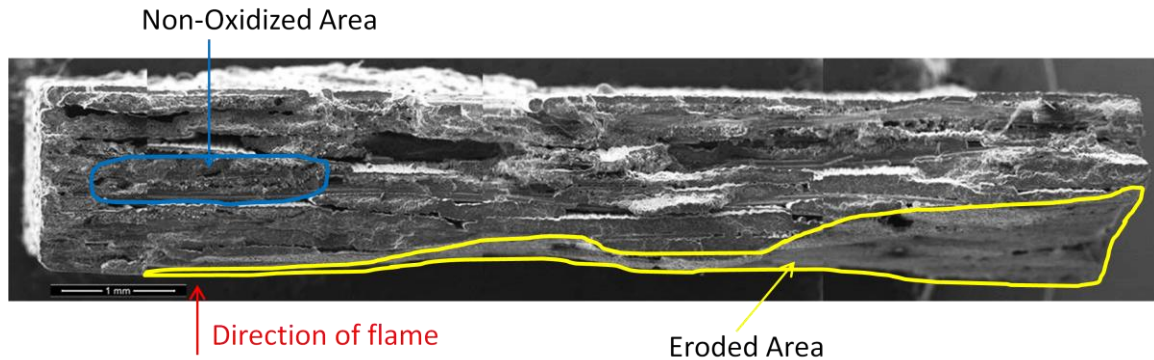
**Figure 75 - Specimen N83 SEM Image of Overall Fracture Surface**

Figure 76 is the overall fracture surface of the specimen tested at 1250°C and 175 MPa (N85). Even though this specimen was tested at a lower temperature than the previous specimen, it shows more areas of oxidation due to the fact it was subjected to the combustion conditions for a much longer amount of time (4,587 vs. 19,769 cycles).



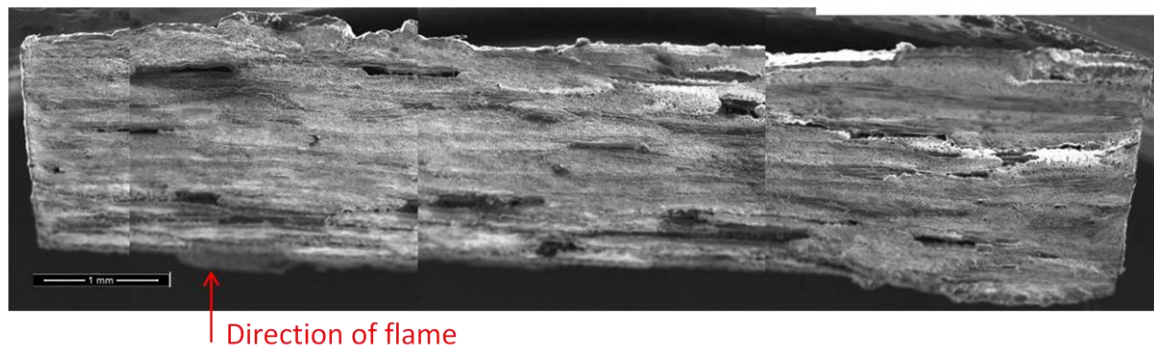
**Figure 76 - Specimen N85 SEM Image of Overall Fracture Surface**

The fracture surface of the specimen tested at 1480°C and 80 MPa (N810) was almost completely oxidized and showed some erosion on the flame side of the specimen. This is pointed out in Figure 77.



**Figure 77 - Specimen N810 SEM Image of Overall Fracture Surface**

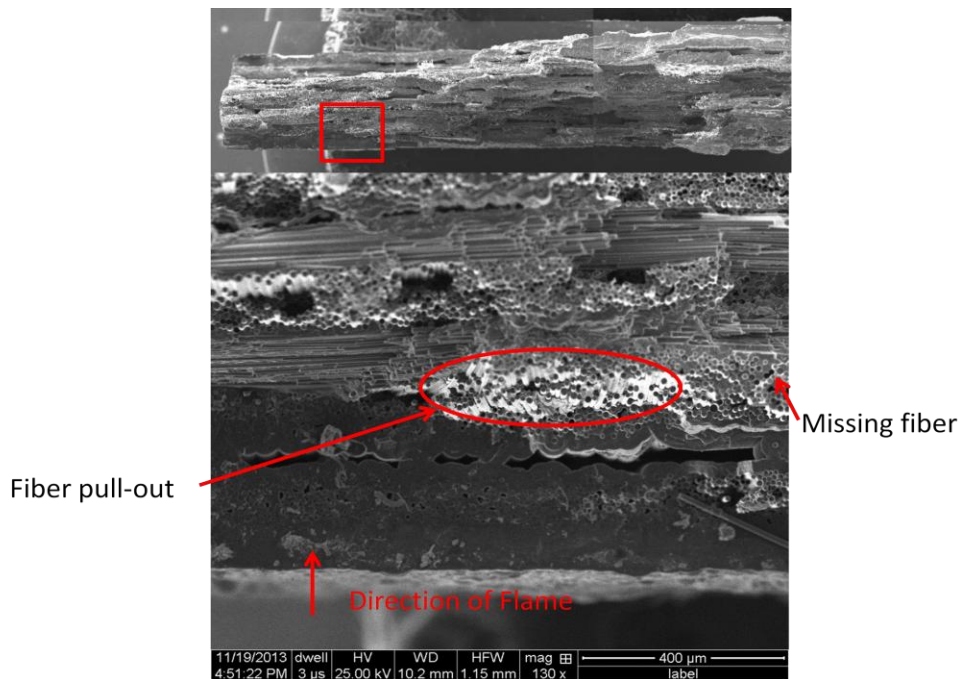
Figure 78 shows the overall failure surface of specimen N811. This specimen was tested at 1480°C with no loading. The entire surface of the specimen was eroded. This loss of material was the cause of failure of this specimen as explained in an earlier section.



**Figure 78 - Specimen N811 SEM Image of Overall Fracture Surface**

There were noticeable differences between the appearance of the microstructure of the specimens that saw different temperatures. It was also noticed that damage caused by the high temperatures produced by combustion existed near the surface of the specimen on both the flame side and reverse side of the specimen. The interior of the specimens did not see as much damage as near the surface with the exception of the specimens that saw temperatures of over 1400°C for longer periods of time.

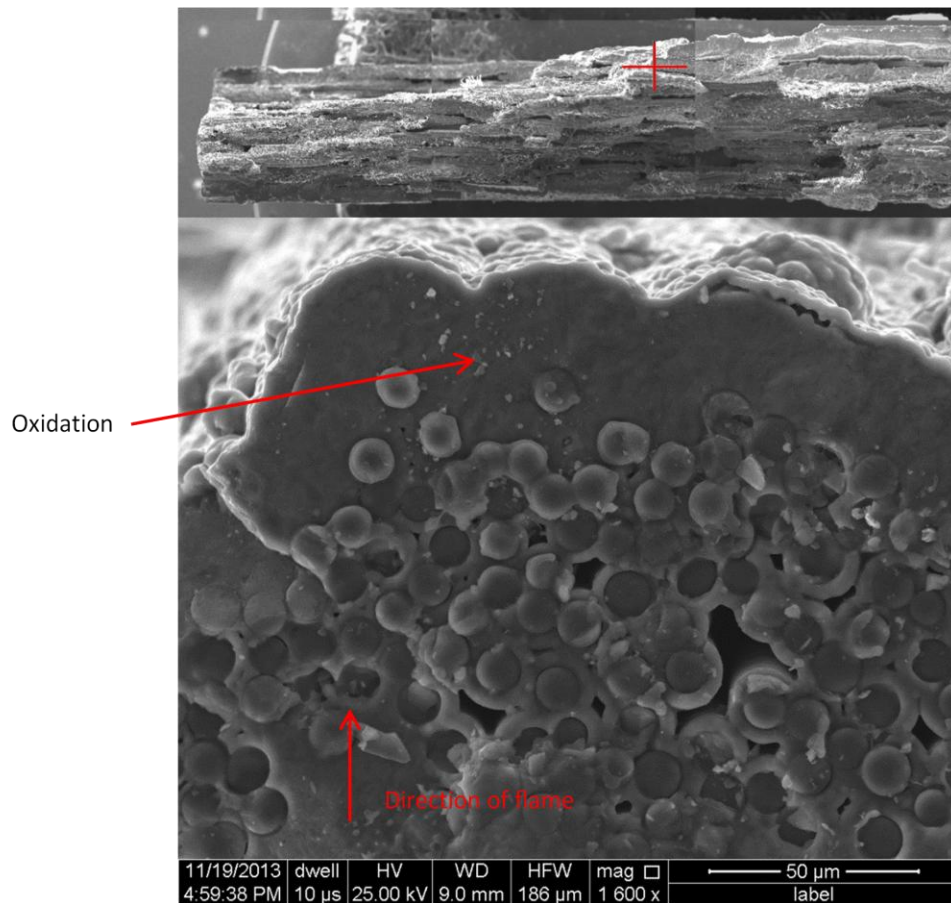
Figure 79 shows an SEM image of specimen N83. There is oxidation present near the surface of the flame side of the specimen, but moving into the interior of the specimen there is no oxidation and some fiber pull-out is present.



**Figure 79 - Specimen N83 Showing Signs of Fiber Pull-out**

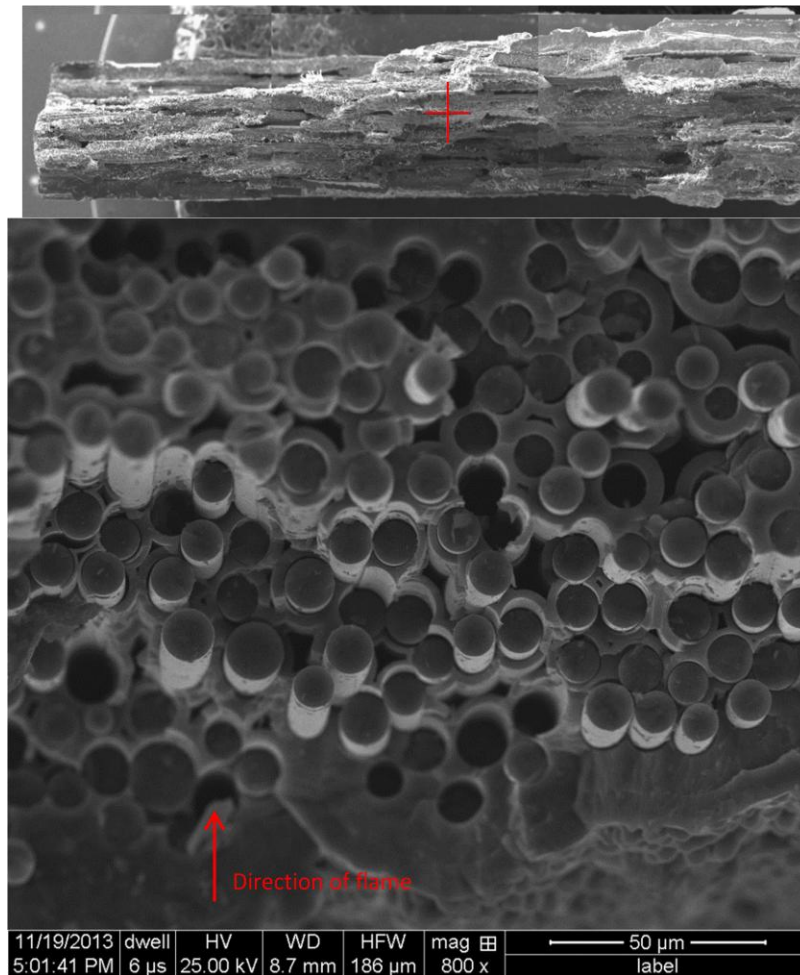


Figure 80 shows more oxidation near the surface of specimen N83. This SEM image was taken near the edge of the specimen that was located away from the flame. This means that hot gases from combustion are heating the backside of the specimen enough to cause some degradation in the material there as well. The temperatures on the back side of the specimen were 200°C below the temperatures on the front side as observed in Figure 40.



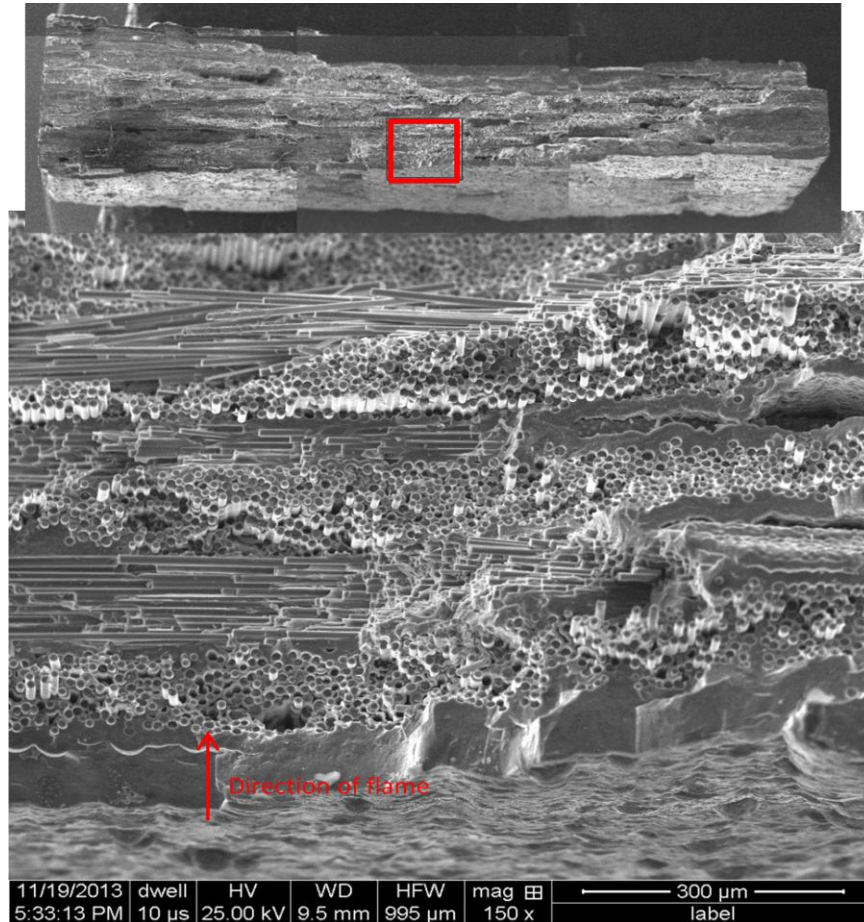
**Figure 80 - Oxidation on Specimen N83**

The SEM image in Figure 81 shows some of the fibers still intact and the interface between the fibers and the matrix is still present. This image was taken in the interior of the specimen and does not show signs of oxidation as the images near the surface do.



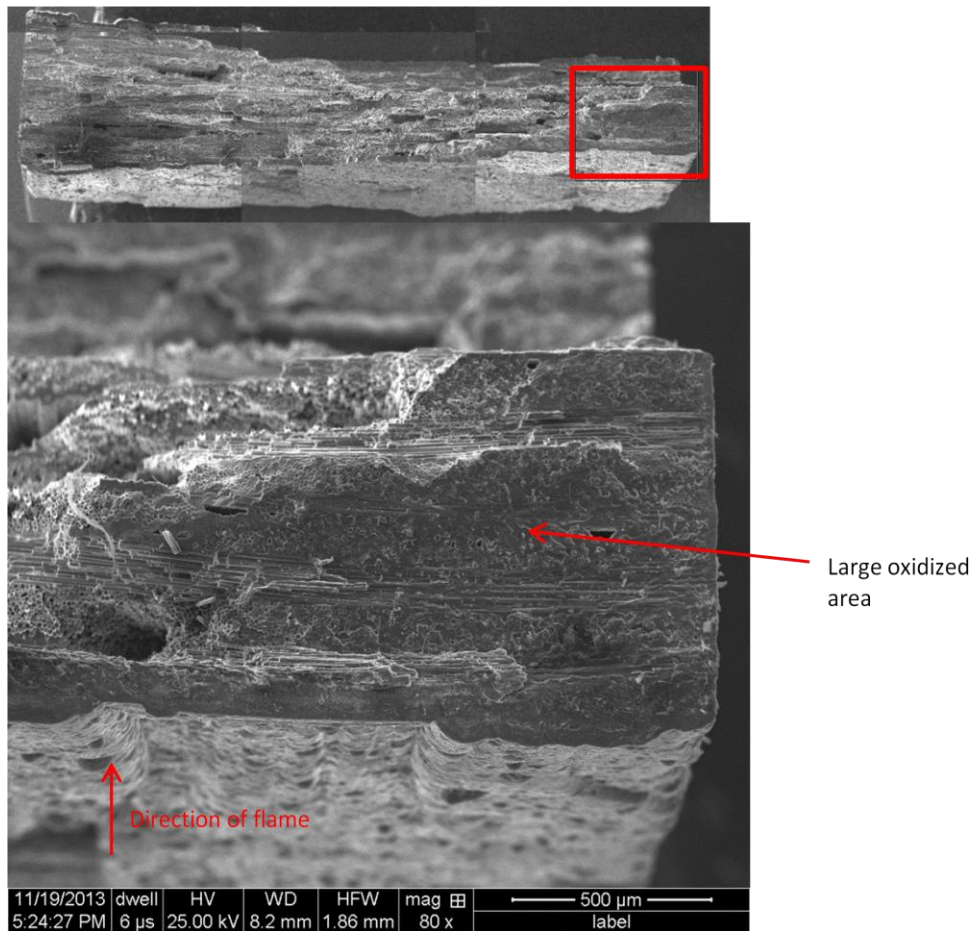
**Figure 81 - Specimen N83 With Some Fiber Pull-out**

Figure 82 is an SEM image taken in the interior of specimen N85. The 90° and 0° fibers can be easily identified since there is not any oxidation occurring in this area of the specimen.



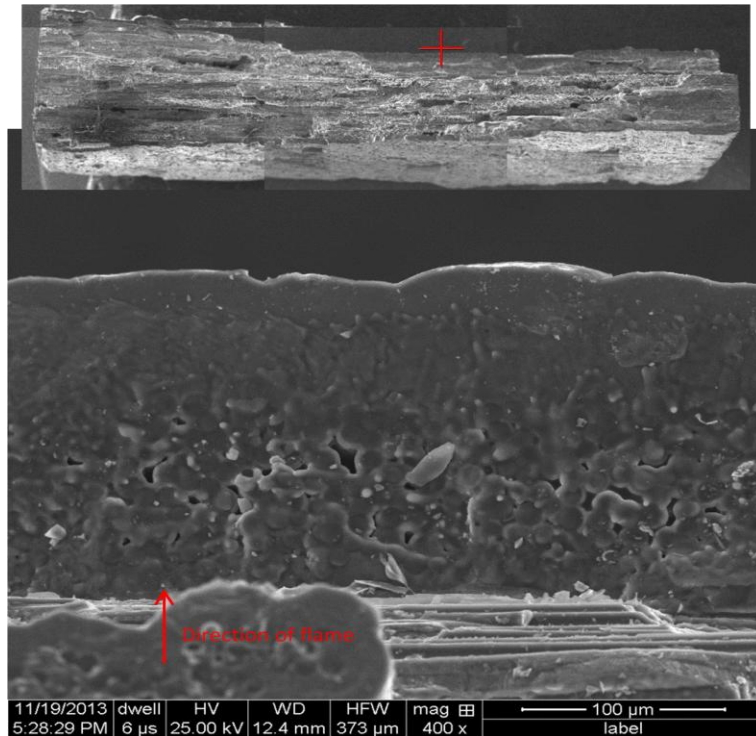
**Figure 82 - Center of Specimen N85 No Signs of Oxidation**

Figure 83 and Figure 84 show SEM images of specimen N85 where areas of the material near the surface have been oxidized. In Figure 84 the matrix and fibers have been fused together to a point where it is almost impossible to tell them apart.



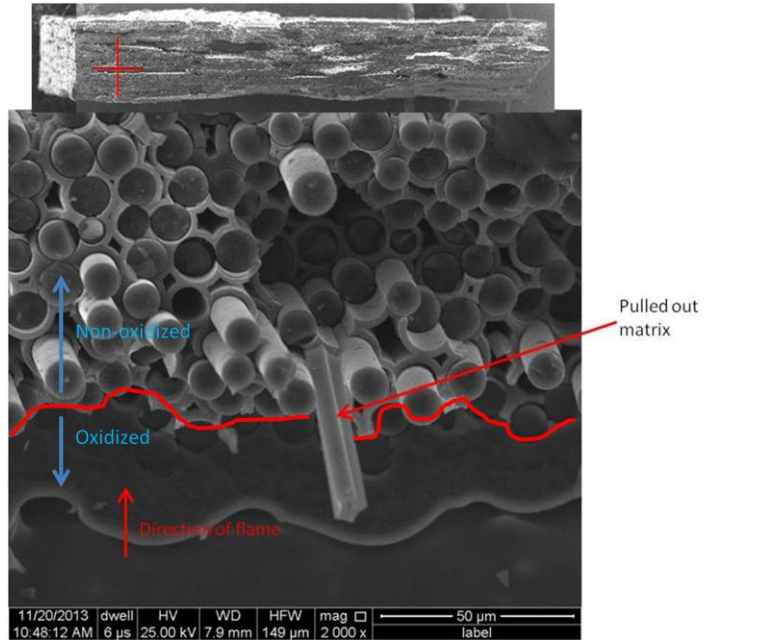
**Figure 83 - Specimen N85 Large Area of Oxidized Material**



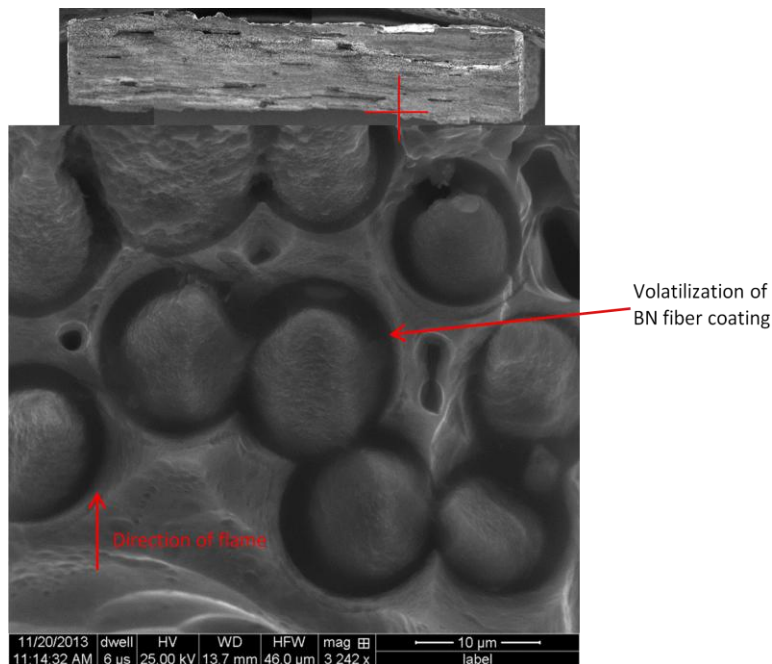


**Figure 84 - Specimen N85 Area of Oxidation Where the Fibers and Matrix are Fused Together**

Figure 85 shows an SEM image of specimen N810 with some fiber pull-out and one piece of matrix material sticking out of the specimen. There may also be some volatilization of the BN coating of the SiC fibers occurring as well. The BN coating oxidizes to form  $B_2O_3$ , which is then volatilized by reaction with water [12]. This phenomenon can better be seen in Figure 86 along with the oxidation of the SiC fibers and matrix.

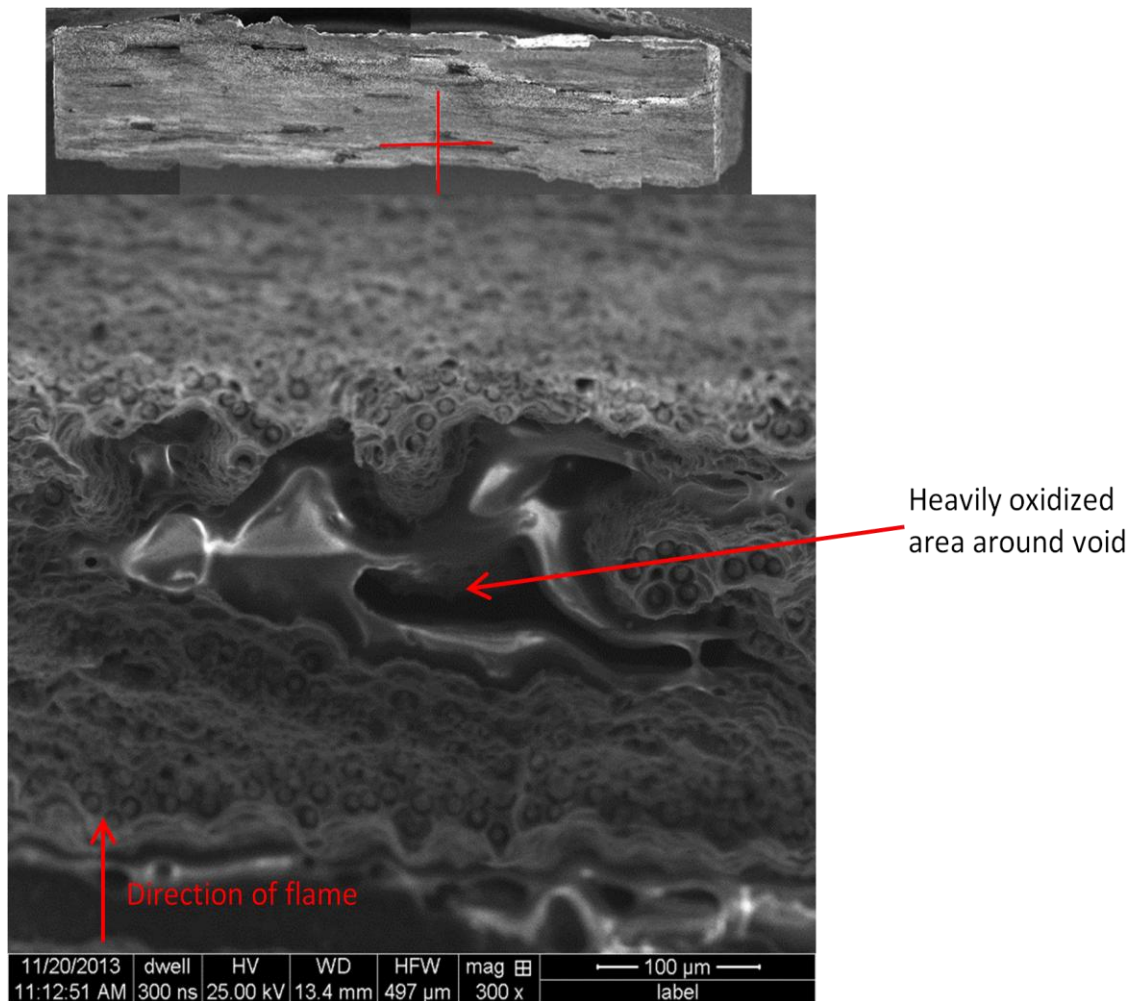


**Figure 85 - Specimen N810 Piece of Matrix Material Extending out of Surface and Areas of Oxidized and Non-Oxidized Material**



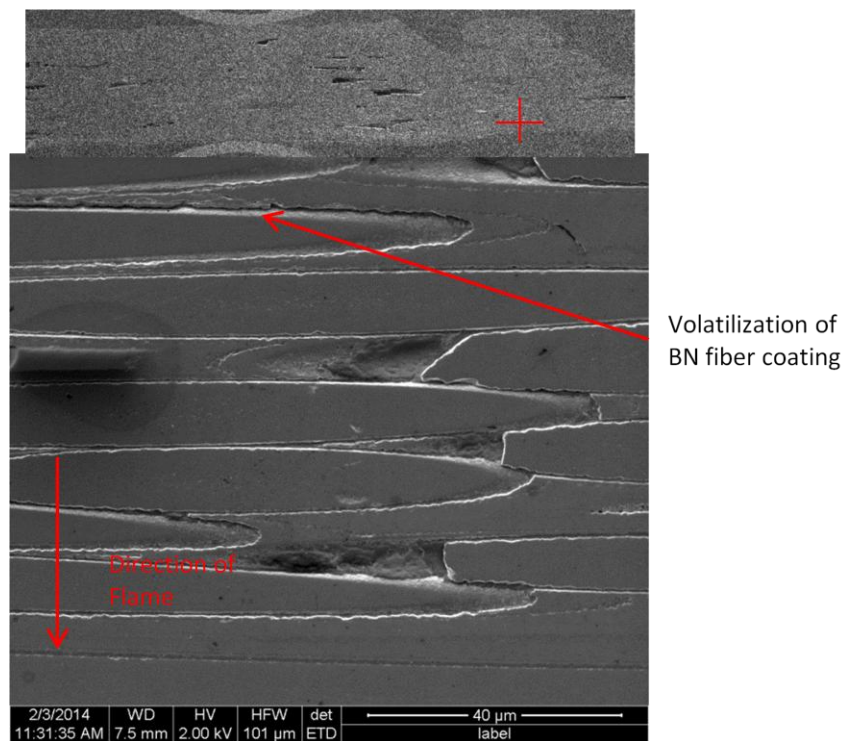
**Figure 86 - Volatilization of the BN Fiber Coating and Oxidation of Fibers and Matrix on Specimen N811**

Figure 87 shows an area of heavy oxidation near the flame side surface of specimen N811 around one of the voids in the matrix.



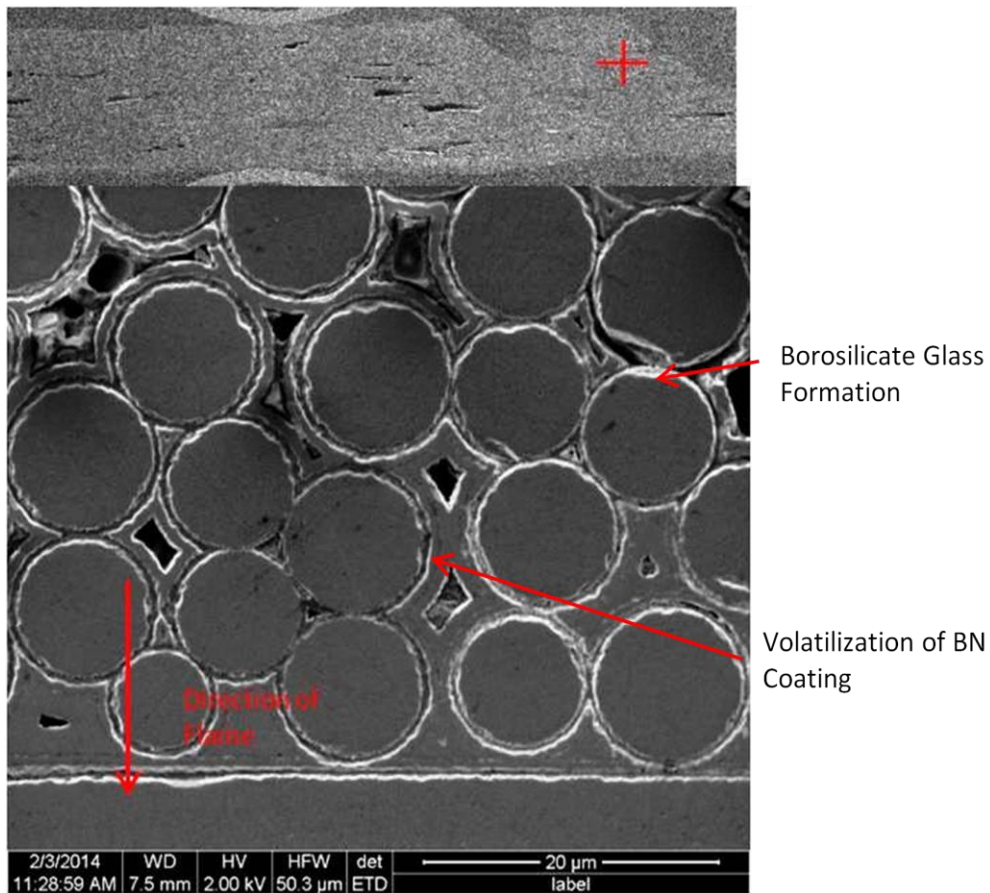
**Figure 87 - Heavily Oxidized Area Around a Void in Specimen N811**

Since specimen N811 experienced the hottest temperatures for the longest period of time, it was decided to perform additional microstructural analysis on this specimen. The specimen was cut, mounted, and polished as described in chapter 3.2.5. This SEM images of the cut and polished piece did reveal that stove piping along the fibers is occurring. This is evident in Figure 88. The combustion gases are causing the BN coating around the fibers to volatilize leaving no fiber-matrix interface. This image was taken near the surface of the specimen on the backside.



**Figure 88 - Stove Piping Occurring Along the Length of the Fibers in Specimen N811**

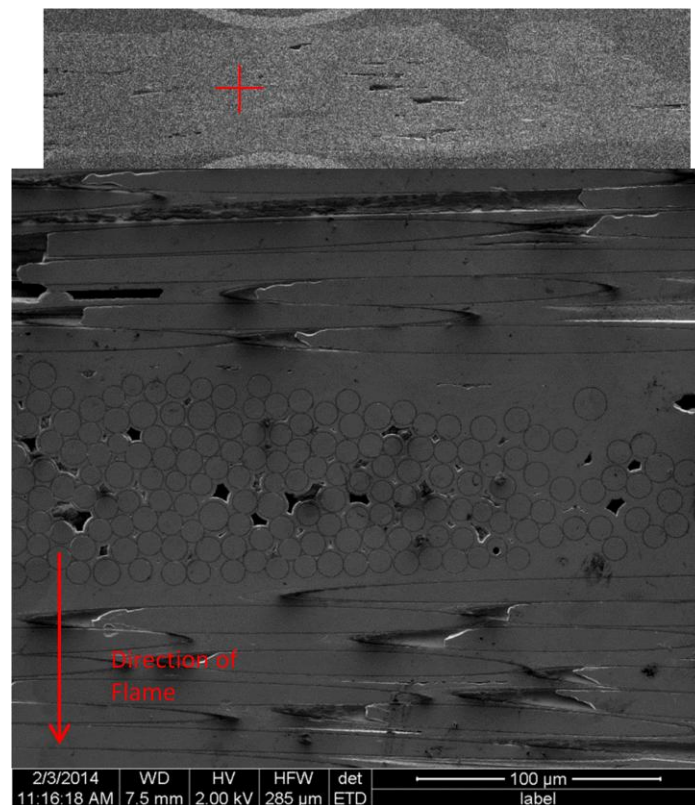
The SEM image in Figure 89 shows some volatilization of the BN fiber coating along with some formation of borosilicate glass around the surface of the fibers. Around some of the fibers as pointed out in the figure, there is a gap between the fiber and the matrix where the BN coating has volatilized. There are also some areas around the circumference of the fibers that have formed borosilicate glass as pointed out in the figure.



**Figure 89 - Specimen N811 Volatilization of BN Coating and Formation of Borosilicate Glass**



Even at high temperatures of near 1480°C, the interior of the specimen does not show signs of oxidation. Figure 90 shows an SEM image of specimen N811 taken within the bulk of the specimen away from the spot where the flame was impinging on the specimen. There are no signs of oxidation or other issues caused by the combustion environment. It appears that oxidation is only occurring near the surface for the most part with the exception of specimens N810 and N811. These two specimens had oxidation present throughout the entire fracture surface. However, as temperature is increased the depth of penetration of the oxidation increases.



**Figure 90 - SEM Image of Specimen N811 No Noticeable Damage Due to Combustion Environment**

#### **4.7. Results Summary**

The fatigue behavior of the material while in a combustion environment does show a dependence on the temperature the specimen is heated to by the flame. This is evident when looking at the S-N curved developed during this research (Figure 43). At temperatures of over 1450°C, the loss of material due to oxidation, vaporization, and erosion is so great that it is impossible to achieve run-out of 25 hrs with any fatigue loading. At temperatures below 1350°C, the material only exhibited some signs of loss of material when exposed to the combustion environment for a relatively long period of time.

Residual strength tests revealed the retained properties of the two specimens that survived fatigue loading in the combustion environment to run-out. Both specimens did suffer a loss of strength after fatigue testing. The specimen tested at 1350°C did retain more strength than the specimen tested at 1250°C, but the specimen tested at 1250°C was tested at a higher max stress fatigue load. Since the specimen tested at 1350°C did retain more strength, it is possible that it could have achieved run-out at a max stress level between 90 MPa and 125 MPa.

Microscopy was able to show that oxidation and volatilization of material due to the combustion environment is occurring within the material near the surface on both the flame side and backside of the specimens. Some of this oxidation and volatilization even traveled down the length of the fibers in the material affecting the matrix-fiber interface. This oxidation is starting a process of material loss that is accelerated by the velocity of the flame leading to a depredation of the material caused mostly by erosion in addition to weakening the material.

## **V. Conclusions and Recommendations**

While subjected to a combustion environment and fatigue loading, the HyperTherm Sylramic-iBN/BN/CVI SiC CMC material performed well when considering the conditions the material was exposed to. At temperatures below 1250°C, the material did not show signs of degradation due to the combustion environment and was able to achieve run-out during fatigue testing with a max stress of 33% of the UTS at room temperature. At temperatures below 1350°C, the material achieved run-out with a max stress of 24% of the room temperature UTS. Temperatures above 1450°C is where the material did not do as well. It was not possible to achieve run-out at these temperatures since the material degraded so much. However, it is important to understand there are not many materials able to withstand these temperatures. Even the most advanced superalloy metals are unable to withstand temperatures over 1000°C without cooling [8].

The main reason for the failures at temperatures over 1450°C in the combustion environment is due to the amount of material lost during testing. This is something that is not present when testing in a furnace. The high temperatures in conjunction with the water vapor present due to the combustion process cause oxidation of the material to start taking place. The velocity of the flame combined with particles in the flame present due to the combustion process leads to an accelerated loss of material due to erosion. The physical nature of the material also contributes to the start of the removal of material. Non-uniformities in the surface of the material or voids within the material cause hot spots to develop on the surface of the specimen in the area where the flame is impinging. These hot spots reached temperatures upwards of 1650°C locally and contribute

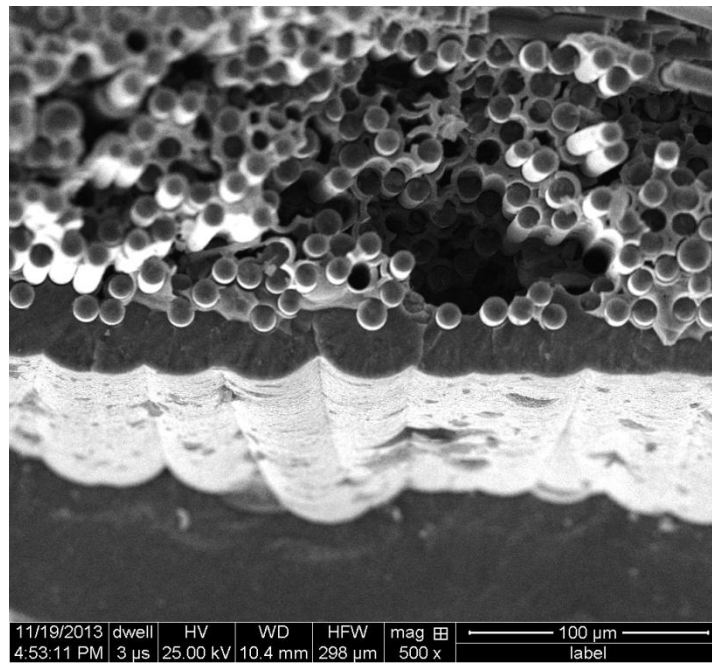


significantly to erosion on the surface. Improvements to the material to limit this phenomenon could potentially allow the material to achieve run-out at an average temperature of 1480°C in the combustion environment.

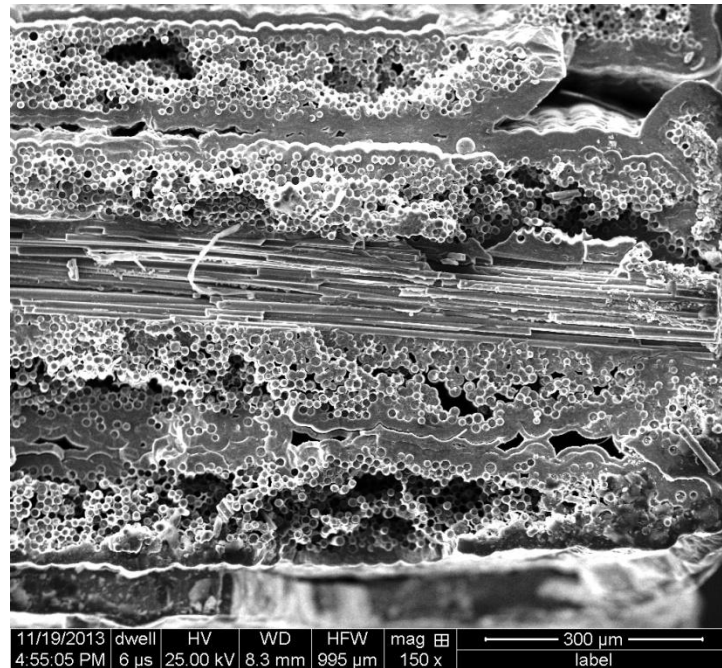
In the future, there are some areas worth studying that were not covered by this research. One thing that would be of interest would be to x-ray the material before testing in the combustion environment to determine where any voids are present in the material. This information would be useful when observing the development of hot spots during combustion environment testing. This could confirm if the hot spots are forming in areas where voids within the material are present or where the weave pattern of the fibers cause a dip in the surface. Another area of interest would be to explore the effects of a thermal barrier coating on the material. This could possibly make the material surface smoother and prevent the development of hot spots.

## Appendix

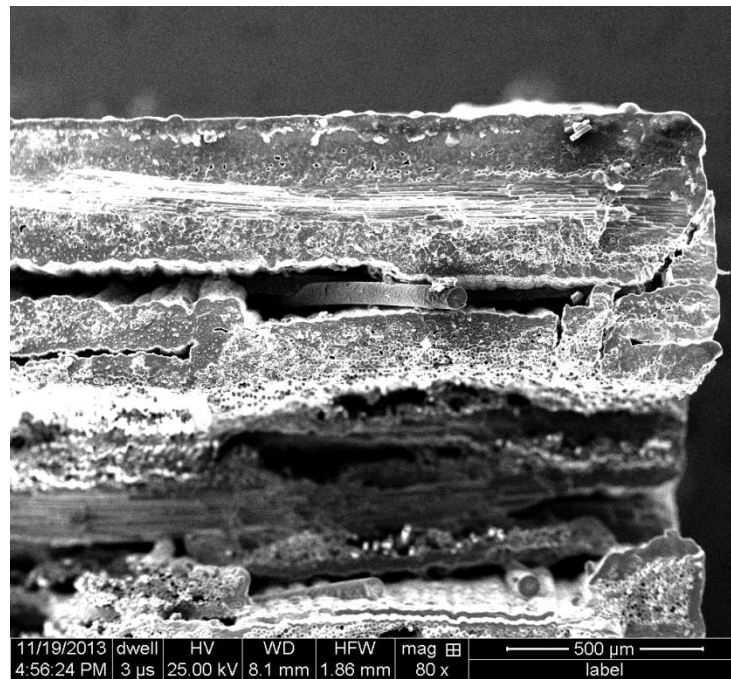
Figure 91 through Figure 95 are additional SEM images of the fracture surface of specimen N83 which was tested at a temperature of 1350°C and a max stress of 210 MPa. This specimen lasted through 4,587 cycles.



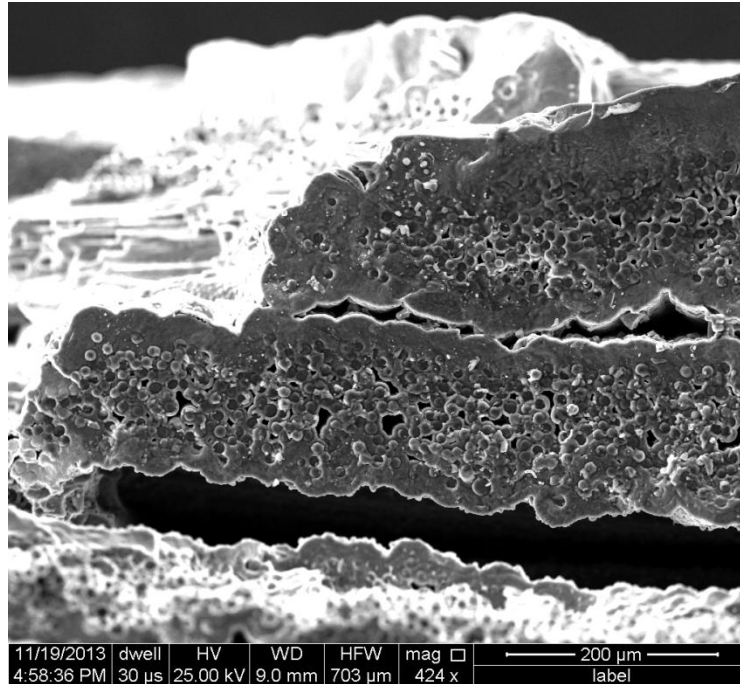
**Figure 91 - SEM Image of Specimen N83 Flame Side Center, 500x**



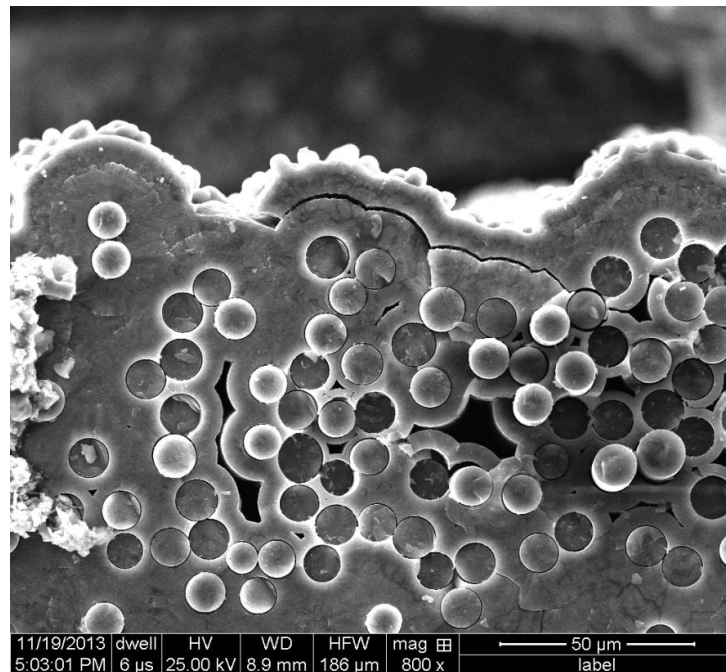
**Figure 92 - SEM Image of Specimen N83 Flame Side Right, 150x**



**Figure 93 - SEM Image of Specimen N83 Backside Right, 80x**

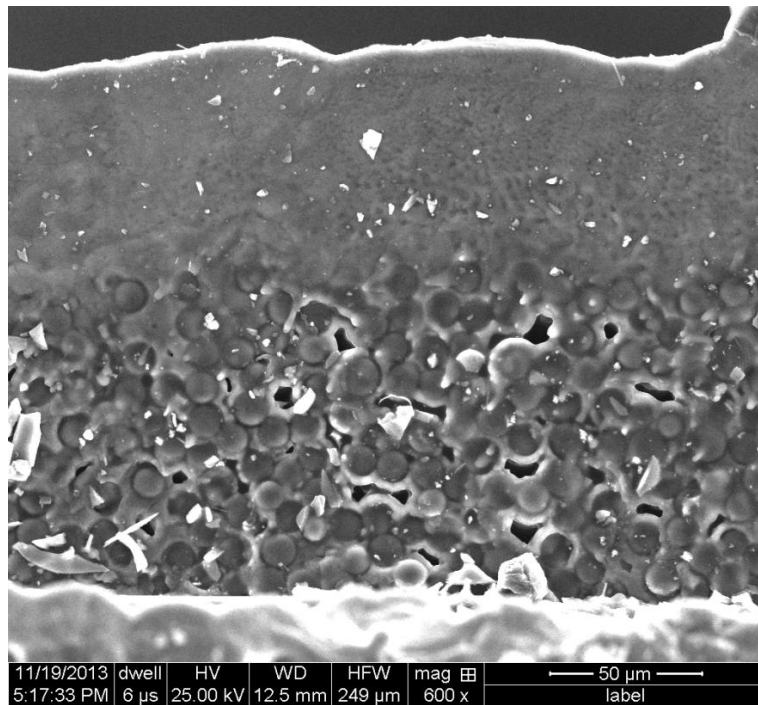


**Figure 94 - SEM Image of Specimen N83 Backside Center, 424x**

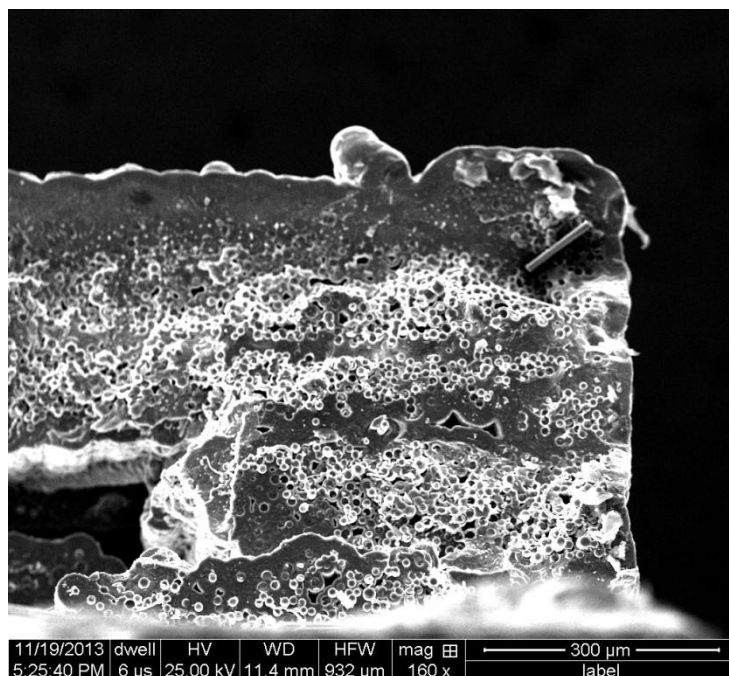


**Figure 95 - SEM Image of Specimen N83 Center of Thickness Right Side, 800x**

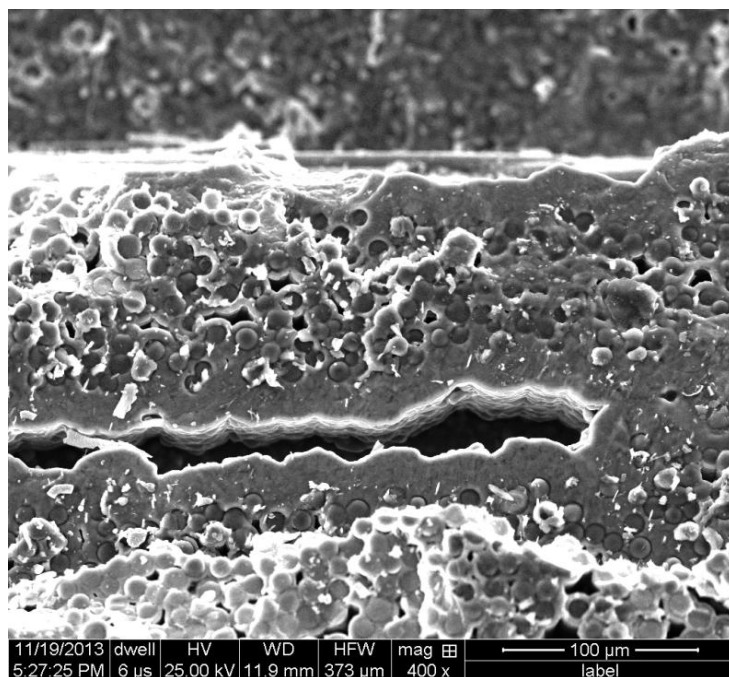
Figure 96 through Figure 102 show additional SEM images of specimen N85 which was tested at a temperature of 1250°C and a max stress of 175 MPa. This specimen survived to 19,769 cycles.



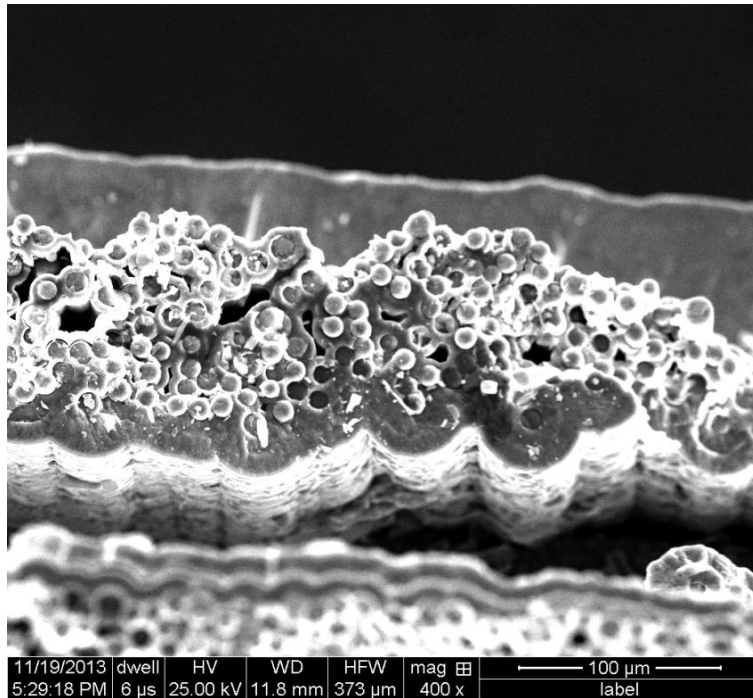
**Figure 96 - SEM Image of Specimen N85 Backside Center, 600x**



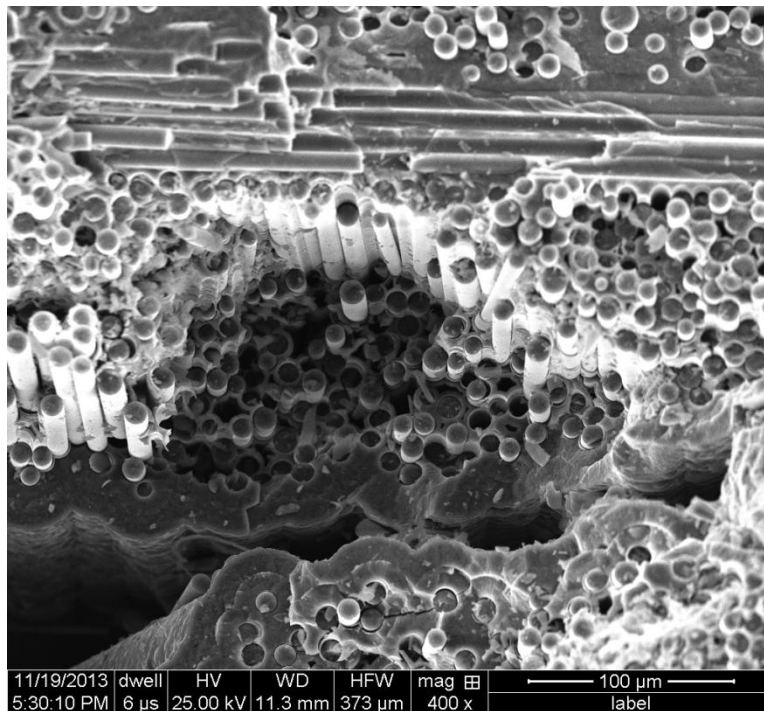
**Figure 97 - SEM Image of Specimen N85 Backside Right, 160x**



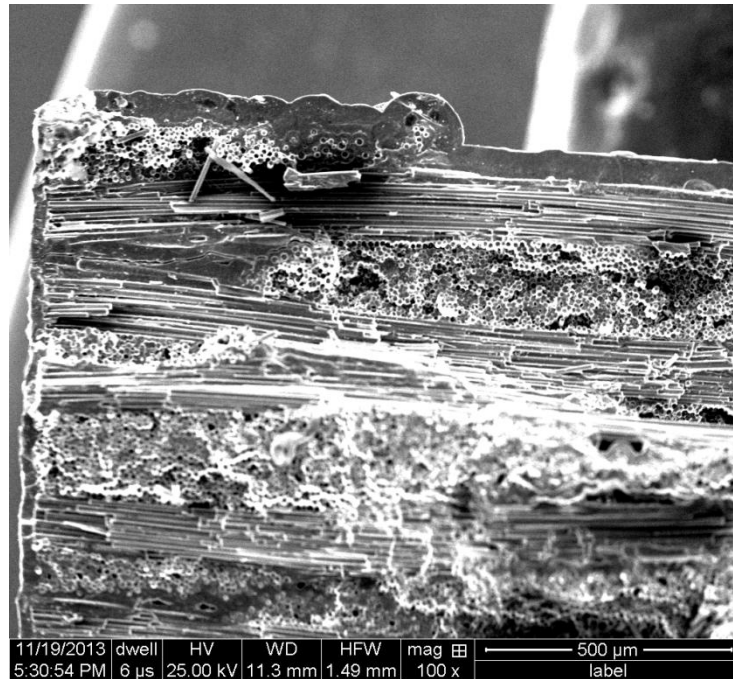
**Figure 98 - SEM Image of Specimen N85 Backside Center, 400x**



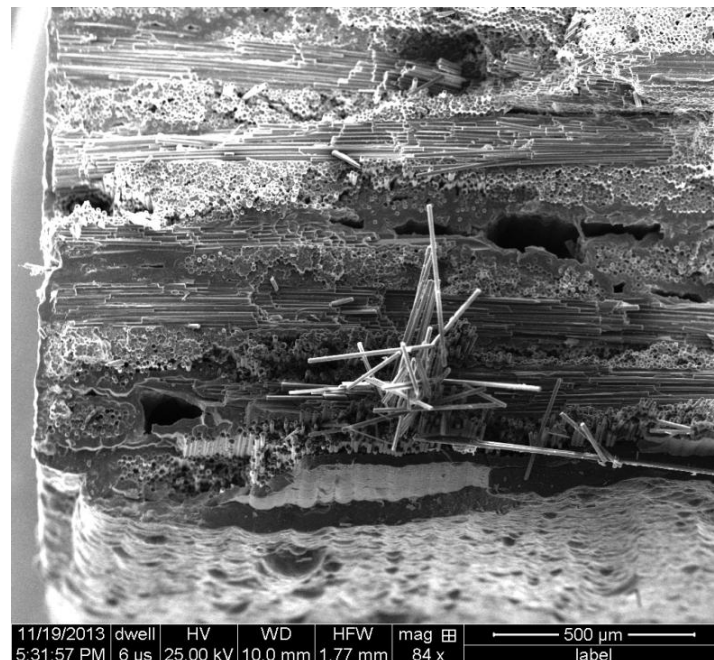
**Figure 99 - SEM Image of Specimen N85 Backside Center, 400x**



**Figure 100 - SEM Image of Specimen N85 Backside Left, 400x**



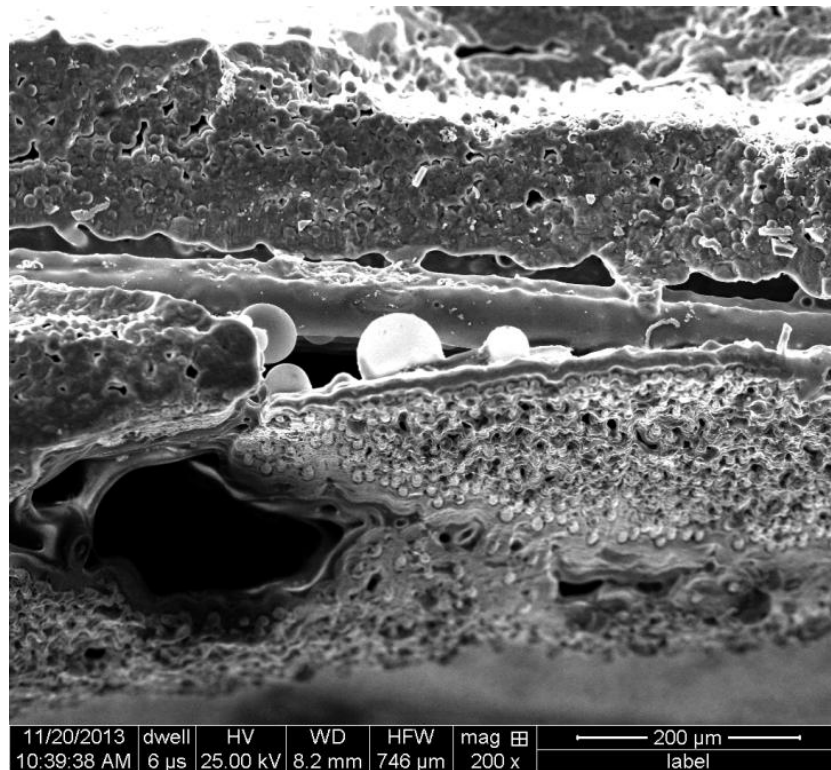
**Figure 101 - SEM Image of Specimen N85 Backside Left, 100x**



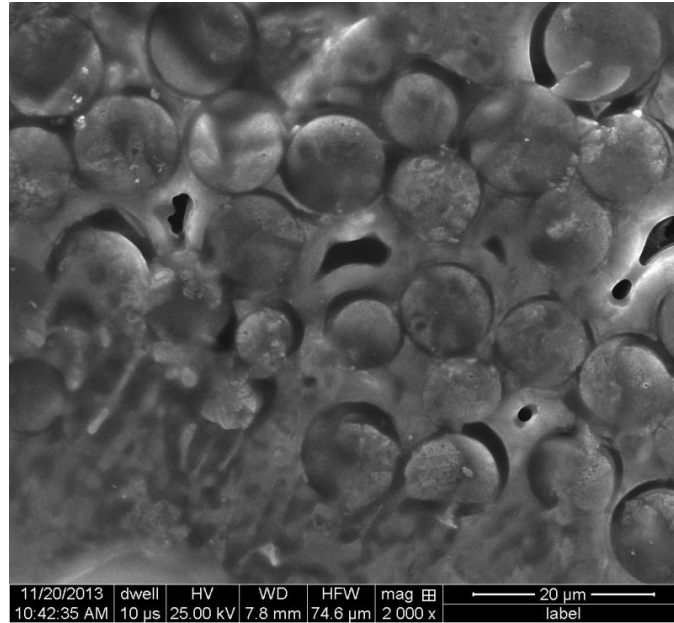
**Figure 102 - SEM Image of Specimen N85 Flame Side Left, 84x**



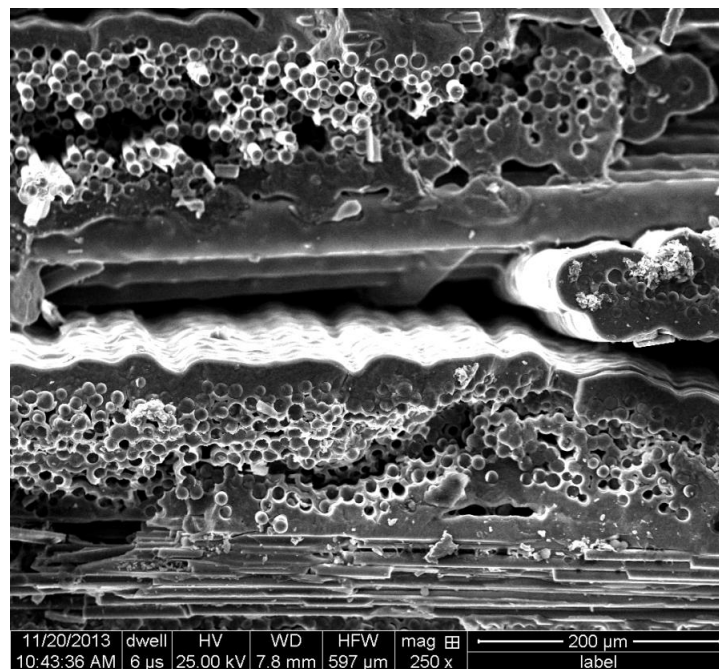
Figure 103 through Figure 109 contain additional SEM images of the fracture surface of specimen N810 which was tested at a temperature of 1480°C and a max stress of 80 MPa. This specimen reached 15,462 cycles during testing.



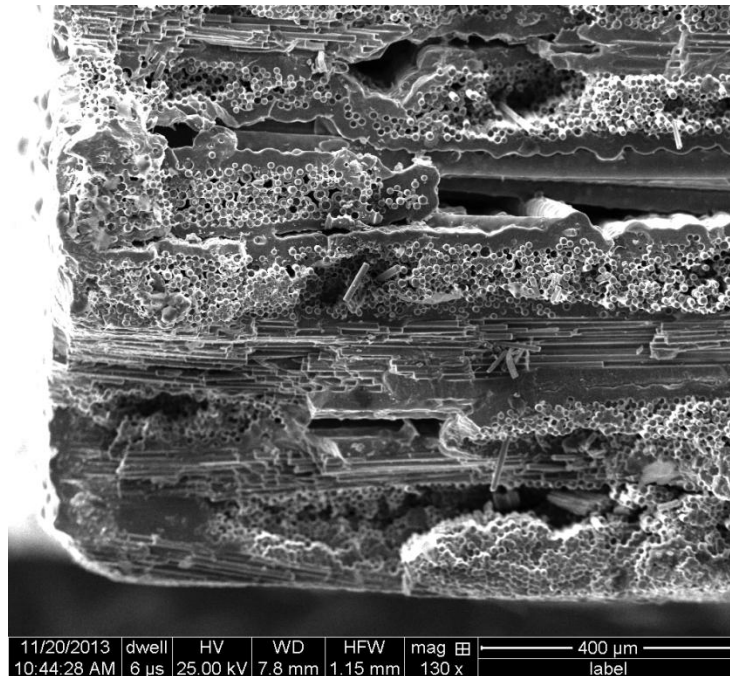
**Figure 103 - SEM Image of Specimen N810 Flame Side Right, 200x**



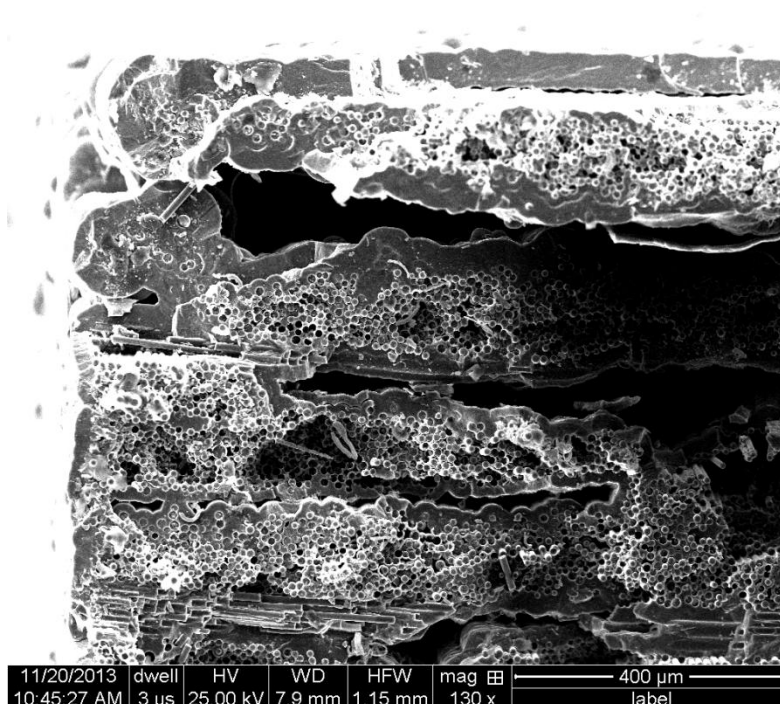
**Figure 104 - SEM Image of Specimen N810 Flame Side Center, 2000x**



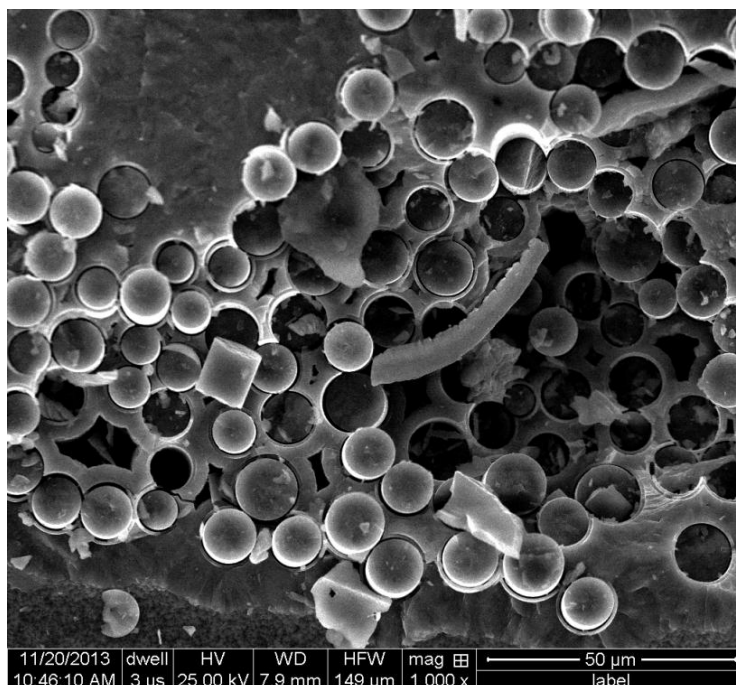
**Figure 105 - SEM Image of Specimen N810 Flame Side Left, 250x**



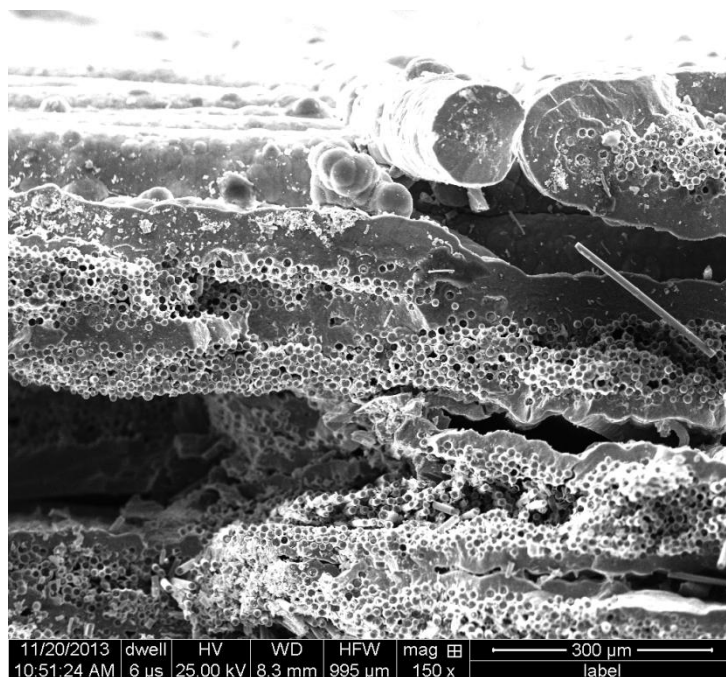
**Figure 106 - SEM Image of Specimen N810 Flame Side Left, 130x**



**Figure 107 - SEM Image of Specimen N810 Back Side Left, 130x**

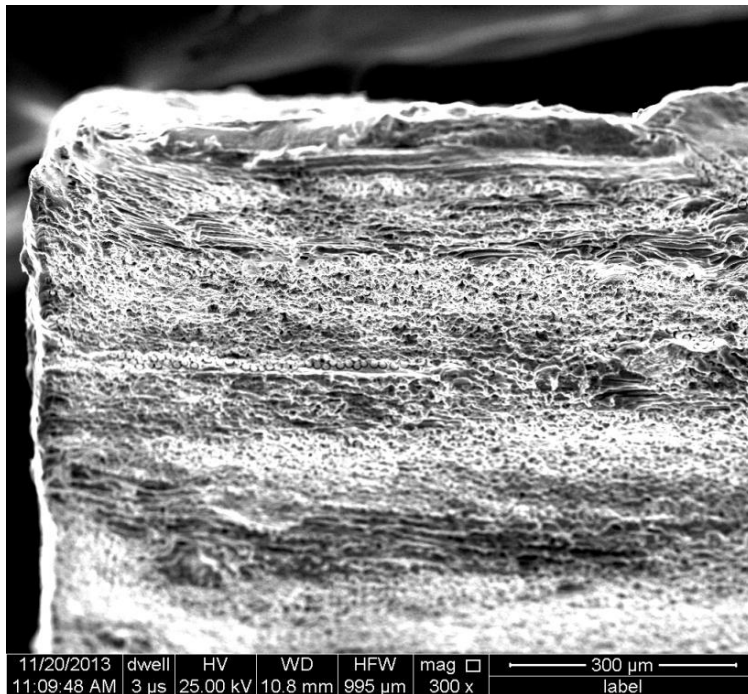


**Figure 108 - SEM Image of Specimen N810 Back Side Left, 1000x**

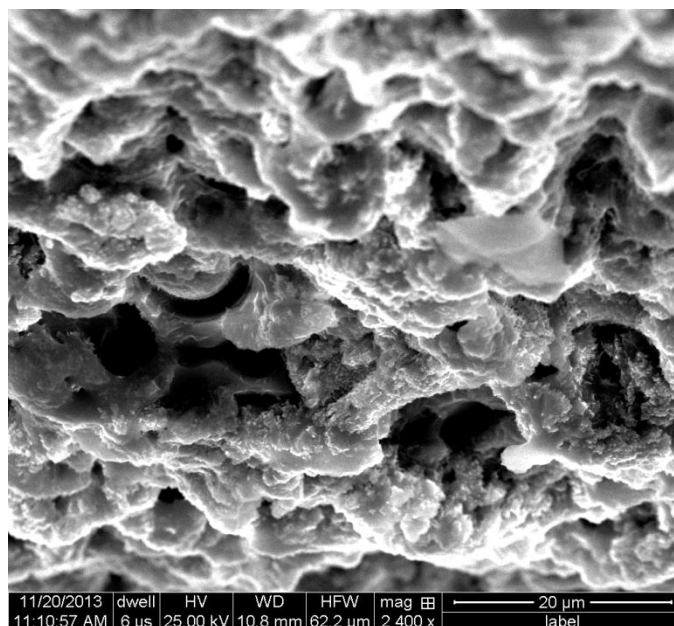


**Figure 109 - SEM Image of Specimen N810 Back Side Center, 150x**

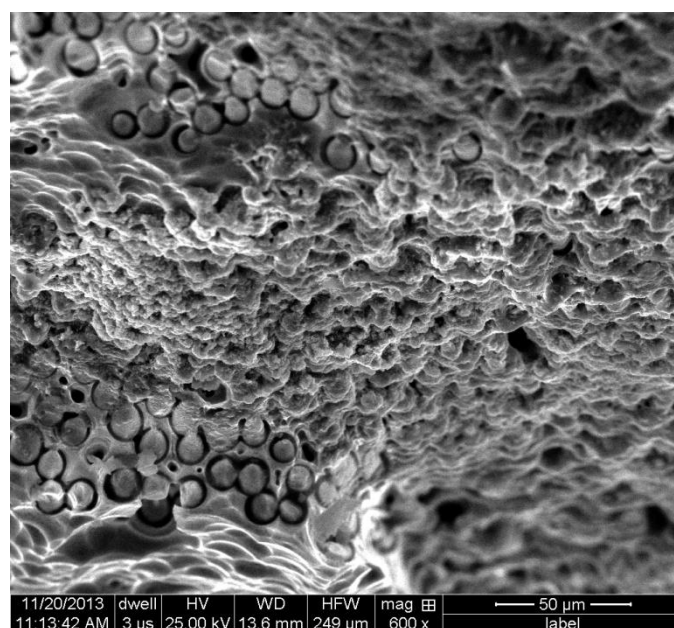
Figure 110 through Figure 116 are additional SEM images of the failure surface of specimen N811. This specimen was tested at a temperature of 1480°C with no applied fatigue loading. The specimen lasted 16.67 hours in the combustion environment.



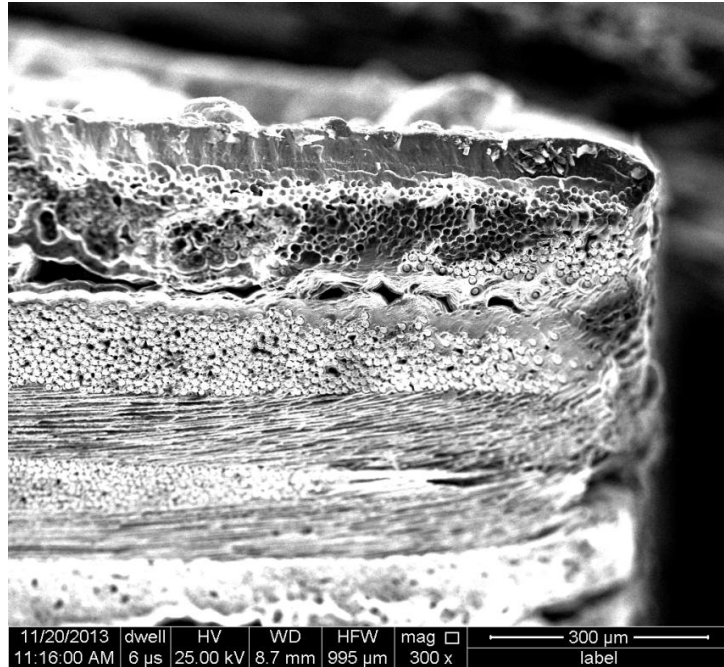
**Figure 110 - SEM Image of Specimen N811 Back Side Left, 300x**



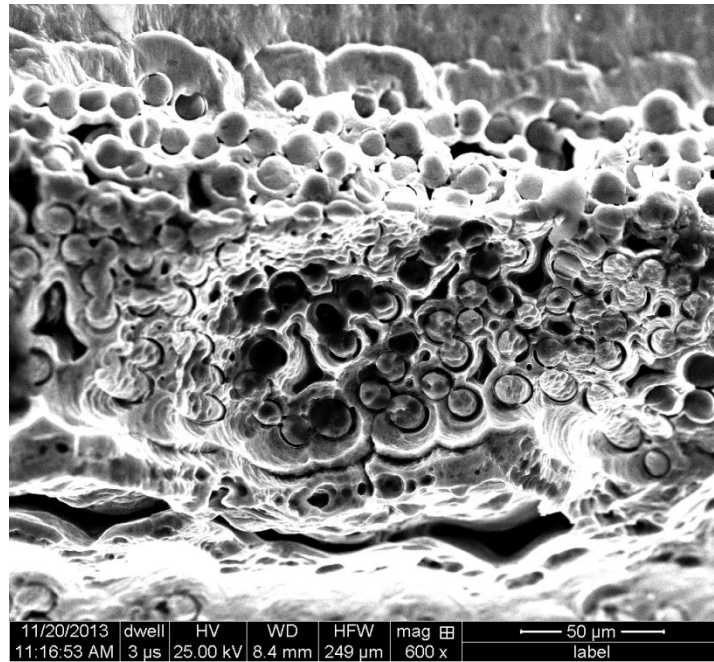
**Figure 111 - SEM Image of Specimen N811 Back Side Left, 2400x**



**Figure 112 - SEM Image of Specimen N811 Flame Side Right, 600x**

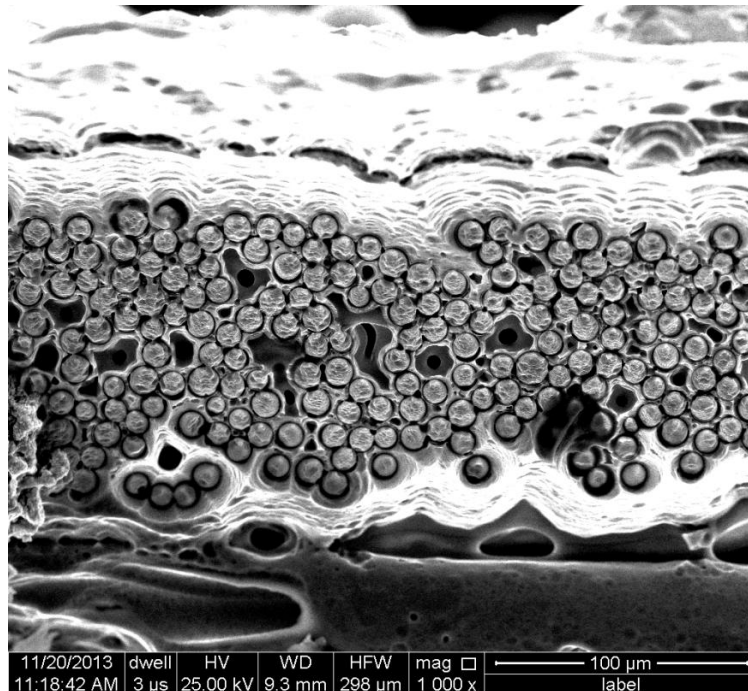


**Figure 113 - SEM Image of Specimen N811 Back Side Right, 300x**

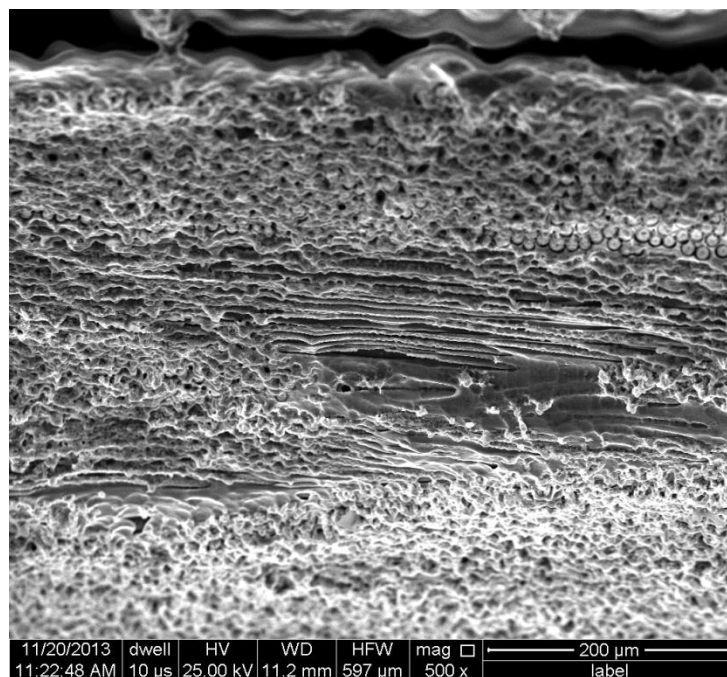


**Figure 114 - SEM Image of Specimen N811 Back Side Right, 600x**





**Figure 115 - SEM Image of Specimen N811 Back Side Center, 1000x**



**Figure 116 - SEM Image of Specimen N811 Back Side Center, 500x**



## Bibliography

1. Auxier, Thomas A. *The Importance of Cooling Technology in Propulsion & Power Systems*. Tech. no. (SYB) KN2-1. N.p.: n.p., 2003. Print.
2. Chamberlain, Adam, and Robert Shinavski. "2700F SiC/SiC Annual Update." Wright-Patterson AFB, Dayton, OH. 12 Dec. 2012. Lecture.
3. Chawla, Krishan Kumar. *Ceramic Matrix Composites*. London: Chapman & Hall, 1993. Print.
4. Cinibulk, Michael K. "Introduction to Ceramic-Matrix Composites." Wright-Patterson AFB, Dayton, OH. Lecture.
5. FLIR Systems. *ThermaCAM PM695 Operator's Manual*. 2000. Portland, OR.
6. Fox, Dennis S., Elizabeth J. Opila, and Raiford E. Hann. "Paralinear Oxidation of CVD SiC in Simulated Fuel-Rich Combustion." *Journal of the American Ceramic Society* 83.7 (2000): 1761-767. Print.
7. Gell, M., D. N. Duhl, and A. F. Giamei. *The Development of Single Crystal Superalloy Turbine Blades*. Tech. N.p.: n.p., 1980. Print.
8. "High Temperature Coatings." *Wadley Research Group*. N.p., n.d. Web. 22 Feb. 2014. <<http://www.virginia.edu/ms/research/wadley/high-temp.html>>.
9. Hill, Philip G., and Carl R. Peterson. *Mechanics and Thermodynamics of Propulsion*. 2nd ed. Reading, MA: Addison-Wesley, 1992. Print.
10. *An Introduction to Thermal Spray*. N.d. Instruction Manual. Sulzer Metco Inc., Westbury, NY.
11. Jacobson, N. "Oxidation and Corrosion of Ceramics and Ceramic Matrix Composites." *Current Opinion in Solid State and Materials Science* 5.4 (2001): 301-09. Print.
12. Jacobson, Nathan S., Gregory N. Morscher, Darren R. Bryant, and Richard E. Tressler. "High-Temperature Oxidation of Boron Nitride: II, Boron Nitride Layers in Composites." *Journal of the American Ceramic Society* 82.6 (1999): 1473-482. Print.
13. Kim, Ted T., Shankar Mall, and Larry P. Zawada. "Fatigue Behavior of Hi-Nicalon Type-S™/BN/SiC Ceramic Matrix Composites in a Combustion Environment." *International Journal of Applied Ceramic Technology* 8.2 (2011): 261-72. Print.

14. Kim, T. T., S. Mall, L. P. Zawada, and G. Jefferson. "Simultaneous Fatigue and Combustion Exposure of a SiC/SiC Ceramic Matrix Composite." *Journal of Composite Materials* 44.25 (2010): 2991-3016. Print.
15. Leng, Y. *Materials Characterization: Introduction to Microscopic and Spectroscopic Methods*. Singapore: J. Wiley, 2008. Print.
16. Luan, Xin'gang, Laifei Cheng, Yongdong Xu, and Litong Zhang. "Stressed Oxidation Behaviors of SiC Matrix Composites in Combustion Environments." *Materials Letters* 61.19-20 (2007): 4114-116. Print.
17. MacFarlane, R. R., R. S. DeFries, E. E. Reynolds, and W. W. Dyrkacz. *Research and Development of Wrought and Cast High Temperature Alloys*. Tech. no. 54-276. N.p.: n.p., 1954. Print.
18. Mall, Shankar, Andrew R. Nye, and George Jefferson. "Tension-Tension Fatigue Behavior of Nextel<sup>TM</sup>720/Alumina under Combustion Environment." *International Journal of Applied Ceramic Technology* 9.1 (2012): 159-71. Print.
19. Mattingly, Jack D., William H. Heiser, and David T. Pratt. *Aircraft Engine Design*. 2nd ed. Reston, VA: American Institute of Aeronautics and Astronautics, 2002. Print.
20. MTS. *MTS 810 & 858 Material Testing Systems*. Eden Prairie, MN: MTS, 2006. Print.
21. Opila, Elizabeth J., James L. Smialek, Raymond C. Robinson, Dennis S. Fox, and Nathan S. Jacobson. "SiC Recession Caused by SiO<sub>2</sub> Scale Volatility Under Combustion Conditions: II, Thermodynamics and Gaseous-Diffusion Model." *Journal of the American Ceramic Society* 82.7 (1999): 1826-34. Web.
22. Parthasarthy, T. A. "Burner RIg Flame Conditions." Message to the author. 24 Jan. 2014. E-mail.
23. Robinson, Raymond C., and James L. Smialek. "SiC Recession Caused by SiO<sub>2</sub> Scale Volatility Under Combustion Conditions: I, Experimental Results and Empirical Model." *Journal of the American Ceramic Society* 82.7 (1999): 1817-25. Web.
24. Sulzer Metco. *Diamond Jet DJ HVOF Spray Gun*. 2003. Component Manual. Westbury, NY.
25. Tortorelli, Peter F., and Karren L. More. "Effects of High Water-Vapor Pressure on Oxidation of Silicon Carbide at 1200°C." *Journal of the American Ceramic Society* 86.8 (2003): 1249-255. Print.

26. Turns, Stephen R. *An Introduction to Combustion: Concepts and Applications*. 2nd ed. Boston: McGraw-Hill, 2000. Print.
27. Zawada, Larry. "Density of Specimens." Message to the author. 19 Feb. 2014. E-mail.
28. *Zimmer Manual PN 52690 REV 5/19/03*. 19 May 2003. Zimmer Gas Vaporizer Manual.

REPORT DOCUMENTATION PAGE				Form Approved OMB No. 074-0188	
<p>The public reporting burden for this collection of information is estimated to average 1 hour per response, including the time for reviewing instructions, searching existing data sources, gathering and maintaining the data needed, and completing and reviewing the collection of information. Send comments regarding this burden estimate or any other aspect of the collection of information, including suggestions for reducing this burden to Department of Defense, Washington Headquarters Services, Directorate for Information Operations and Reports (0704-0188), 1215 Jefferson Davis Highway, Suite 1204, Arlington, VA 22202-4302. Respondents should be aware that notwithstanding any other provision of law, no person shall be subject to a penalty for failing to comply with a collection of information if it does not display a currently valid OMB control number.</p> <p><b>PLEASE DO NOT RETURN YOUR FORM TO THE ABOVE ADDRESS.</b></p>					
1. REPORT DATE (DD-MM-YYYY) 17-03-2014		2. REPORT TYPE Master's Thesis		3. DATES COVERED (From - To) November 2012 - March 2014	
TITLE AND SUBTITLE  Ceramic Matrix Characterization Under A Gas Turbine Combustion And Loading Environment				5a. CONTRACT NUMBER	
				5b. GRANT NUMBER	
				5c. PROGRAM ELEMENT NUMBER	
				5d. PROJECT NUMBER	
6. AUTHOR(S)  Bertrand, Dustin J., Captain, USAF				5e. TASK NUMBER	
				5f. WORK UNIT NUMBER	
7. PERFORMING ORGANIZATION NAMES(S) AND ADDRESS(S) Air Force Institute of Technology Graduate School of Engineering and Management (AFIT/ENY) 2950 Hobson Way, Building 640 WPAFB OH 45433-8865				8. PERFORMING ORGANIZATION REPORT NUMBER  AFIT-ENY-14-M-08	
9. SPONSORING/MONITORING AGENCY NAME(S) AND ADDRESS(ES) Air Force Research Laboratory 2230 10th Street B655 312-785-1352 email: larry.zawada@wpafb.af.mil ATTN: Larry Zawada				10. SPONSOR/MONITOR'S ACRONYM(S)  AFRL/RHIQ (example)	
				11. SPONSOR/MONITOR'S REPORT NUMBER(S)	
12. DISTRIBUTION/AVAILABILITY STATEMENT DISTRIBUTION STATEMENT A. APPROVED FOR PUBLIC RELEASE; DISTRIBUTION UNLIMITED.					
13. SUPPLEMENTARY NOTES This material is declared a work of the U.S. Government and is not subject to copyright protection in the United States.					
14. ABSTRACT The fatigue behavior of Hyper-Therm High Temperature Composites (HTC) Sylramic-iBN/BN/CVI SiC material was investigated while being subjected to a unique high temperature environment. The specimens used in this research were subjected to a high temperature combustion environment intended to simulate the conditions this material would see in turbine engine applications. Results show that the effects of the combustion environment on the materials fatigue behavior are significant with increasing temperature.					
15. SUBJECT TERMS Ceramic Matrix Composite, Combustion, Gas Turbine Engine Environment, Fatigue					
16. SECURITY CLASSIFICATION OF:			17. LIMITATION OF ABSTRACT  UU	18. NUMBER OF PAGES  136	19a. NAME OF RESPONSIBLE PERSON Dr. Shankar Mall, AFIT/ENY
a. REPORT U	b. ABSTRACT U	c. THIS PAGE U			19b. TELEPHONE NUMBER (937) 785-3636 x4587 (Shankar.mall@afit.edu)

Standard Form 298 (Rev. 8-98)  
Prescribed by ANSI Std. Z39-18